CONTROL OF WIND POWER SYSTEMS FOR ENERGY EFFICIENCY

AND RELIABILITY

by

Yan Xiao

APPROVED BY SUPERVISORY COMMITTEE:

____

Mario A. Rotea, Chair

____

Yaoyu Li, Co-Chair

____

Babak Fahimi, Co-Chair

____

Bilal Akin

To my beloved family

CONTROL OF WIND POWER SYSTEMS FOR ENERGY EFFICIENCY AND RELIABILITY

by

YAN XIAO, MS

DISSERTATION

Presented to the Faculty of

The University of Texas at Dallas

in Partial Fulfillment

of the Requirements

for the Degree of

DOCTOR OF PHILOSOPHY IN

ELECTRICAL ENGINEERING

THE UNIVERSITY OF TEXAS AT DALLAS

December 2018

ACKNOWLEDGMENTS

My sincere gratitude goes to my advisors, Dr. Mario Rotea, Dr. Yaoyu Li and Dr. Babak Fahimi, for their valuable guidance, trust and consistent support throughout my entire PhD study. Dr. Rotea and Dr. Li’s insightful view of optimal control and wind energy has helped me gain a deeper understanding in wind turbine control. Dr. Fahimi’s substantial support and professional guidance has made my study and research on DFIG (doubly fed induction generator) control a smooth and fruitful process. Most importantly, their rigorous academic attitude inspired me to learn how to study and how to perform academic research. I would also like to express my gratitude to Dr. Bilal Akin, for his valuable comments and suggestions.

I would like to acknowledge and thank the NSF WindSTAR Industry/University Cooperative Research Center for the financial support of the wind turbine control research projects. I also would like to express my gratitude to Mr. Andrew Scholbrock, Dr. Paul Fleming and Dr. Alan Wright at the National Wind Technology Center (NWTC), for the assistance on the CART3 field test.

Finally, I would like to thank all the members of Mechatronics System Lab and Renewable Energy and Vehicular Technology (REVT) Lab at The University of Texas at Dallas, for all their help and assistance during my PhD study.

August 2018

CONTROL OF WIND POWER SYSTEMS FOR ENERGY EFFICIENCY

AND RELIABILITY

Yan Xiao, PhD
The University of Texas at Dallas, 2018

Supervising Professor: Mario A. Rotea, Chair
Yaoyu Li, Co-Chair
Babak Fahimi, Co-Chair

With decades of development of wind energy technology, the cost of electricity production from wind has decreased significantly. To stimulate higher penetration of wind energy in the electric grid, further research and development are needed to reduce the Levelized Cost of Energy (LCOE) of wind power systems.

The LCOE of wind energy may be reduced by: 1) increasing the Annual Energy Production (AEP); 2) reducing the operation and maintenance (O&M) costs; 3) reducing the capital expenditures. On the aeromechanics side, increasing the AEP is achieved by increasing the turbine aeromechanical efficiency (the power coefficient C_P of a wind turbine), while reducing the O&M costs could be attained by reducing the aeromechanical forces and moments on the wind turbine rotor and structure. On the electrical side, the AEP is increased by increasing the efficiency of the electricity generation, conversion and transmission, while the capital expenditures may be reduced by lowering the costs of electric components.

Conventional wind turbine control schemes are mostly model based, and may rely on wind speed measurements for some cases. However, accurate wind turbine models and wind speed measurements may be difficult and costly to acquire. Extremum Seeking Control (ESC) is a nearly model-free optimization approach suitable for automatically finding the optimal torque gain and blade pitch angle that results in maximized wind turbine aeromechanical efficiency. Previous studies on ESC based wind turbine control are all simulation based. To further evaluate the effectiveness and potential of ESC for wind energy applications, it is necessary to implement the ESC controller on a commercial scale wind turbine, and evaluate the performance through field test. This dissertation presents the results of a field test of an ESC based controller on the NREL's (National Renewable Energy Laboratory) 600 KW CART3 wind turbine. Also, to reduce the wind turbine aeromechanical loads, while increasing the power coefficient, a multi-objective ESC wind turbine control scheme is proposed. The effectiveness of this multi-objective ESC is evaluated using computer simulations.

The second major part of this dissertation is dedicated to investigating two control challenges of the DFIG-DC (DFIG: doubly-fed induction generator; DC: direct current) framework. One of the most critical issues is the torque ripple caused by uncontrollable rectification. In this dissertation, a torque ripple mitigation scheme based on the Multiple Reference Frame (MRF) method is proposed. The effectiveness of the proposed strategy is evaluated through both simulations and experiments. Another control challenge of the DFIG-DC framework is associated with stator frequency control. This dissertation presents computer simulations and experiments indicating that the efficiency of the DFIG-DC system is a unimodal function of the stator frequency. It is also shown that the optimal stator frequency, attaining the highest efficiency, varies with the generator rotor speed. Since it is difficult to obtain an accurate efficiency model of the DFIG-DC system, ESC is implemented to find this optimal frequency in real time. The effectiveness and performance of the proposed ESC based optimal stator frequency control is evaluated with both simulations and experiments.

TABLE OF CONTENTS

LIST OF FIGURES

LIST OF TABLES

CHAPTER 1

INTRODUCTION

1.1 Overview of Wind Energy Conversion System (WECS)

A WECS is used to transform the kinetic energy of the wind into electricity. There are two stages in the conversion process. The first stage is to extract the kinetic energy from the wind with rotor blades, i.e., part of kinetic energy from the wind flow is transferred to the rotational mechanical energy of the rotor blade and the drive train. A generator is used in the second stage to convert this rotational mechanical energy into electricity.

There are two basic configurations of WECS, namely Horizontal Axis Wind Turbines (HAWT)[5], and Vertical Axis Wind Turbines (VAWT)[6] as shown in Figure 1.1.

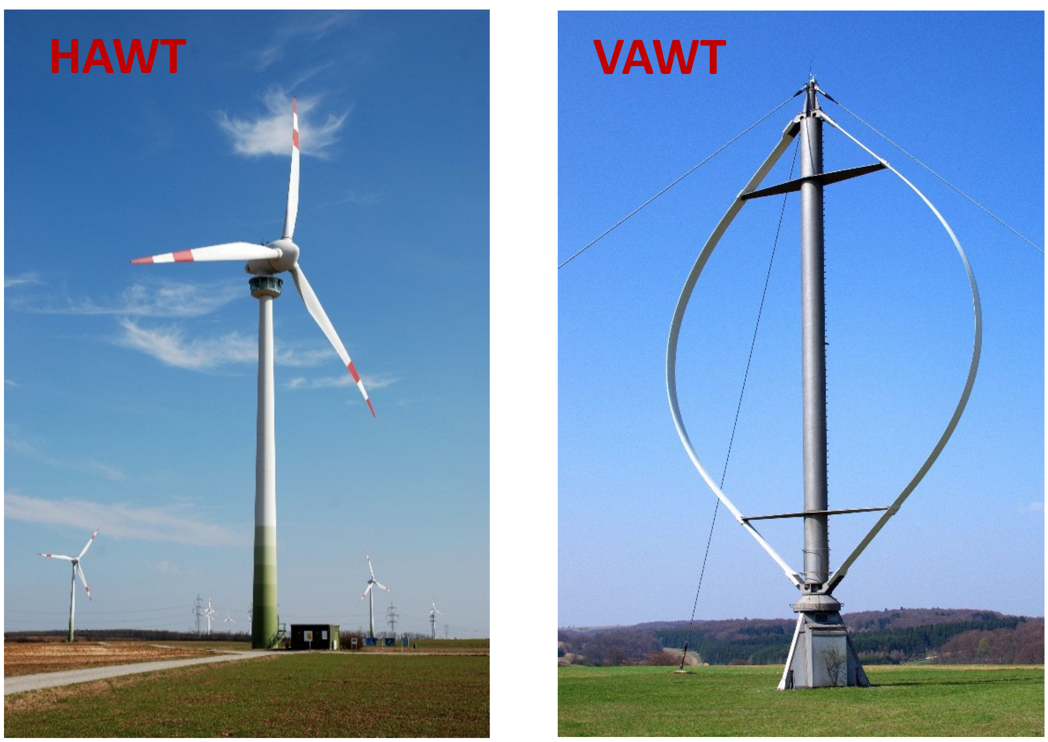

Figure 1.1. HAWT (courtesy KoeppiK) and VAWT (courtesy W. Wacker)

VAWTs are typically used in small power rating scenarios. HAWT dominates the utility-scale wind energy market due to its various advantages (improved power capture, structural performance, etc.) over VAWT. This dissertation is focused on HAWT due to its wide-spread use. Throughout this document, we will use wind turbine to refer to HAWT, unless it is stated otherwise.

Depending on the range of rotational speed during normal operation, wind turbines can be categorized as variable speed or fixed speed type. Variable speed wind turbines can operate closer to their maximum aerodynamic efficiency over a wide wind speed range. Also, for variable speed wind turbine, wind gusts can be absorbed and stored as rotational inertia energy of the turbine. In this way, the torque pulsation is reduced by this "elasticity", which means reduced mechanical stress compared with fixed-speed wind turbine. From electrical side of view, less torque pulsation results in smaller electrical power variations, i.e. less flicker. Therefore, the power quality is improved compared with fixed-speed wind turbine. Last but not the least, a variable speed wind turbine can operate at low rotational speeds (low wind speeds), which would reduce the acoustic noise. Thanks to the afore-mentioned advantages, variable-speed wind turbines are used much more than their fixed-speed counterparts, especially for large scale wind turbines.

Wind turbines can also be categorized as variable pitch or fixed pitch type depending on whether the blades are able to rotate along their longitudinal axis during normal operation. Although fixed-pitch wind turbine is less expensive compared with variable-pitch design, the lacking capability of regulating the aerodynamic loads makes fixed-pitch wind turbine not suitable for large scale wind turbines. Fixed-pitch wind turbines are typically seen in small power rating cases.

In this dissertation, we focus on variable-speed, variable-pitch wind turbines. Since this type of wind turbine is much more common, especially for utility-scale units. Figure 1.2 shows a typical wind turbine with major components labeled. As can be seen, turbine blades convert the kinetic energy from the incoming wind flow to the rotational mechanical energy, which is then transferred to the generator through drive train (low-speed shaft, gear box, high-speed shaft). The generator converts the rotational mechanical energy into electricity.

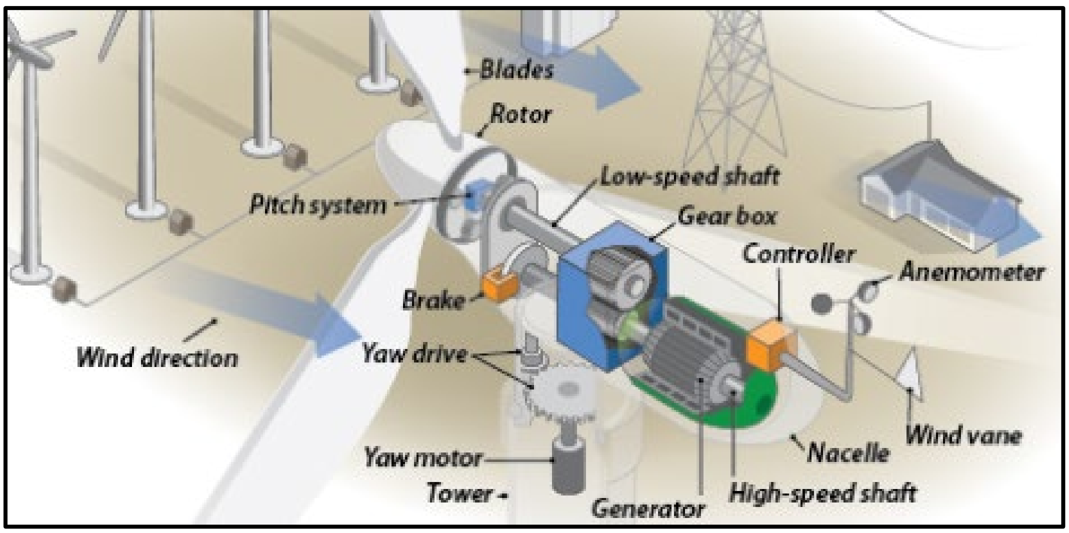

Figure 1.2. Components of a wind turbine (courtesy U.S. Department of Energy)[7]

For variable-speed variable-pitch wind turbines, rotational speed can be regulated by changing the generator torque reference in Region-2 (below rated wind speed) operation. In Region-3 (above rated wind speed), blade pitch angle is regulated using the pitch mechanism to maintain the generator speed around its rated value. Besides blade pitch angle control and generator torque control, yaw control is also needed to ensure that wind turbine is facing directly into the wind flow direction, so that the energy capture can be maximized.

1.2 Extremum Seeking Control (ESC) Based Region-2 Wind Turbine Control

Wind power dominates utility-scale renewable power generation. A key objective in this industry is to reduce the Levelized Cost of Energy (LCOE). As introduced in the previous section, this may be accomplished by enhancing the energy capture below the rated wind speed (Region 2). Improving the control software in Region-2 is a cost-effective approach to achieving such objective. This is particularly significant for existing fleets, which as a result of aging may require re-tuning of the control laws. The power produced by a wind turbine operating in Region-2 is proportional to the power available in the wind. The constant of proportionality is referred as the power coefficient C_P. Thus, to maximize the energy capture in Region-2 operation, it is necessary to maximize the power coefficient C_P.

For variable-speed variable-pitch wind turbines, the power coefficient C_P is typically a unimodal function of tip-speed ratio (TSR) λ and blade pitch angle β. Thus, C_P can be maximized at a specific combination of TSR and blade pitch angle. Note that TSR is defined as

$$TSR = \frac{\omega R}{v} \tag{1-1}$$

Where ω is the rotor angular speed in radians/second, R is the radius of the wind turbine rotor in meters, v is the wind speed in meters/second.

The basic objective for Region-2 control is to achieve the optimum C_P in real time under unsteady wind conditions by adjusting the TSR (via control of the generator torque) and/or the blade pitch angle for maximum power production. Most of the existing Region-2 control strategies are model based, which typically requires pre-calibrated models or look-up tables obtained from analytical and/or empirical data at a number of prescribed wind conditions; and, in some cases, wind measurements in real time. However, accurate model of wind turbine or wind speed measurement is difficult to acquire. Since aerodynamic characteristics of wind turbines are complex, nonlinear and time-varying, affected by factors such as wind speed and direction, wind shear, air density, blade surface wear and accumulation of ice, dirt and bugs.

Extremum Seeking Control (ESC) provides a nearly model-free solution for maximizing power coefficient C_P. ESC estimates the gradient online by using a dither signal and a demodulation signal. By closing the loop via integral control acting on the estimated gradient, the global optimality would be achieved assuming stability of the ESC and convexity of the performance map.

Existing works have shown the potential of ESC based Region-2 controller in maximizing energy capture. However, to our knowledge, all these studies are simulation based. To better evaluate the performance of ESC based wind turbine Region-2 control, it is necessary to implement the ESC controller on a commercial scale wind turbine to perform field testing. One of the main contributions of this dissertation is the field testing of ESC based Region-2 control on NREL's 600 KW wind turbine.

1.3 Multi-objective ESC for Energy Capture Enhancement with Load Reduction

For wind turbine operation, the primary objective for below rated wind speed (Region-2) is to maximize the energy capture. As the wind turbine characteristics are affected by the variations in wind speed, direction and shear, change of blade aerodynamic behavior due to various surface accumulations as well as inaccurate wind measurements, model-based control strategies have limited performance for the Region-2 operation. Thus, model-free and wind-measurement-independent control strategies such as Extremum Seeking Control (ESC) have received significant attention. Based on a dither-demodulation scheme, ESC can maximize the wind power capture in real time with remarkable robustness against turbulence and other external factors. While the existing work on ESC based wind turbine control focuses on power capture only, certain loads may increase during ESC operation. In this dissertation, a multi-objective extremum seeking control strategy is proposed to achieve nearly optimum wind energy capture while preventing excessive increase in structural fatigue load. The objective function of rotor power is modified by adding penalty terms of the standard deviations of selected fatigue load variables. Simulation study of the proposed multi-objective ESC demonstrates that the damage equivalent load of tower and/or blade load can be reduced significantly with a very small compromise in energy capture.

1.4 Overview of Doubly-fed Induction Generator (DFIG) - DC System

DC power systems are gaining more and more attention in recent years due to the fast development of High Voltage Direct Current (HVDC) transmission, DC micro-grids and distributed generation systems. Compared with conventional AC transmission, DC transmission is more efficient and cost effective due to: 1) there is no reactive power flow; 2) DC transmission requires less conductor per unit length than AC transmission, since only two wires are needed (compared with three wires for AC transmission), also, thinner wire can be used for DC transmission since there is no skin effect. For micro-grid and distributed generation system applications, DC systems allow an easy integration of different power generation units and power loads by simplifying the layout and the number of electronic converters [8].

One important aspect of DC power system research is focused on developing a reliable and cost-effective interface between conventional AC generators and DC systems. Both Induction Generator (IG) and Permanent Magnet Synchronous Generator (PMSG) can be connected with DC system. However, a full power rating three-phase PWM rectifier is needed for high performance control. By replacing the three-phase PWM rectifier with uncontrollable diode rectifier, the system cost can be reduced considerably. However, an additional full power DC-DC converter is needed to allow some basic regulation (such as generator torque control for variable-speed wind turbines) of the system. Even with this additional full power rating DC-DC converter, the torque ripple caused by the uncontrollable rectification process cannot be effectively mitigated [9].

As a better alternative, [10] and [11] proposed the so-called DFIG-DC framework. In which a diode bridge rectifier is used to connect the stator winding of DFIG to the DC link, as shown in Figure 1.3. Similar to conventional DFIG-AC configuration, a small power rating (typically 25% of the full power) three-phase PWM converter is connected to the rotor winding of DFIG. Unlike conventional DFIG-AC system, the rotor side PWM converter is connected to the DC link directly, therefore, there is no need for the grid side PWM converter. The elimination of one PWM converter could reduce the system cost.

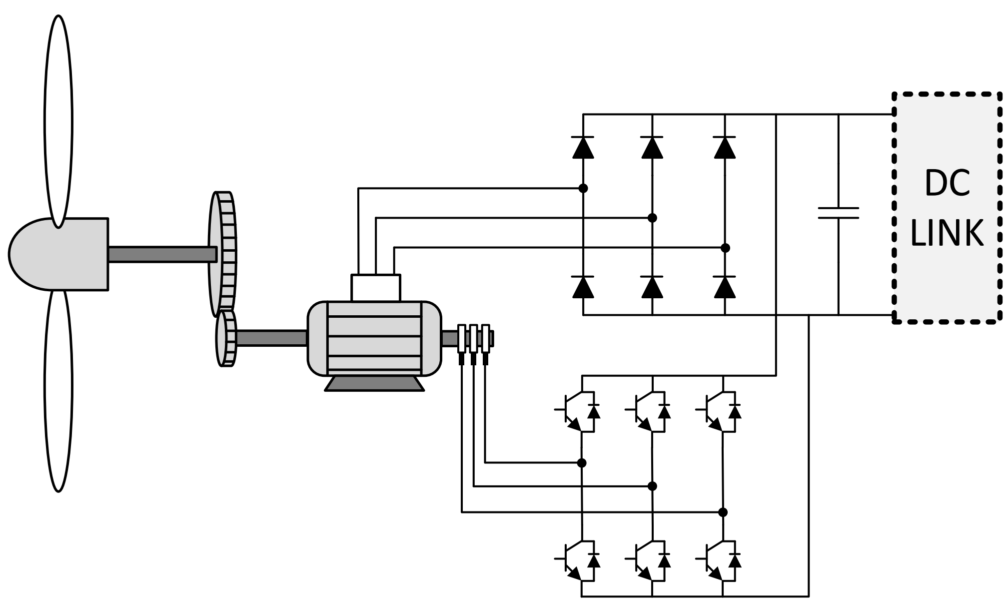

Figure 1.3. Overview of DFIG-DC system for wind energy production

Despite the benefits of low cost, there is an inherent drawback in this system. Due to the uncontrollable rectification, the stator voltage, current and flux would be distorted with harmonics. The resultant electromagnetic torque will be introduced with harmonics which causes the pulsation of torque (i.e. torque ripple). The torque ripple will generate more fatigue load on the wind turbine structure. As a result, the components are more likely to fail prematurely, which would induce higher repair and maintenance cost. Without addressing the problem of torque ripple, the low cost of DFIG-DC system might be offset by the increasing maintenance and repair cost.

Another challenge of the DFIG-DC system lies in the stator frequency control. For conventional configuration of DFIG connected with AC grid, the stator frequency is imposed by the AC grid frequency (60 Hz in US). However, for the studied DFIG-DC framework, the stator frequency is not imposed by the DC grid. This additional freedom of stator frequency control poses an interesting question: At what value should the stator frequency be regulated?

1.5 Torque Ripple Mitigation Control of DFIG-DC System

The torque ripple in the DFIG-DC system can be reduced by implementing a multi-pulse (12 pulse, for example) rectifier. However, a multi-phase DFIG or transformer would be required [59]. Another method to mitigate the torque ripple is to add an Active Power Filter (APF) to the stator winding of the DFIG [60], with appropriate control, the harmonic terms in the stator current can be filtered out, which will result in the reduction of torque ripple.

However, the approaches described above require additional investment on hardware cost, which may offset the advantage of low cost of the DFIG-DC framework. As a result, it is more favorable to develop a torque ripple reduction scheme which does not require additional hardware investment.

Although the studied DFIG-DC system only has one PWM converter, this framework still preserves the capability of high performance control. With full freedom in the control of rotor current, it is possible to regulate the instantaneous generator torque. With appropriate control method, the torque ripple caused by uncontrollable rectification can be reduced. Several control-based torque ripple mitigation schemes are reviewed and discussed in Chapter 2. In this dissertation, a Multiple Reference Frame (MRF) based torque ripple mitigation scheme is proposed and evaluated for the DFIG-DC system.

The stator current and flux are mainly distorted with sixth order harmonics. To obtain a relative constant electromagnetic torque, the rotor current need to be compensated with harmonic (mainly six times of the stator frequency) reference. However, due to stability requirement, the bandwidth of the current control loop is typically not adequate to track the fast-changing command value. The proposed MRF based torque ripple mitigation controller is capable of extracting the current vector associated with a certain reference frame. In this way, the fast-changing harmonic signal in synchronized reference frame is transformed into relatively constant signal in the corresponding rotational reference frame. As a result, the MRF controller can easily deliver good tracking performance for fast-changing harmonic reference, even with a conventional PI controller. Both simulations and experiments presented in this dissertation have demonstrated the effectiveness of the proposed scheme in reducing the torque ripple of the DFIG-DC system.

1.6 Optimal Stator Frequency Control of DFIG-DC System

Compared with conventional DFIG-AC systems, another peculiarity of the DFIG-DC framework is that the stator frequency of the DFIG is not imposed by the DC grid. The additional need of stator frequency regulation adds an extra freedom of control to the system. This introduces two interesting questions: 1. Is there an optimal stator frequency at which the DFIG-DC system's efficiency is maximized? 2. Is it possible to implement model-free optimization algorithms such as ESC to find this optimal frequency?

Both simulations and experiments included in this dissertation demonstrate that the efficiency map of the DFIG-DC system is a unimodal curve with respect to different stator frequency, assuming the generator rotor shaft speed is fixed. It is also shown that the optimal stator frequency that results in highest efficiency varies with the generator rotor shaft speed. To achieve maximum efficiency during variable speed operation, it is necessary to implement a real-time optimal stator frequency controller. Since it is difficult to obtain an accurate power loss model (or efficiency model) of the DFIG-DC system, in this dissertation, the nearly model free real-time optimization scheme, Extremum Seeking Control (ESC), is adopted to find the optimal stator frequency in real time that results in improved efficiency of the DFIG-DC system.

1.7 Research Statements and Dissertation Organization

With the introduction of research background in the previous sections, the research problems of interest for this dissertation are summarized as follows:

1) Design and development of an ESC based Region-2 controller for field test evaluation
2) Design and development of a multi-objective ESC Region-2 controller to enhance energy capture while limiting the structure load
3) Design and development of an MRF based torque ripple mitigation framework for the DFIG-DC system.
4) Design and development of an ESC based optimal stator frequency regulator to achieve improved efficiency of the DFIG-DC system.

The remainder of this dissertation is organized as follows:

Chapter 2 presents a literature review relevant to the topics included in this dissertation, with discussion on achievements and limitations of the existing works. The limitations motivate, in part, the research in this dissertation.

Chapter 3 presents the field test study for wind turbine Region-2 operation with extremum seeking controllers. The control variables are torque gain and blade pitch angle. The measured rotor power is used as feedback for the ESC controller. Field test of the following three different scenarios were performed: 1. Torque-gain ESC; 2. Blade-pitch ESC; 3. Two-input (Torque-gain + Blade-pitch) ESC. The proposed ESC based Region-2 controller is implemented on NREL's CART3 wind turbine (600 kW, variable-speed, variable-pitch). The field test results demonstrate the effectiveness of the proposed scheme in increasing the energy capture of wind turbine in Region-2 operation, without the need of accurate model information or wind measurements.

In Chapter 4, a Multi-Objective Extremum Seeking Control (MOESC) based Region-2 wind turbine controller is proposed to increase the energy capture while limiting the load increase of the wind turbine structure. Similar to standard Region-2 ESC controller, the two control variables are torque gain and blade pitch angle. The main difference of the proposed MOESC framework is that the measured rotor power penalized by the measured load is used as the feedback to the ESC controller. Simulation study on CART3 FAST [80] model demonstrates the effectiveness of the proposed control strategy in improving the energy capture while limiting the increase of load.

In Chapter 5, a Multiple Reference Frame (MRF) based torque ripple mitigation scheme is proposed to reduce the torque ripple caused by diode bridge rectification in DFIG-DC system. An analysis on the root cause of the torque ripple in the DFIG-DC system is given first. Followed by the design of the proposed MRF based torque ripple mitigation controller. Both simulation results and experimental results have demonstrated that the proposed algorithm can effectively reduce the level of torque ripple.

Chapter 6 presents the study regarding the optimal stator frequency control in DFIG-DC system. Both simulation and experimental test show that the efficiency map of the DFIG-DC system demonstrates a unimodal curve with reference to different stator frequency. At certain frequency setting, the power efficiency of the DFIG-DC system is maximized. To find this optimal stator frequency, an ESC based optimal stator frequency controller is implemented. Both simulations and experiments demonstrate that ESC can successfully find the optimal state frequency that results in maximized power efficiency of the DFIG-DC system.

The preliminary CART3 ESC field test results have been demonstrated in [49]. The full test results included in Chapter 3 have been published in [88], Chapter 4 has appeared already in [89], while the results in Chapter 6 will appear in [90].

CHAPTER 2

LITERATURE REVIEW

In this chapter, a literature review relevant to the dissertation topics is included. As the major self-optimizing control scheme adopted in this dissertation, works on extremum seeking control are first reviewed. Then, literature review regarding existing studies on Region-2 wind turbine control is given. Followed by literature review on existing torque ripple mitigation scheme for the DFIG-DC system. Existing studies on stator frequency regulation and optimal stator frequency control of DFIG-DC system are reviewed in the end. Discussion regarding possible limitations of the existing research are highlighted to explain the value and motivation of the research in this dissertation.

2.1 Review of Extremum Seeking Control

As a nearly model-free real-time optimization algorithm, extremum seeking control represents a major class of self-optimization control methods. ESC aims to find the optimal value of an unknown and/or slowly time-varying performance function, with only limited knowledge of the system models.

The complexity of many physical systems poses great challenges to their optimization. It is typically difficult, if not impossible, to describe an engineered system with an accurate model for optimization, especially for multi-variable, nonlinear, and high-dimensional systems. Due to this limitation, in certain applications, it is preferred to pursue a non-model-based approach such as extremum seeking to solve these optimization problems.

The idea of ESC was first introduced by Leblanc [12] in 1922. Since then ESC has been used in various applications such as internal combustion engines [13] and gas furnaces [14]. In the late twentieth Century, extremum seeking control was nearly dormant for decades until the proof of its stability was given by Krstić and Wang [15], which employs the averaging analysis and the singular perturbation method. Rotea [16], Krstić and his co-workers [17] later extend such analysis to the multi-variable extremum seeking control.

The proof of stability has revived the research interests towards ESC, with many new applications in different areas: such as HVAC [18][19][20], variable refrigerant flow system [21][22], MPPT control of PV system [23], wastewater treatment [24], fuel cells [25], robot navigation [26], vehicle ABS braking system [27], laser control [28], bioreactor [29] etc. ESC has also been implemented into a single wind turbine [30] or a cascaded wind turbine array [31] for enhancement of energy capture.

2.2 Review of Region-2 Wind Turbine Control

For variable-speed variable-pitch wind turbines, the power coefficient C_P is a unimodal function of Tip-Speed Ratio (TSR) λ and blade pitch angle β [32]. C_P is maximized at a specific combination of TSR and blade pitch angle. The basic objective of Region-2 control is to achieve the maximum C_P in real time under unsteady wind conditions by adjusting the TSR (via control of the generator torque) and/or the blade pitch angle.

Most of the Region-2 control strategies reported in the literatures are model based [33-40]. Traditional model-based control strategies [33-37] typically require calibrated models or lookup tables obtained from analytical and/or empirical data at a number of prescribed wind conditions; and, in some cases, wind measurements in real time. Advanced control techniques have also been applied, e.g. linear quadratic control [38], model predictive control [39] and linear parameter-varying control [40]. The field performance of the model-based control schemes can be limited due to model uncertainty and/or inaccurate wind estimates. Aerodynamic characteristics of wind turbines are complex, nonlinear and time-varying, affected by factors such as wind speed and direction, wind shear, air density, blade surface wear and accumulation of ice, dirt and bugs. In modern wind turbines, any wind estimates used for control purposes are typically obtained from rotor speed through the knowledge of wind turbine aerodynamic characteristics which may not be precisely known and can vary through operation. It is thus desirable to develop Region-2 control strategies with little dependency on wind turbine models and accurate wind estimates.

A few authors have studied model-free or adaptive schemes for Region-2 control. Johnson et al. [41][42] applied a Model Reference Adaptive Control (MRAC) scheme. The optimal TSR is obtained by controlling the generator torque following the classical quadratic torque control law

$$\tau_g = k_t \cdot \Omega_h^2 \tag{2-1}$$

where τ_g is the calculated generator torque command, Ω_h is the angular speed of the high-speed shaft, and k_t is the torque gain. The MRAC tunes the torque gain k_t in real time using an estimate of the power coefficient obtained from averaging the power output and a real-time measurement of the wind speed, which is referred as the normalized power output. Both simulation and field testing demonstrate improvement in energy capture. A potential limitation of this approach is its dependency on the wind measurement due to the feedback of the normalized power. In this scheme, it can be difficult to distinguish the change in the normalized power output due to wind fluctuations from that due to the tuning of the torque gain.

Extremum Seeking Control (ESC) [43][16][44] is a nearly model-free real-time optimization algorithm that implements a gradient-based steepest ascent search. The ESC algorithm estimates the gradient by using a dither signal (the gradient carrier) and a demodulation signal. The necessary condition for optimality is achieved by closing the loop via integral control acting on the estimated gradient. The result, assuming stability, is a vanishing gradient leading to the solution of first-order optimality conditions. A distinctive advantage of such strategy is that the gradient extraction process is locked to the dither frequencies, which results in two benefits: 1) the search process is insensitive to exogenous disturbances provided that the dithered output achieves significant signal-to-noise ratio (SNR) at the dither frequency; 2) multi-input search can be easily realized by assigning different dither frequencies to different input channels. These attributes make ESC an attractive Region-2 control algorithm under fluctuating wind.

Earlier attempts of single-input ESC based Region-2 controller were reported by Komatsu et al. [45] and Ishii et al. [46]. Creaby et al. [30] proposed a multi-input ESC scheme for maximizing the wind power output using the generator torque gain and blade pitch angle. Improvements in energy capture were demonstrated through computer simulations. Johnson and Fritsch [47] evaluated advantages and limitations of ESC.

To our knowledge, the reported studies on Region-2 ESC have all been simulation based. Field testing is necessary to evaluate the actual effectiveness of ESC. This dissertation presents an experimental evaluation of the ESC based Region-2 wind turbine controller on the CART3 facility [48] at NREL.

Existing studies on ESC based Region-2 control have been focused on maximizing power without consideration of load impact. Under certain combinations of control actions, wind inputs and turbine characteristics, structural loads may increase. Also, due to undesirable structure design or construction, it is possible to excite structural modes even with the conventional Region-2 operation of blade pitch and/or generator torque control [79]. Such resonance modes may change with site and time since they are influenced by construction and foundation variability, as well by component degradation, which may not be predictable from the design model. The induced increase in Damage Equivalent Load (DEL) may undermine the benefit of the power increase with ESC, thus compromising the Levelized Cost of Energy (LCOE). Therefore, it is desirable to limit the growth of structural loads while maximizing the wind energy capture, without acquisition and/or calibration of turbine structural model. A multi-objective ESC based Region-2 wind turbine control scheme is proposed in this dissertation to maximize the energy capture while limiting structure loads.

2.3 Review of Torque Ripple Mitigation for DFIG-DC System

The DFIG-DC framework studied in this dissertation benefits from the low cost of diode bridge rectifier. However, the uncontrollable rectification produces a highly distorted stator voltage and stator flux linkage, as demonstrated in [50] and [51]. The interaction between the distorted stator flux linkage and current would cause significant torque ripple. This would introduce large mechanical stress to the drive train of a wind turbine, which in return would increase the LCOE of the wind energy. By using multi-pulse rectifier, the current and torque harmonics can be reduced significantly in the DFIG-DC system. However, the need of a multi-phase transform [52] or DFIG [53] would increase the system cost. To reduce the torque ripple without adding extra hardware investment to the system, torque ripple mitigation through appropriate control of rotor side converter (RSC) has received attention in the past few years.

In order to obtain a relatively constant generator torque, the rotor current need to track a pulsating (mainly six times of the stator frequency) reference to compensate for the distorted stator flux linkage [51]. To track this fast-changing rotor current reference, simple Proportional-Integral (PI) controller need to be designed with an unrealistic high bandwidth, which is unfeasible for application due to noise and reduction of stability margins in the stator flux dynamics [54][55]. In [56], the authors proposed a scheme based on feedforward transient compensation control. Although this could reduce the impact of harmonics on the rotor current control, however it does not improve the tracking performance of the pulsating reference.

Proportional integral resonant (PI-R) controllers have good tracking capability for the reference signal at pre-designed resonant frequency. As seen in [9][57][58], this scheme can successfully reduce the torque ripple in the DFIG-DC system. However, since the resonant controller is designed to cope with a specific frequency, when the harmonic frequency deviates from the designed value, the tracking performance would deteriorate substantially. The sensitivity to the frequency fluctuations is the main drawback of this approach [59]. Adjusting the resonance frequency on the fly based on the real-time stator frequency estimation can indeed increase the robustness against small range of frequency deviation [51]. However, it adds complication to the system, and can cause unwanted interactions with current controller if the frequency varies over a wide range. In [60], the authors use active filters to eliminate current harmonics to suppress the torque ripple. However, this approach is not suitable for the studied DFIG-DC structure, since the grid side converter in this scheme work is required.

In [61], authors proposed a repetitive-control-based torque ripple mitigation method for the DFIG-DC system. The proposed repetitive controller is essentially a combination of many resonant controllers designated to different order of harmonic frequency working in parallel. This framework can be seen as an enhancement for the PI-R method introduced previously. Since one repetitive controller can track many orders of resonant frequencies simultaneously, while one resonant controller in PI-R scheme is only capable of tracking one resonant frequency. Similar to PI-R control, the shortcoming of this method is the lack of robustness against stator frequency deviation.

Recently, a torque ripple mitigation approach based on predictive delay compensation is proposed in [59]. Compared with PI-R framework, the proposed method is very robust against wide range of stator frequency deviation. However, the good performance of this scheme is contingent on the accuracy of the estimated predictive advance time.

A model predictive control (MPC) based approach was adopted in [83] to reduce the torque ripple in the DFIG-DC system. The proposed algorithm predicts the future torque response under each available control action (seven different voltage vectors), and then select the optimal voltage vector that results in the smallest deviation from the commanded torque. For traditional Field-Oriented Control (FOC) based control scheme which relies on PI current loop controller, as introduced previously, one of the major drawbacks is the limitation of the controller bandwidth. The MPC based direct torque control approach introduced in this paper can achieve very fast control bandwidth. Also, this scheme is very robust against stator frequency variation. One of the major limitations of this method is that it poses higher requirement for the calculation speed of the control action. Another major drawback of this method is that the performance relies heavily on the availability and accuracy of the system model information.

In this dissertation, a multiple reference frame (MRF) based torque ripple mitigation scheme is proposed. This scheme was used in [62] to suppress the stator current harmonics in conventional DFIG-AC layout. Similarly, we can implement this algorithm in DFIG-DC system to track the pulsating rotor current reference with PI controllers operating at multiple reference frames. This method is very robust against variation of stator frequency due to the fact that the rotational speed of the reference frame is synchronized with the stator frequency. Also, unlike the framework based on predictive delay compensation or MPC, MRF does not require detailed model information.

2.4 Review of Stator Frequency Control of DFIG-DC System

As introduced in Chapter 1, the stator frequency of the DFIG-DC system provides an additional degree of freedom for control. The only constraint imposed by the DFIG-DC system, assuming relatively constant DC bus voltage, is that the product of the stator frequency and the amplitude of the stator flux linkage must be constant. By controlling the d-axis rotor current in the stator flux field-oriented control (FOC) frame, the stator flux linkage could be changed. As a result, the stator frequency can be regulated.

There are only a few studies discussing the stator frequency control of DFIG-DC system. And most of the existing literature ([53][11][63][64]) is focused on regulating the stator frequency to the rated value, without consideration of optimal stator frequency control to increase the system efficiency. In [65], optimal stator frequency control aimed to increase the efficiency of DFIG-DC system is investigated. However, this optimization scheme is model based, which adds complexity to the control system design. Also, the performance of this scheme is limited by the model accuracy.

A Model Predictive Control (MPC) based approach was recently reported in [83]. This control algorithm has good dynamic performance due to its fast control bandwidth. However, similar to the algorithm investigated in [65], complex computation is required. Also, the practical implementation could be limited by the availability and accuracy of the model information.

As a nearly model-free optimization algorithm, Extremum Seeking Control (ESC) seems to be a better option for optimal stator frequency regulation of the DFIG-DC system. In this dissertation, an ESC based optimum stator frequency controller is developed and implemented. Both simulations and experiments were conducted to evaluate the performance of ESC in improving the efficiency of the DFIG-DC system.

CHAPTER 3

EXTREMUM SEEKING CONTROL BASED REGION-2 WIND TURBINE CONTROL*§

3.1 Introduction and Research Motivation

As introduced in Chapter 1, the available power extracted by a wind turbine operating in Region-2 is proportional to the power available in the wind. The constant of proportionality is defined as the power coefficient C_P. Thus, to maximize power output in Region-2, it is necessary to maximize the power coefficient C_P, as the power available in the wind is not controllable.

For variable-speed variable-pitch wind turbines, as can be seen from Figure 3.1, the power coefficient C_P is typically a unimodal function of Tip-Speed Ratio (TSR) λ and blade pitch angle β. Thus, at a specific combination of TSR and blade pitch angle, C_P can be maximized. The basic objective for Region-2 control is to achieve the optimum C_P in real time under fluctuating wind by adjusting the TSR (via control of the generator torque) and/or the blade pitch angle.

As discussed in Chapter 1, most traditional wind turbine Region-2 control strategies are model based. The performance of such controller is limited by the accuracy of the model and, in some cases, wind measurements. However, accurate model information and wind measurements are difficult and costly to guarantee. Also, the aerodynamic characteristic of the wind turbine could vary due to the change of wind field (wind direction, wind shear, etc.), accumulation (dirt, bug, snow, ice, etc.) and erosion of turbine blades. Due to these reasons, it is favorable to develop a Region-2 wind turbine controller that does not rely on wind turbine model and wind measurements.

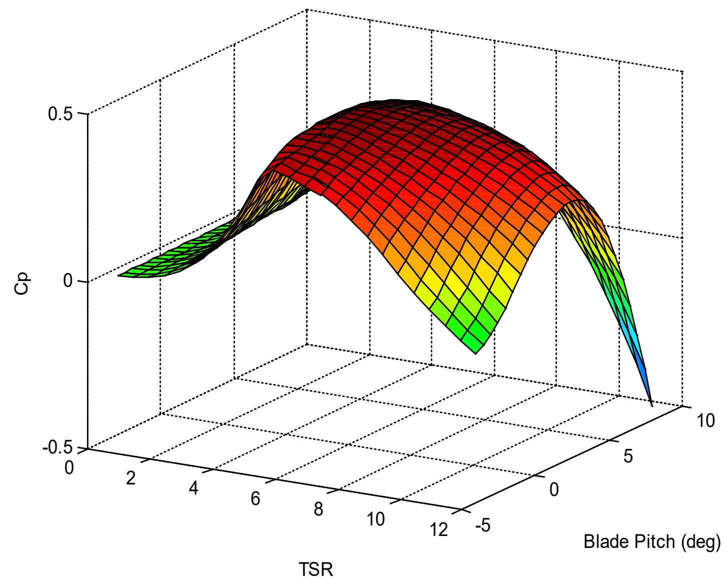

Figure 3.1. Variation of power coefficient C_P with TSR and blade pitch angle for the CART3 turbine at the National Renewable Energy Laboratory (NREL), obtained from WT_PERF [66]

As a nearly model-free optimization framework, Extremum Seeking Control (ESC) is a good candidate for wind turbine Reigon-2 controller. ESC is essentially an online gradient estimator based on a pair of dither (modulation) and demodulation signal. Assuming stability of the ESC loop and convexity of the static map of the plant, optimality would be eventually achieved by closing the loop of the estimated gradient with an integrator.

Existing works have proven the effectiveness of ESC in maximizing the power coefficient of wind turbine at Region-2 operation [30][45][46][47]. However, to our best knowledge, all the existing works are simulation based. To properly evaluate the performance of ESC based Region-2 controller, it is necessary to implement the ESC controller on a commercial-scale wind turbine and perform field tests. This chapter presents the field test results of ESC based Region-2 controller implemented on NREL's 600 KW CART3 wind turbine.

3.2 Overview of ESC and Design Guidelines

3.2.1 ESC Overview

As introduced in Chapter 2, ESC is a class of self-optimizing control strategy that can search for an unknown and/or time-varying input that optimizes a performance index of a nonlinear dynamic plant [16][43][44]. Among different variations of ESC schemes, a primary category is based on the use of a periodic perturbation to extract the gradient information [43].

Figure 3.2 shows a nonlinear plant where $f(u)$ is the performance index to be optimized by selecting the control input(s) u. The diagram includes Linear Time Invariant (LTI) input and output dynamics, $F_{in}(s)$ and $F_{out}(s)$, respectively. In this study, u can be the generator torque gain k_t and/or blade pitch angle β, while y is the rotor power derived from measurements of rotor shaft torque and rotational speed. The objective of ESC is to maximize the plant output y by manipulating the control input(s) u in real time. The ESC accomplishes this goal by finding the input(s) that leads to a vanishing gradient. The operating principle of ESC is reviewed for the single-input scenario [16]. For simplicity, we assume that the transfer functions $F_{in}(s)$, $F_{out}(s)$ and $F_{HP}(s)$ have unit magnitude at the dither frequency ω.

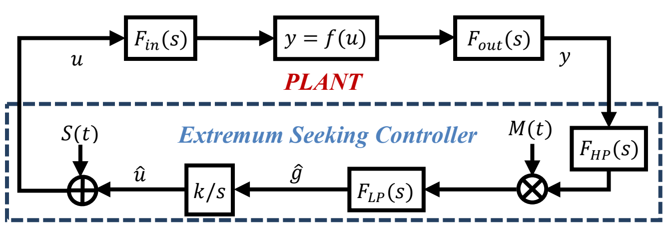

Figure 3.2. Block diagram of dither based ESC

The gradient $\partial f / \partial u$ is estimated from the measurements of the objective function y with a dither signal $S(t) = a\sin(\omega t)$ added to the input, i.e.

$$u = \hat{u} + a\sin(\omega t) \tag{3-1}$$

The corresponding plant output is then approximated as

$$y = f[\hat{u} + a\sin(\omega t + \varphi_{in})] \tag{3-2}$$

where φ_{in} represents the phase shift caused by the input dynamics at the dither frequency. The Taylor series expansion of Equation (3-2) is

$$y = f[\hat{u} + a\sin(\omega t + \varphi_{in})] = f(\hat{u}) + a\sin(\omega t + \varphi_{in})\frac{\partial f}{\partial u} + h.o.t. \tag{3-3}$$

The high-pass filter is designed to suppress the DC term in Equation (3-3) while passing the AC terms. Its output is approximated as

$$a\sin(\omega t + \varphi_{in} + \varphi_{out} + \varphi_{HP})\frac{\partial f}{\partial u} + h.o.t. \tag{3-4}$$

where φ_{out} and φ_{HP} denote the phase shifts caused by the $F_{out}(s)$ and $F_{HP}(s)$ at the dither frequency, respectively. The signal in Equation (3-4) is then multiplied by the demodulation signal $M(t) = \sin(\omega t + \theta)$ to obtain

$$\begin{aligned} &\sin(\omega t + \theta) \times [a\sin(\omega t + \varphi_{in} + \varphi_{out} + \varphi_{HP})\frac{\partial f}{\partial u} + h.o.t.] = \\ &\qquad \frac{a}{2}\frac{\partial f}{\partial u}[\cos(\theta - \varphi_{in} - \varphi_{out} - \varphi_{HP}) - \cos(2\omega t + \varphi_{in} + \varphi_{out} + \varphi_{HP} + \theta) + h.o.t.] \end{aligned} \tag{3-5}$$

The low-pass filter $F_{LP}(s)$ is designed to retain the DC term $\frac{a}{2}\frac{\partial f}{\partial u}\cos(\theta - \varphi_{in} - \varphi_{out} - \varphi_{HP})$, which is proportional to the gradient $\partial f / \partial u$. Finally, closing the loop with an integrator drives the gradient to zero in steady state, provided that the closed-loop system is asymptotically stable; thus, resulting in an optimum control input.

In order to maximize the gradient information extracted, the phase of the demodulation signal θ is chosen to satisfy $\theta = \varphi_{in} + \varphi_{out} + \varphi_{HP}$.

3.2.2 ESC Design Guidelines

The ESC design guidelines in [16] have been used in this study, and are summarized as follows:

- Estimate the input dynamics based on open-loop tests.
- Choose the dither frequency within the bandwidth of the input dynamics.
- Choose the dither amplitude so that the dithered output has appropriate SNR at the dither frequency with respect to the portion of output due to measurement noise, external disturbance and process variation.
- Design the high-pass filter with highest possible cut-off frequency while the dither frequency remains in the pass band.
- Design the low-pass filter with highest possible bandwidth while providing satisfactory suppression on dither related harmonics.
- Determine appropriate phase shift angle between the additive dither $S(t)$ and the demodulating signal $M(t)$ to compensate for the phase change caused by plant dynamics and the high-pass filter. That is, $\theta = \varphi_{in} + \varphi_{out} + \varphi_{HP}$.
- Choose an integrator gain and, if necessary, add phase lead compensation to improve the transient performance.

Note that larger integrator gain generally results in faster convergence speed, while too large a gain could destabilize the ESC system. With moderate knowledge of the Hessian of the underlying static map, various stability conditions near the optimum have been obtained [43][16][44].

A crucial parameter for ESC design is the dither frequency. For single-input ESC, the selection of dither frequency depends on input/output dynamics only. For two-input ESC the dither frequencies should be distinct, as explained in [16][43].

For the field tests on the CART3 facility, the ESC is applied to determine the optimal settings for the following scenarios of control input: 1) torque gain k_t only, 2) blade pitch angle β only, 3) both torque gain k_t and blade pitch angle β.

3.3 ESC Integrator with Saturation

As mentioned in subsection 3.2, the integral gain k has major influence in the convergence rate of ESC: the larger gain the faster the convergence rate. However, too large gain leads to overshoot in the search process or even instability. Small integrator gain increases the degree of stability; however, it would result in slower convergence speed. In the Region-2 control problem, the wind speed significantly affects the variation of power output even with fixed torque gain and blade pitch angle. As a result, the ESC convergence rate can be greatly affected by the wind speed as shown in the following analysis.

The rotor power (mechanical power extracted from the wind) of a wind turbine is given by [67]

$$P = \frac{1}{2}\rho\pi R^2 V^3 C_P \tag{3-6}$$

where V is the effective wind speed acting on the rotor plane, R is the rotor plane radius and ρ is the air density. For the case of torque-gain ESC, the search process is driven by the gradient of the rotor power with respect to torque gain k_t, i.e. $\partial P/\partial k_t$. Taking the derivative of rotor power with respect to k_t yields

$$\frac{\partial P}{\partial k_t} = \frac{1}{2}\rho \pi R^2 V^3 \frac{\partial C_P}{\partial k_t} \tag{3-7}$$

For typical Region-2 operation, the variation in $\partial C_p / \partial k_t$ across the possible operating conditions is significantly smaller than the variation due to the wind speed factor V^3. Table 3.1 summarizes the C_P profile of the CART3 as function of torque gain and blade pitch angle, with 6 m/s, 9 m/s and 12 m/s constant wind speeds. Note that "Sat." in the 12 m/s columns represents the cases where the generator torque is saturated at the rated value.

Table 3.1. C_P variation with wind speed, torque gain and pitch angle for CART3 model

Wind Speed	6 m/s					9 m/s					12 m/s				
Pitch (°)	0	1	2	3	4	0	1	2	3	4	0	1	2	3	4
Torque Gain (Nm/(rad/s)^2)															
6000	0.409	0.425	0.439	0.453	0.459	0.411	0.426	0.441	0.454	0.461	0.416	0.433	0.448	0.462	0.469
7000	0.420	0.434	0.448	0.460	0.464	0.422	0.436	0.450	0.462	0.465	0.427	0.441	0.455	0.468	0.472
8000	0.428	0.442	0.455	0.465	0.466	0.429	0.444	0.457	0.467	0.468	0.434	0.448	0.461	0.472	0.474
9000	0.435	0.449	0.460	0.468	0.468	0.436	0.450	0.462	0.470	0.470	0.440	0.454	0.466	0.474	0.474
10000	0.439	0.453	0.465	0.471	0.468	0.439	0.454	0.466	0.472	0.470	0.442	0.458	0.470	0.476	0.474
11000	0.442	0.457	0.468	0.472	0.469	0.441	0.457	0.469	0.473	0.470	0.444	0.461	0.472	0.477	0.474
12000	0.443	0.459	0.470	0.473	0.468	0.443	0.458	0.471	0.474	0.470	0.446	0.461	0.474	0.477	0.473
13000	0.443	0.459	0.470	0.472	0.467	0.445	0.459	0.470	0.474	0.469	0.448	0.461	Sat.	Sat.	0.472
14000	0.442	0.457	0.468	0.471	0.466	0.446	0.457	0.467	0.472	0.467	0.449	Sat.	Sat.	Sat.	Sat.
15000	0.439	0.454	0.463	0.468	0.464	0.446	0.455	0.463	0.468	0.465	Sat.	Sat.	Sat.	Sat.	Sat.
16000	0.430	0.449	0.458	0.463	0.460	0.443	0.453	0.458	0.462	0.461	Sat.	Sat.	Sat.	Sat.	Sat.

The results shown in Table 3.1 reveal that a change of torque gain only results in a variation of power coefficient C_P no larger than 8.5%. Therefore, in this range of wind speeds, $\partial P / \partial k_t$ can be approximately seen as in proportional with the cube of wind speed; i.e., V^3. With a constant integrator gain, a larger wind speed yields larger gradient for the power map at a specific torque gain, which would result in faster convergence speed. To maintain a consistent convergence speed, smaller gain is needed for higher wind speed while larger gain is needed for lower wind speed.

Similarly, the gradient of rotor power with respect to blade pitch angle β is:

$$\frac{\partial P}{\partial \beta} = \frac{1}{2}\rho \pi R^2 V^3 \frac{\partial C_P}{\partial \beta} \tag{3-8}$$

Again, the change of $\partial C_p / \partial\beta$ is much smaller compared with the variation of the V^3 term in Equation (3-8). As shown in Table 3.1, for blade pitch angle from 0° to 4°, the C_P variation is about 12.7% from 6 to 12 m/s wind speed. Therefore, the gradient $\partial P/\partial\beta$ is also more sensitive with the variation of the V^3 term than with the variation of $\partial C_P/\partial\beta$. In other words, fluctuation in the wind speed have significant impact on the convergence rate of a blade-pitch ESC algorithm.

Since wind speed is not controllable and not measured for the ESC algorithm, a fixed-gain ESC would be exposed to highly variable (and potentially difficult to predict) convergence rates. In order to achieve a more consistent convergence rate, it is beneficial to adjust the ESC "loop gain" in response to large variations of the estimated gradient $\hat{g}$. In [49], we proposed to replace the integrator gain k in Figure 3.2 with the nonlinear modification shown in Figure 3.3.

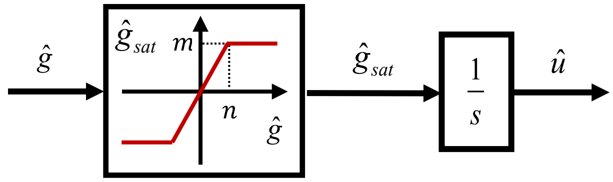

Figure 3.3. ESC integrator with saturation nonlinearity

In this block diagram, m is the saturation level for the estimated gradient, and n defines the linear range. Note that the ESC integrator with the saturation non-linearity may also be represented by the following equivalent integrator gain K:

$$K = \begin{cases} \dfrac{m}{\hat{g}}, & \hat{g} \in [n, \infty) \\ \dfrac{m}{n}, & \hat{g} \in (-n, n] \\ -\dfrac{m}{\hat{g}}, & \hat{g} \in (-\infty, -n] \end{cases} \tag{3-9}$$

The nonlinear gain scheme in Equation (3-9) is equivalent to first multiplying the estimated gradient by m/n, and then saturating it to the range of $[-m, m]$ prior to integration. In this fashion, the gain is self-adjustable according to the estimated gradient to achieve a more consistent convergence rate under fluctuating magnitude of the mean wind speed.

The proposed ESC scheme with nonlinearly saturated integrator is simulated with the FAST model of CART3 using uniform constant wind of 5 m/s and 10 m/s. The ESC parameter settings are summarized in Table 3.2. The simulation results are shown in Figure 3.4. Figure 3.4(a) and Figure 3.4(b) show the results of the torque-gain ESC, while the simulation results of blade pitch ESC are shown in Figure 3.4(c) and Figure 3.4(d). The calibrated optimum torque gain and blade pitch angle are 12000 N-m/(rad/s)^2 and 3.7°, respectively. ESC is engaged at 400 seconds.

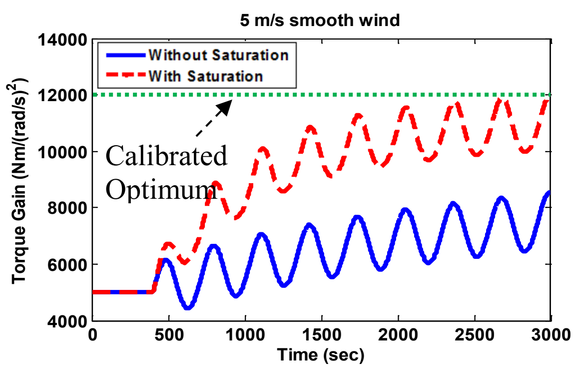

(a). Torque-gain ESC (5 m/s)

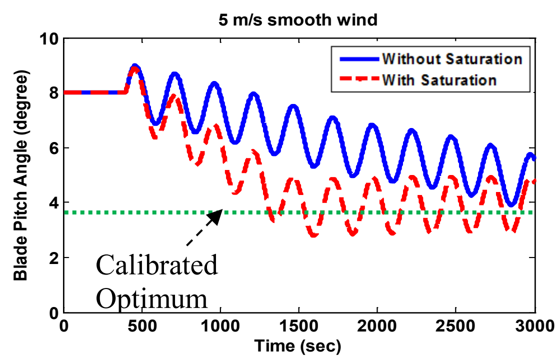

(c). Blade-pitch ESC (5 m/s)

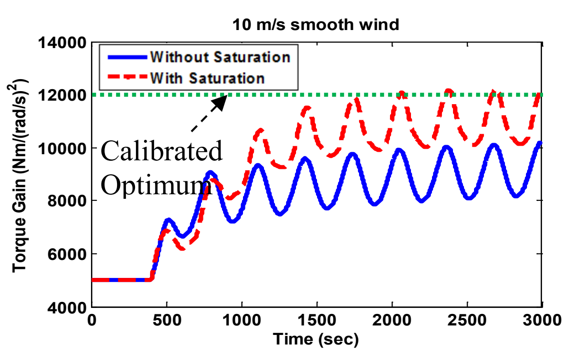

(b). Torque-gain ESC (10 m/s)

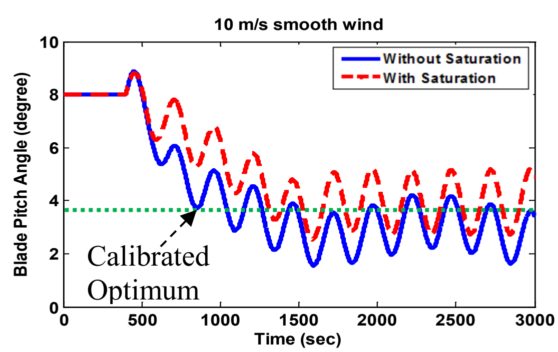

(d). Blade-pitch ESC (10 m/s)

Figure 3.4. Comparison of ESC transient performance with (dashed red) and without (solid blue) saturation nonlinearity under two different mean wind speeds

For the standard ESC with constant integrator gain, the convergence speed with 10 m/s wind is much faster than the 5 m/s case. With the proposed nonlinearly saturated integration, the convergence rate is much more consistent, despite variations in the wind speeds. The proposed saturation nonlinearity is implemented in the ESC controller developed for the field test on CART3 wind turbine.

Table 3.2. ESC parameters for CART3 simulation of integrator with saturation nonlinearity

Parameter		Torque-gain ESC	Blade-pitch ESC
Dither Frequency		0.02 rad/s	0.025 rad/s
Cut-off Frequency of LPF		0.015 rad/s	0.015 rad/s
Cut-off Frequency of HPF		0.018 rad/s	0.018 rad/s
Dither Amplitude		1000 N-m/(rad/s)^2	1°
Phase Compensator		0.43 radian	0.1 radian
Integrator Gain		3	0.002
Integrator with Saturation Nonlinearity	m	2	2
	n	0.25	0.25

3.4 ESC Design for CART3 Region-2 Operation

In this study, NREL's 600-kW CART3 facility is used for the experimental evaluation of the ESC based Region-2 control algorithm. Three ESC based Region-2 controllers are designed and tested to find the actual optimum settings for the "torque gain" and/or the "blade pitch angle." The experimental study is devoted to answering the following question: *Can the ESC algorithm determine the generator torque gain and/or blade pitch angle that maximize the real-time power production using the power measurement only?*

For evaluation purposes, the ESC field test results will be compared with those obtained with the NREL "baseline" controller. The key parameters of the CART3 turbine are given in Table 3.3.

Table 3.3. Key parameters of CART3 wind turbine

Parameter	Value	Unit
Tower Height	34.862	m
Hub Height	36.596	m
Rotor Diameter	40	m
Cut-in Wind Speed	4	m/s
Cut-out Wind Speed	25	m/s
Rated Wind Speed	11.7	m/s
Max. Generation Power	650	kW
Maximum Rotor Torque	162	kN-m
Rated Rotor Speed	41.7	rpm
Maximum Rotor Speed	58	rpm
Gearbox Ratio	43.165	---
Maximum Yaw Rate	0.5	°/s

3.4.1 Step Tests for CART3 Field Operation

As described in subsection 3.2.2, the dither frequency of the ESC should be selected within the bandwidth of the plant dynamics. For the implementation of ESC on CART3 wind turbine, and to attenuate the high frequency measurement noise, the power measurement is passed through a moving-average filter (averaging 400 samples per second) before it is processed by the ESC algorithm. This moving-average filter is effectively the output dynamics, and has a high bandwidth (~2.8 rad/sec) relative to the wind turbine dynamics. Thus, to simplify the design procedure, the input and output dynamics are combined into a single transfer function, i.e. $F_{in}^{'}(s) = F_{in}(s)F_{out}(s)$, which can be estimated from open-loop step test. Note from our design procedure that the main parameter to estimate is the overall phase lag of the combined input and output dynamics at the dither frequency, i.e. $\varphi_{in} + \varphi_{out}$.

Step test in simulation study is relatively straight forward, while for field operated wind turbines in fluctuating wind, the change in wind speed is an undesirable disturbance, which may distort the parameter identification. Therefore, it is desirable to perform step tests with relatively constant wind speed. To this end, an online wind speed slope estimator is adopted. As shown in Figure 3.5, a least-squares linear regression module is developed to estimate the slope of wind speed within a moving time window. If the slope is within the prescribed threshold (± 0.1 m/s^2), the step change in torque gain or blade pitch angle will be triggered.

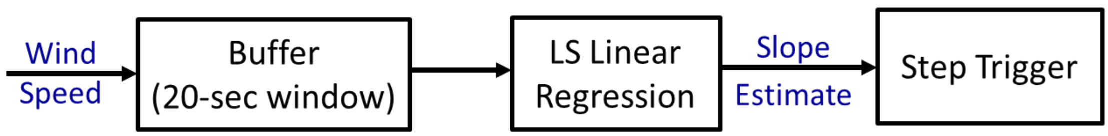

Figure 3.5. Step test of CART3 enhanced with wind speed slope estimation

For both torque gain and blade pitch input, the power output can be approximated by simple first-order dynamics. The time constant is determined by the natural logarithm method [68]. Table 3.4 summarizes the time constants estimated in several step tests performed on CART3.

Table 3.4. Estimated time constants from step response data

Torque-gain Time Constant (sec)	Blade-pitch Time Constant (sec)
5.09	5.71
4.7	3.57
4.37	3.14
4.04	2.91
4.04	2.91
4.34	2.9
3.07	2.86
3.08	2.75

The time constant varies as the wind turbine dynamics are intrinsically nonlinear. To enhance the robustness for the ESC to be tested, the largest time constant is adopted for the input dynamics estimation, i.e. 5.09 seconds and 5.71 seconds for the torque gain and the blade pitch input channel, respectively. The corresponding bandwidths of the overall dynamics are 0.2 rad/s for the torque gain and 0.18 rad/s for the blade pitch angle.

3.4.2 ESC Parameters Design

Based on the above estimates of input dynamics bandwidth, the dither frequencies are selected as 0.02 rad/s (~ 5 min period) and 0.05 rad/s (~ 2 min period) for the torque-gain and blade-pitch input channel, respectively.

Besides the frequency constraint imposed by the bandwidth of the plant, the dither frequencies should also avoid the resonant frequencies of the wind turbine and tower structure. The principal modes for CART3 [69][70] are listed in Table 3.5. The lowest structural mode is 5.4 rad/sec, which is much larger than the selected dither frequencies of 0.02 rad/s (torque-gain channel) and 0.05 rad/s (blade-pitch channel). This indicates that the dither actions would not excite any detrimental structural vibrations.

Table 3.5. Principle structure vibration modes for CART3 [69][70]

Mode #	Description	Frequency (Hz)	Frequency (rad/s)
1	1st model tower-base fore-aft bending moment	0.86	5.4
2	1st mode of tower-base side-to-side bending moment	0.88	5.53
3	1st mode of blade flap-wise bending moment	1.45-1.85	9.11-11.62
4	1st mode of blade edge-wise moment	3	18.85
5	1st torsional mode of drive-train	2.7	16.96

Figure 3.6 shows the Bode plots of the overall dynamics, low-pass and high-pass filters, with the dither frequencies labeled. Note that the dither signals are in the pass band of the wind turbine dynamics, the pass band of the HPF and the stop band of the LPF (there is one LPF per channel). The ESC parameters designed are summarized in Table 3.6.

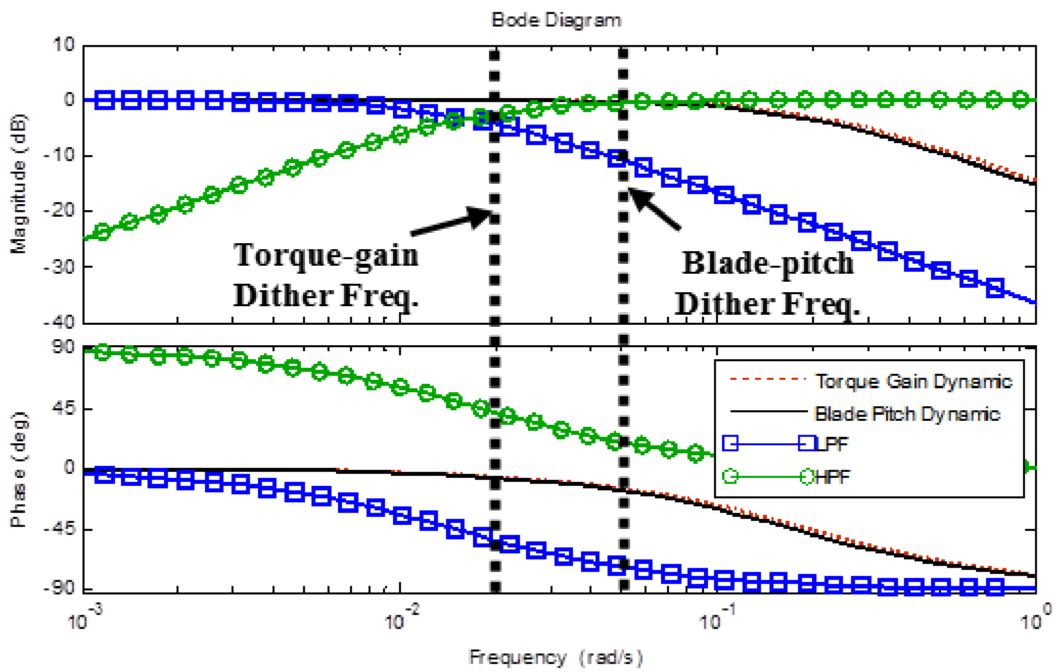

Figure 3.6. Bode plots of input dynamics, LPF, HPF and the dither frequencies

Table 3.6. ESC parameters for CART3 Region-2 controllers

Parameter		Torque-gain ESC	Blade-pitch ESC
Dither Frequency		0.02 rad/s	0.05 rad/s
Cut-off Frequency of LPF		0.015 rad/s	0.015 rad/s
Cut-off Frequency of HPF		0.018 rad/s	0.018 rad/s
Dither Amplitude		1500 N-m/(rad/s)^2	1.5°
Phase Compensator		0.63 radian	0.1 radian
Integrator Gain		1	1
Saturation Nonlinearity	m	6	0.004
	n	0.2	0.2

3.4.3 Switching between ESC Region-2 Controller and Baseline Controller

As described in [71], the CART3 baseline control is divided into four different regions based on the generator speed (see Figure 3.7). For the generator torque control, the baseline control adopts a constant torque gain reference of 6541.8 N-m/(rad/s)^2 in Region-2 operation, while in Region-3, the generator torque is fixed at the rated value of 3,524 N-m. To ensure the wind turbine reach the rated torque at the rated speed, a transitional Region-2.5 is introduced between Region-2 and Region-3 using a linear torque-speed relation. The generator speed for the transitional Region-2.5 is between 94% to 99% of the maximum generator speed (1800 rpm for CART3). The corresponding low-speed shaft speed is between 34.1 rpm and 36.7 rpm.

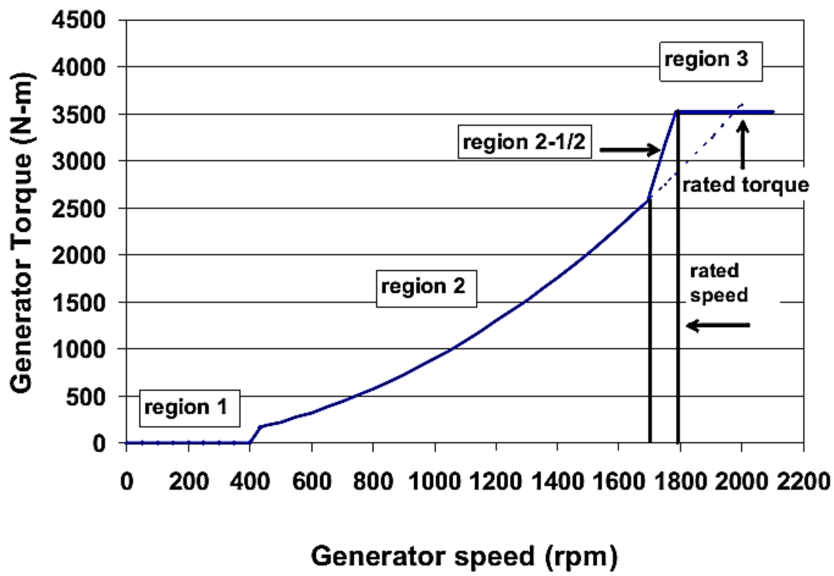

Figure 3.7. Baseline control scheme for four regions of CART3 operation [71]

For blade pitch control, the baseline control adopts a constant pitch angle reference of 3.7° for Region-2 and Region-2.5 operation; while for Region-3, the baseline controller engages a proportional-integral (PI) controller that manipulates the blade pitch angle to maintain the rated rotor/generator speed.

The focus of this study is the ESC based Region-2 controller, while the field operation of a wind turbine covers all regions. It is thus necessary to develop switching logic between the ESC Region-2 controller and the existing baseline controller outside Region-2. Also, to determine the performance of the ESC relative to the Region-2 baseline controller, it is necessary to switch between the ESC and baseline operations.

The ESC strategy is designed for Region-2 operation only. For torque-gain ESC testing, if the wind turbine exits Region-2 operation, the following two actions will be executed: 1) switch the torque-gain control from "ESC Control" to "Baseline Control", and 2) pause the ESC output (i.e. the torque gain reference). When the wind turbine returns to Region-2 operation, the torque-gain control will be switched back to "ESC Control", resuming from the previously paused values. To avoid possible discontinuity of generator torque command, a soft switching technique is implemented to gradually change the torque command to the new torque command during transitions between baseline control and ESC control. Similarly, the blade-pitch ESC is designed to work in both Region-2 and Region-2.5. If the turbine operation enters other regions, the following two actions will be taken: 1) switch the pitch control from "ESC Control" to "Baseline Control", and 2) pause the ESC output (i.e. the blade pitch reference). When the wind turbine returns to Region-2 or Region-2.5 operation, the blade-pitch control will be switched back to "ESC Control" by resuming from the previously paused values. The region switching scheme is summarized in Figure 3.8. Note that for safety operation, the rated generator speed is downsized from 1800 rpm to 1600 rpm.

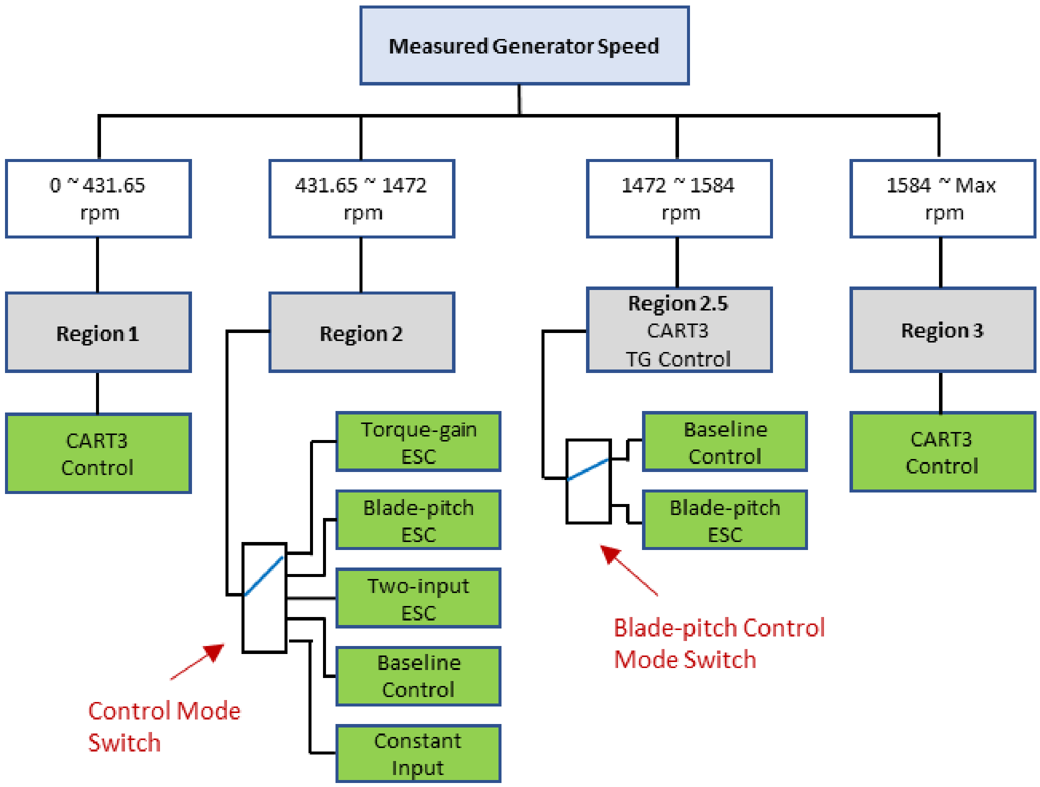

Figure 3.8. Controller switching for CART3 ESC testing

3.5 CART3 Field Testing Results for ESC Based Region-2 Control

This section presents the results of the field test on the CART3 facility for the three ESC based Region-2 controllers, as designed in the previous section. The CART3 is a three-blade, 600-kW wind turbine located at the National Wind Technology Center (NWTC) of NREL. A LabVIEW based control system (CART-SCADA) has been developed, with sampling rate of up to 400 Hz. Controllers implemented in Matlab/Simulink can be compiled into executable codes with dynamic link library (DLL), making control testing highly customizable [72][73].

To evaluate the performance of the ESC algorithms, hub-height (36.6 m) wind measurements from Met Tower 4.2 are collected. Figure 3.9 illustrates the relative position between Met Tower 4.2 and CART3.

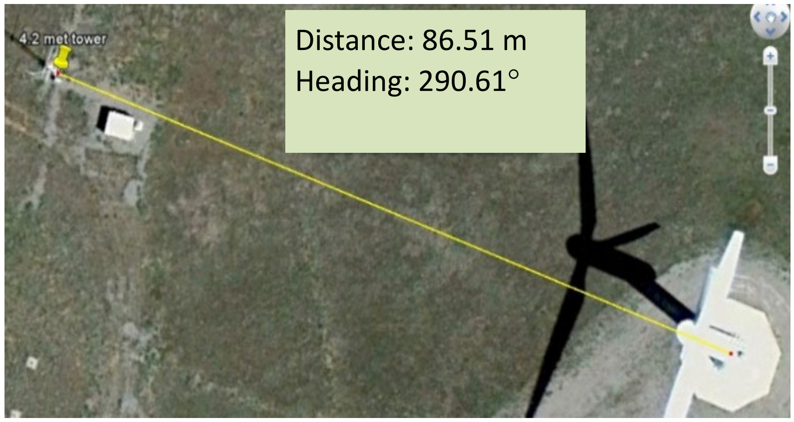

Figure 3.9. Relative position between Met Tower 4.2 and CART3 [74]

Following Johnson [75], we evaluate the performance of the ESC algorithms using a "normalized power" figure of merit:

$$P_N = \frac{\overline{P}}{\frac{1}{2}\overline{\rho} A \overline{V}^3 \cos^3 \overline{\psi}} \tag{3-10}$$

where

$$\overline{P} = \frac{1}{N}\sum_{i=1}^{N} P(i) \qquad \overline{V} = \frac{1}{N}\sum_{i=1}^{N} V(i + t_{shift})$$

$$\overline{\rho} = \frac{1}{N}\sum_{i=1}^{N} \rho(i) \qquad \overline{\psi} = \frac{1}{N}\sum_{i=1}^{N} \psi(i + t_{shift})$$

With N = 100 seconds, $\overline{P}$, $\overline{V}$, $\overline{\rho}$ and $\overline{\psi}$ stand for 100-second average of rotor power, wind speed, air density and yaw error, respectively. V is the wind speed measurements from Met Tower 4.2 at the height of 36.6 m, which is approximately the CART3 hub height. Also, both yaw error and the wind propagation time t_{shift} from the Met tower to the turbine rotor are compensated in the calculation of P_N. The propagation time t_{shift} is estimated through maximum cross correlation between the hub-height Met tower wind speed and the nacelle-top wind speed, rounded to the nearest integer second.

Three different tests were performed on CART3 wind turbine: 1) torque-gain ESC, 2) blade-pitch ESC, and 3) two-input (torque-gain + blade-pitch) ESC. The benchmark controller is the baseline design provided by NREL for Region-2 operation, which has constant torque gain k_t = 6541.8 N-m/(rad/s)^2 and constant blade pitch angle β = 3.7° as described in subsection 3.4.3. The evaluation of each controller (baseline and ESC) is done using two hours of test data sampled at 400 Hz.

3.5.1 Torque-gain ESC Field Tests

The field tests of the torque-gain ESC are performed with the following testing sequence:

1. NREL baseline torque gain of 6541.8 Nm/(rad/s)^2 for 30 minutes.
2. Low torque gain of 3000 Nm/(rad/s)^2 for 30 minutes
3. ESC starting from the low torque gain of 3000 Nm/(rad/s)^2 and run for 60 minutes
4. NREL baseline torque gain of 6541.8 Nm/(rad/s)^2 for 30 minutes
5. High torque gain of 14000 Nm/(rad/s)^2 for 30 minutes
6. ESC starting from the high torque gain of 14000 Nm/(rad/s)^2 and run for 60 minutes
7. Repeat from Step 1

The torque-gain ESC parameters summarized in Table 3.6 are used in this test. Figure 3.10 shows two examples of field test trajectories for the torque-gain ESC case, in which Figure 3.10(a) shows a case that ESC starting with the high initial value (14000 Nm/(rad/s)^2), while Figure 3.10(b) shows a case that ESC starting with a low initial value (3000 Nm/(rad/s)^2).

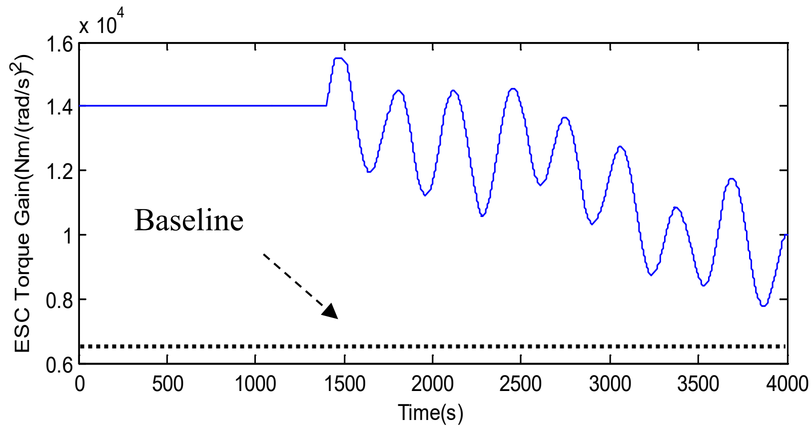

(a). Torque-gain ESC with high initial value

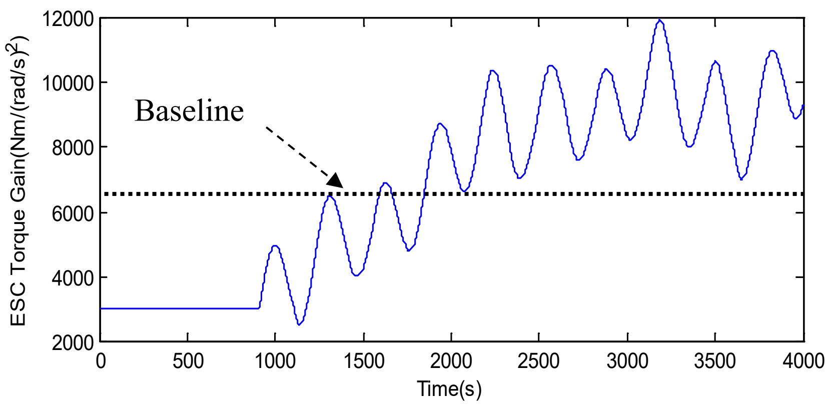

(b). Torque-gain ESC with low initial value

Figure 3.10. CART3 sample test data for torque-gain ESC (solid line) and NREL baseline torque-gain value (dashed)

Due to changes in wind condition during ESC operations (i.e. steps 3 and 6 in the above sequence), valid ESC test data are not available for the full hour allocated to the ESC controller. Basically, the wind speed has decreased and the turbine is no longer in Region-2 operation. The dashed lines in Figure 3.10 represent the value of the NREL baseline torque gain (6541.8 N-m/(rad/s)^2). Note that ESC decreases (Figure 3.10(a)) or increases (Figure 3.10(b)) toward the NREL baseline.

To evaluate the performance of the ESC controller in the presence of changing wind conditions, we use the following protocol:

1. Eliminate non-Region-2 data segments
2. Eliminate any data segment where the NREL over-ride torque controller became active to avoid the critical rotor speed corresponding to the tower structure
3. Calculate "normalized power data points" using data segments of sufficient duration to average power over a continuous time interval

Using this protocol, we have obtained 72 data points where the power is calculated by averaging the instantaneous measured power (sampled at 400 Hz) over a 100-second time window. That is, each data point results from averaging 40,000 samples of power data and wind data.

The histograms of the estimated normalized power P_N are shown in Figure 3.11.

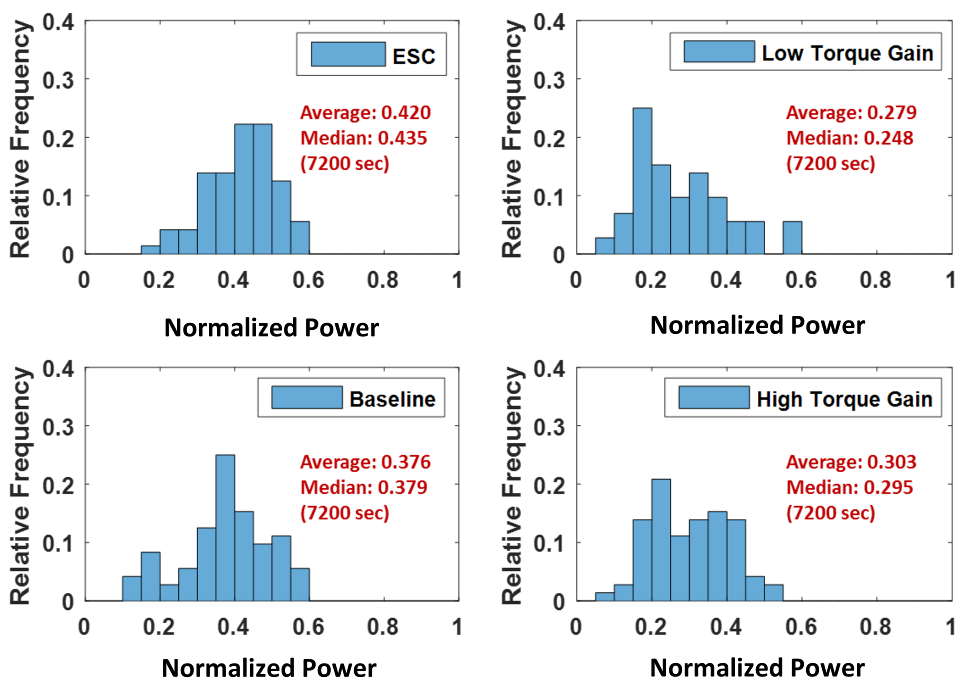

Figure 3.11. P_N histograms for torque-gain ESC and comparative scenarios

As can be seen, the average (median) value of P_N with ESC is 0.420 (0.435), compared with 0.376 (0.379) for the NREL baseline torque gain. Thus, torque-gain ESC exhibits about 12% higher energy capture than the NREL baseline torque gain. Both the High-Torque-Gain and Low-Torque-Gain cases show much smaller average P_N than those of ESC and baseline cases.

The distribution of the 72 normalized power data points P_N are shown in Figure 3.12. The data is visualized using box plots to provide a concise representation of the normalized power distribution for each controller. Each box shows the median (red line), the 25th percentile (box base) and the 75th percentile (box top) corresponding to 72 data points. The whiskers (dashed lines) show the maximum and minimum values extending 1.5 times the interquartile range above the 75th percentile (max) and below the 25th percentile (min). Data points outside this range (+ sign) are considered outliers. The median normalized power P_N with ESC is 0.435 compared with 0.379 for the NREL baseline torque gain. This represents a 15% increase in the median normalized power.

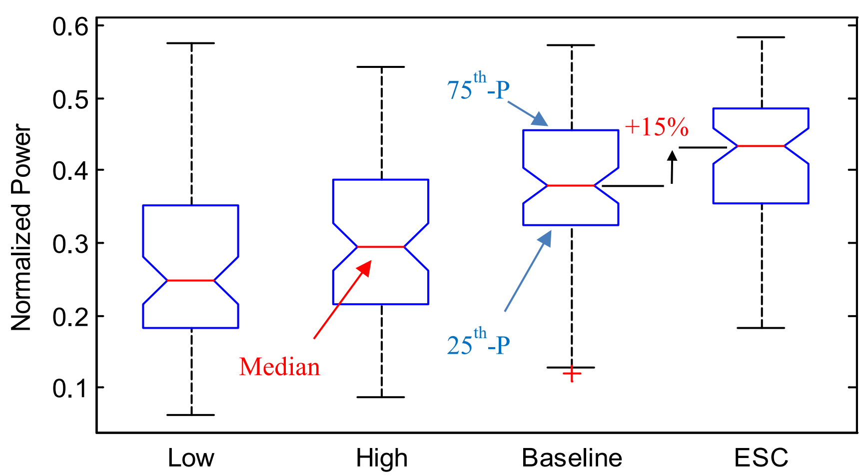

Figure 3.12. P_N distribution for the torque-gain ESC and the comparison controllers, distributions are visualized with box plot

Figure 3.13 shows the normalized Damage Equivalent Loads (DEL) values of selected turbine loads for all the afore-mentioned cases. The DEL is the standard metric used to evaluate fatigue loads in wind turbines. As wind induced aerodynamic loads are proportional to the square of wind speed, loads calculations are normalized to compare DELs at different wind speeds.

Similar to the calculation of the normalized power P_N, the DEL estimations are normalized with respect to the variations of air density ρ, wind speed V and yaw error $\bar{\psi}$. The measured structural loads M_{meas} can be approximately estimated as in proportional with the aerodynamic force exerted on the wind turbine. Based on such consideration, the measured structural loads are normalized as

$$M_{norm} = \frac{M_{meas}}{\bar{\rho}\bar{V}^2 \cos^2 \bar{\psi}} \tag{3-11}$$

The normalized loads are then used to calculate the corresponding DELs with NREL's MCrunch software [76]. The air density $\bar{\rho}$, wind speed $\bar{V}$ and yaw error $\bar{\psi}$ shown in Equation (3-11) are the average value based on 100 seconds of data.

Then, the DEL values obtained for all scenarios are normalized with the baseline results (unity in the bar graph in Figure 3.13). The DELs considered are the following: B1EM, B2EM and B3EM denote the blade-root edge-wise bending moments for blades #1, #2 and #3, respectively. B1FM and B2FM denote the blade-root flap-wise bending moments for blades #1 and #2, respectively. The measurement of blade #3 flap-wise bending moment was faulty and thus unavailable. TwrSS and TwrFA denote the tower-base side-side and fore-aft bending moments, respectively. STR denotes the shaft torsional rate of the drive train.

The mean values of calculated normalized power and load indices in Figure 3.11 and Figure 3.13 are summarized in Table 3.7. For the load variables evaluated, ESC shows increase in DEL, about 3%~14% in the average value over the NREL baseline control.

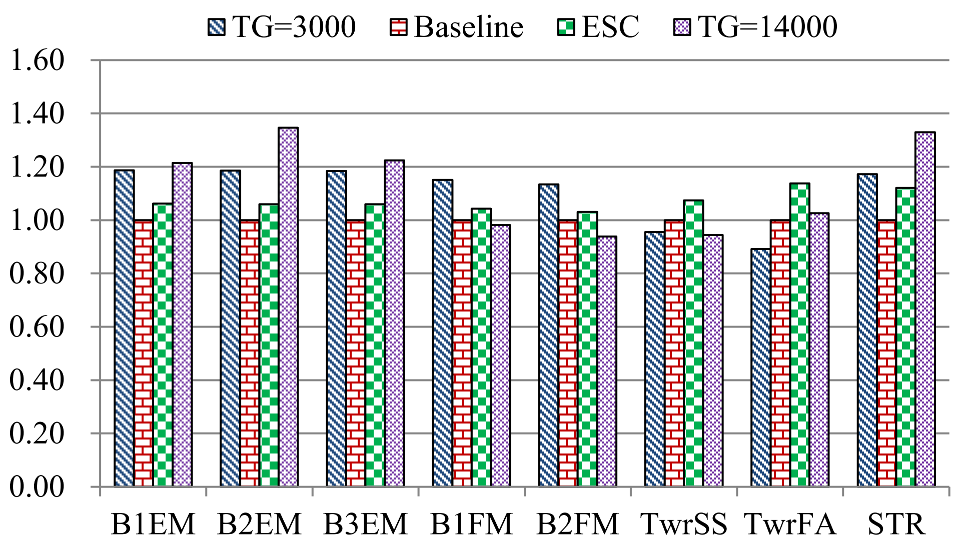

Figure 3.13. Normalized DEL values of selected load variables for CART3 testing of torque-gain ESC and comparative scenarios

Table 3.7. Energy capture and load indices for CART3 testing of torque-gain ESC and comparative scenarios

Index	**Baseline**	**Torque-gain ESC**	**Low Torque Gain**	**High Torque Gain**
P_N	1	+12%	−26%	−19%
B1EM	1	+6%	+19%	+21%
B2EM	1	+6%	+19%	+35%
B3EM	1	+6%	+18%	+22%
B1FM	1	+4%	+15%	-2%
B2FM	1	+3%	+13%	-6%
TwrSS	1	+7%	-4%	-6%
TwrFA	1	+14%	-11%	+3%
STR	1	+12%	+17%	+33%

Figure 3.14 shows the wind-speed histograms for the afore-mentioned four scenarios, using the hub-height measurement at the met tower.

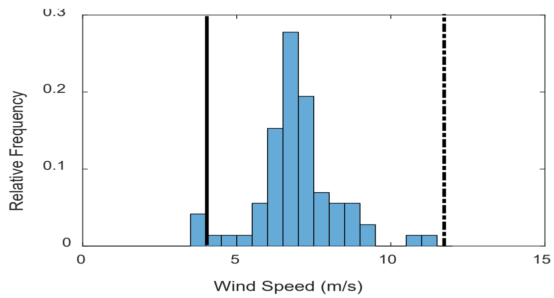

(a). ESC (mean: 6.98 m/s)

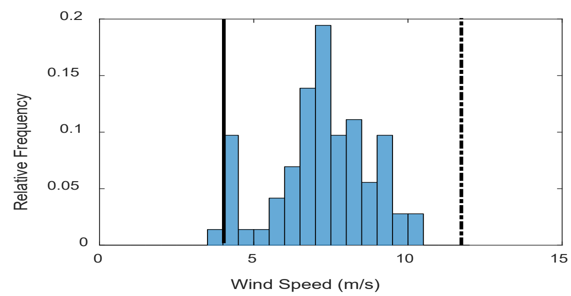

(b). Baseline (mean: 7.24 m/s)

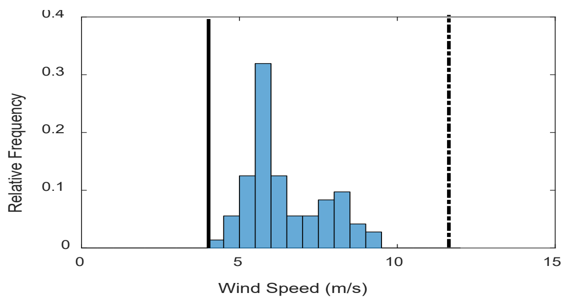

(c). Low torque gain (mean: 6.42 m/s)

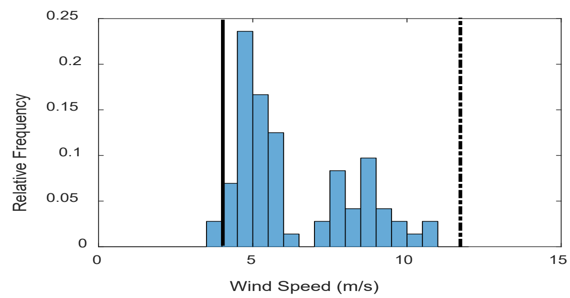

(d). High torque gain (mean: 6.35 m/s)

Figure 3.14. Wind speed histograms (based on 7200 seconds of data) for CART3 testing of the torque-gain ESC and comparative scenarios. Vertical solid lines denote the cut-in speed (4 m/s). Dash-dot line represents the rated wind speed (11.7 m/s)

Figure 3.15 shows the wind-speed box plots for the four controllers tested. Wind speeds are from the hub-height measurement at the met tower. The rated wind speed (11.7 m/s) and the cut-in wind speed (4 m/s) are plotted as horizontal dashed lines. The wind speed data confirms that the normalized power distributions shown in Figure 3.12 come from Region-2 operation.

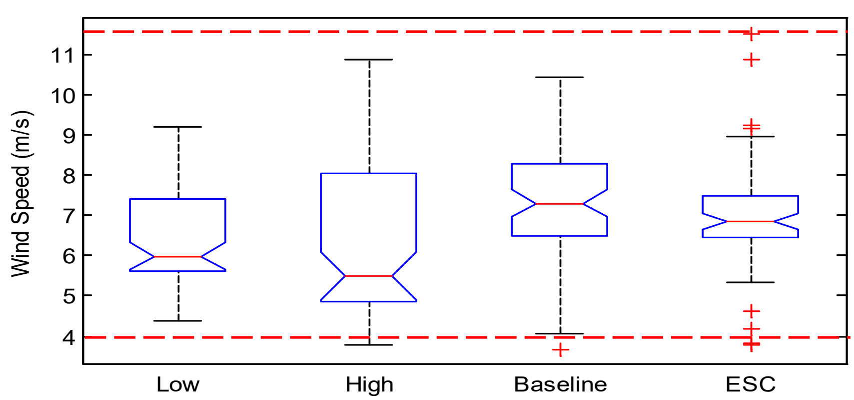

Figure 3.15. Wind speed distribution (box plots) for each torque-gain controller tested. Dashed red lines indicate rated wind speed and cut-in wind speed.

The wind roses plots from the wind measurements during the field test are shown in Figure 3.16. Note from Figure 3.14 that wind speeds for ESC and baseline are comparable. Wind direction, however, is different (Figure 3.16) for these two tests.

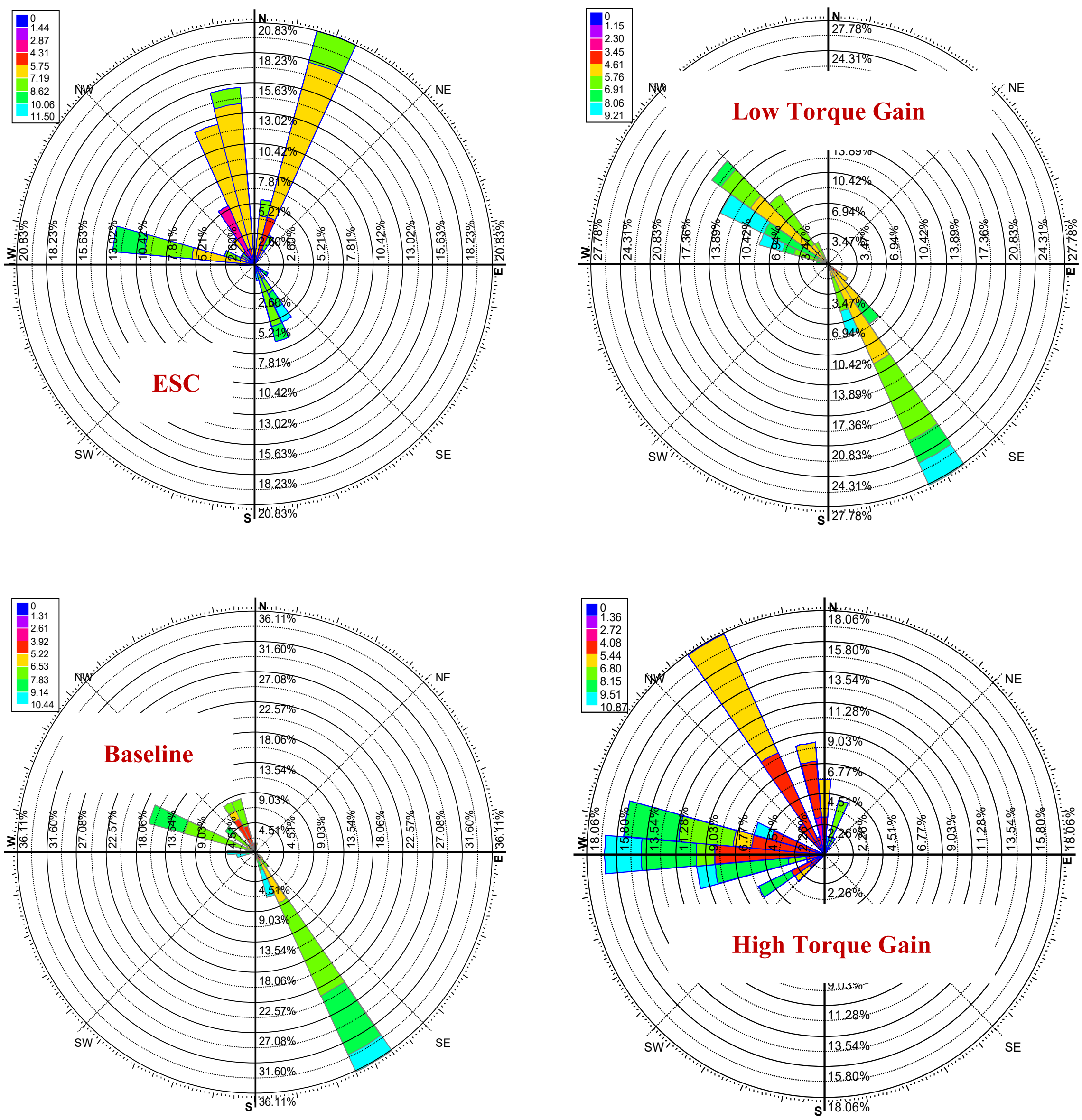

Figure 3.16. Wind roses for CART3 testing of the torque-gain ESC and comparative scenarios

3.5.2 Blade-pitch ESC Field Tests

The blade-pitch ESC field tests are performed using the parameters summarized in Table 3.6, with the following testing sequence implemented:

1. NREL baseline blade pitch of 3.7° for 30 minutes
2. High blade pitch of 10° for 30 minutes
3. ESC for 60 minutes, from the initial blade pitch of 10°
4. NREL baseline blade pitch of 3.7° for 30 minutes
5. Low blade pitch of 0° for 30 minutes
6. ESC for 60 minutes, from initial blade pitch of 0°
7. Repeat from Step 1

Figure 3.17 shows two examples of blade pitch angle trajectories from field tests of the blade-pitch ESC. Figure 3.17(a) shows a case with a high initial blade pitch at 10°, while Figure 3.17(b) shows a case with a low initial value at 0°. Again, due to changes in wind conditions during ESC operations (i.e. steps 3 and 6 in the operational sequence described above), the full-hour ESC operation was not possible as the wind speed dropped below the cut-in wind speed. The dashed lines in Figure 3.17 represent the value of the NREL baseline blade pitch of 3.7°. For both of the two cases, ESC converges to a blade pitch angle slightly smaller than NREL's baseline blade pitch angle.

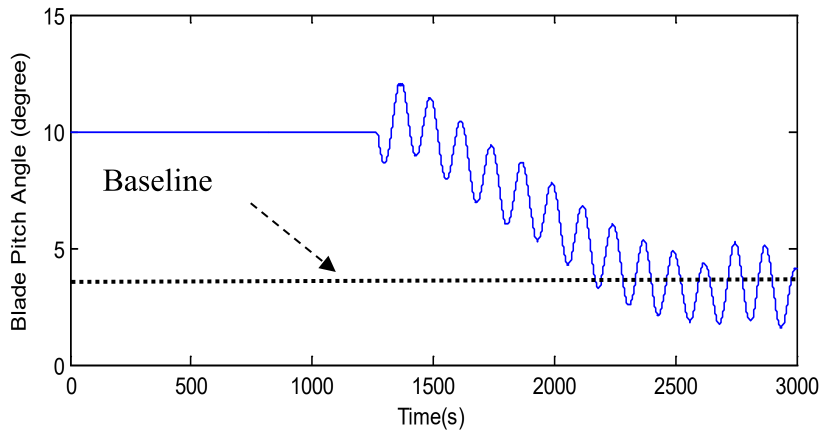

(a). Blade-pitch ESC with high initial value

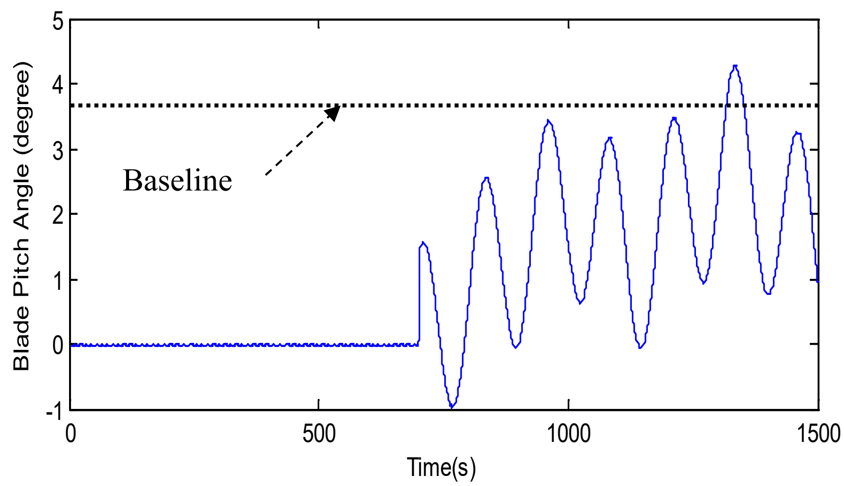

(b). Blade-pitch ESC with low initial value

Figure 3.17. Examples of CART3 field test (blade-pitch ESC)

To evaluate the performance of the ESC algorithm, the histogram of the normalized power P_N is calculated and shown in Figure 3.18. The duration of data records for ESC, Baseline, Low Blade Pitch and High Blade Pitch are all 7200 seconds. The average normalized power with the ESC controller and the NREL baseline controller are 0.346 and 0.319, respectively. The ESC improves the average value of the normalized power by 8% over the NREL baseline blade pitch angle.

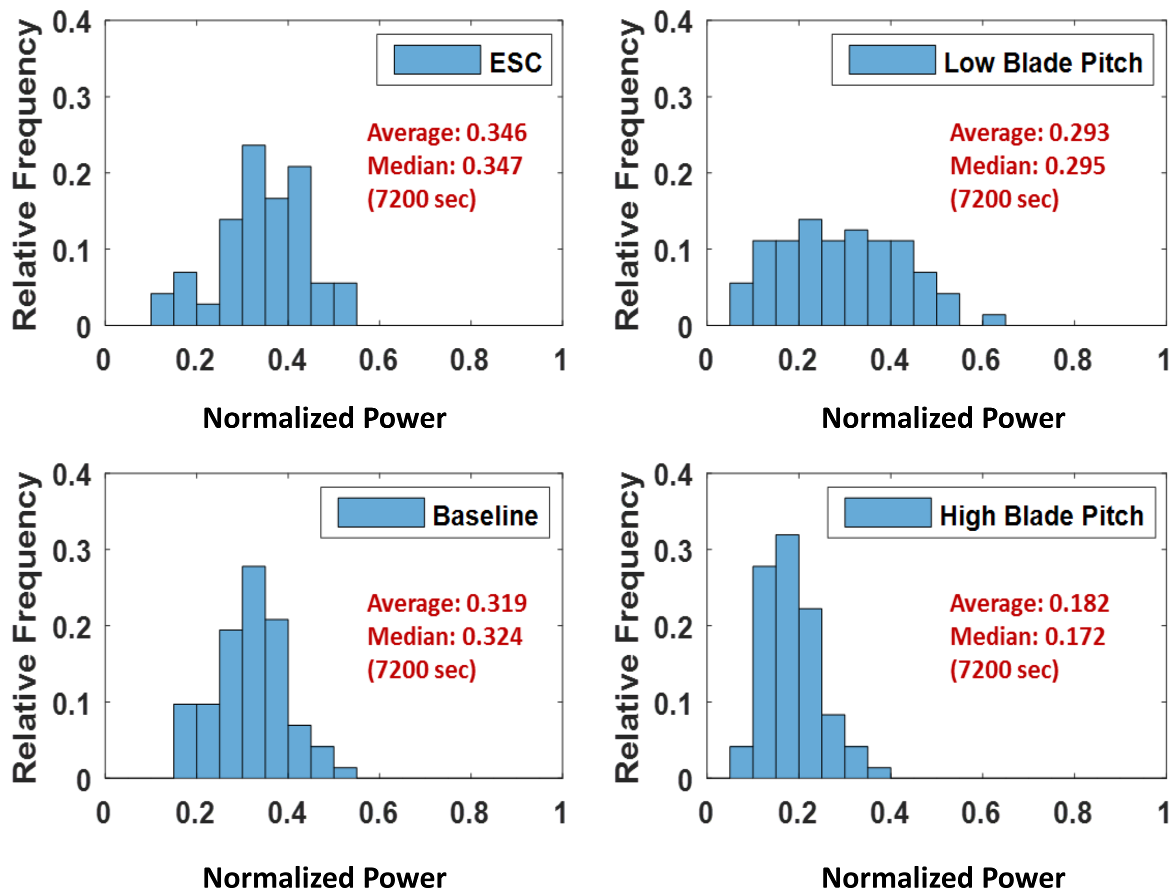

Figure 3.18. P_N histograms of CART3 testing of the blade-pitch ESC and comparative scenarios

The box plots of the normalized power P_N are shown in Figure 3.19. The protocol used to generate each data point is identical to the one described in the torque-gain ESC field test. The median value of the normalized power P_N with ESC is 0.347, while the NREL baseline blade pitch angle yields 0.324. Thus, ESC increases the median normalized power by 7% compared with the NREL baseline blade pitch angle.

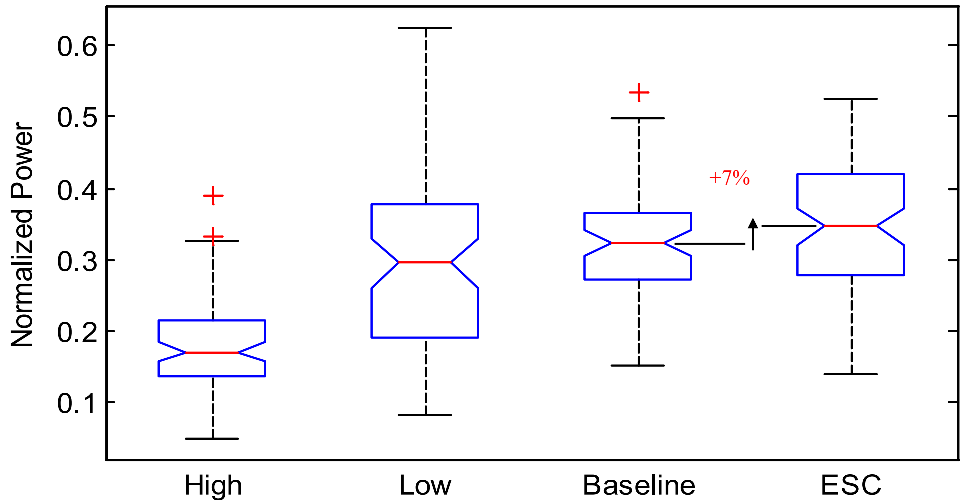

Figure 3.19. P_N box plots of CART3 testing of the blade-pitch ESC and comparative scenarios

Figure 3.20 compares the normalized DEL values of the selected fatigue loads for the aforementioned four cases, with the baseline results normalized to unity. The normalized value of energy capture performance and load indices are summarized in Table 3.8. The DEL values of the blade-pitch ESC are in general smaller than or similar to those of the baseline case, except for the slight increase (1%~5% on average) in the blade-root flap-wise bending moments.

It is noteworthy that the blade-root edgewise bending moments are consistently reduced with the blade pitch ESC, compared with the baseline controller. Using high blade pitch angle significantly reduces the energy capture (reduced by 43% compared with NREL Baseline blade pitch angle), while inducing mild increase (12% - 18%) of the blade-root edge-wise bending moments and blade-root flap-wise bending moments.

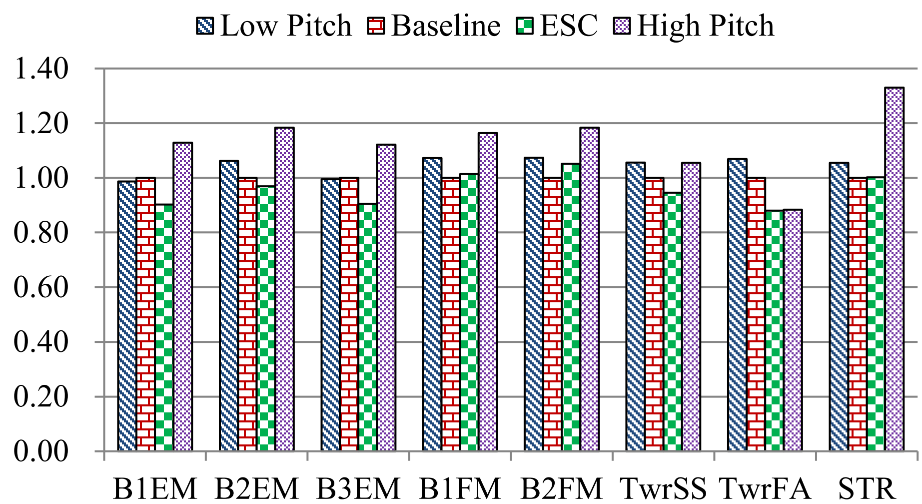

Figure 3.20. Normalized DEL values of selected load variables for blade-pitch ESC testing on CART3 and comparative scenarios

Table 3.8. Average energy capture and load indices for CART3 testing of blade pitch ESC and comparative scenarios

Index	Baseline	Blade-pitch ESC	Low Blade Pitch	High Blade Pitch
P_N	1	+8%	–8%	–43%
B1EM	1	-10%	-1%	+13%
B2EM	1	-3%	+6%	+18%
B3EM	1	-10%	-0.5%	+12%
B1FM	1	+1%	+7%	+16%
B2FM	1	+5%	+7%	+18%
TwrSS	1	-5%	+6%	+5%
TwrFA	1	-12%	+7%	-12%
STR	1	+0.2%	+6%	+33%

The histograms of the wind speed, the box plots of the wind speed and the wind roses for the blade pitch ESC and the comparative scenarios are shown by Figure 3.21, Figure 3.22 and Figure 3.23, respectively, with all data obtained from Met Tower 4.2 measurements at the hub height of CART3. From Figure 3.22, it is clear to see that the testing data for evaluation are below the rated wind speed.

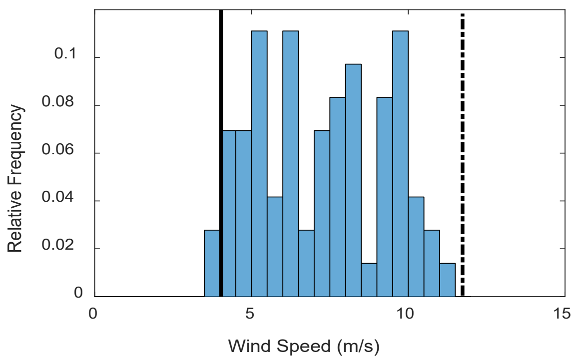

(a). ESC (mean: 7.25 m/s)

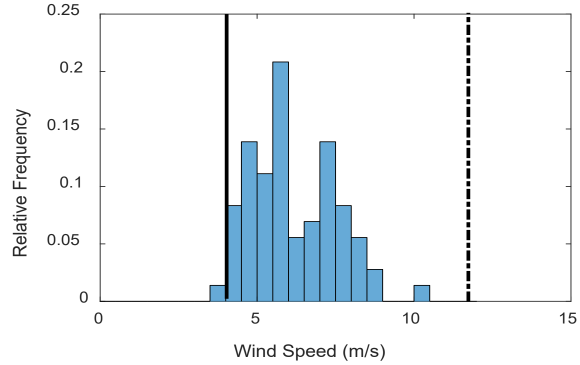

(b). Baseline (mean: 6.16 m/s)

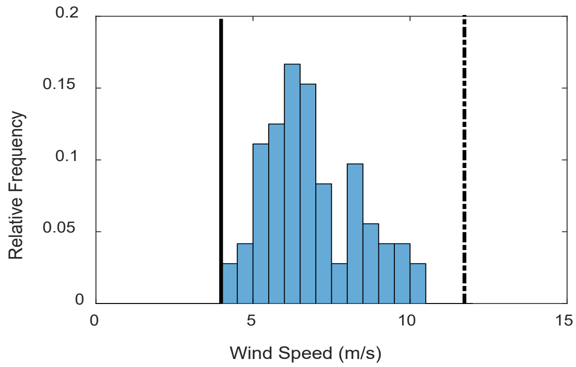

(c). Low blade pitch (mean: 6.88 m/s)

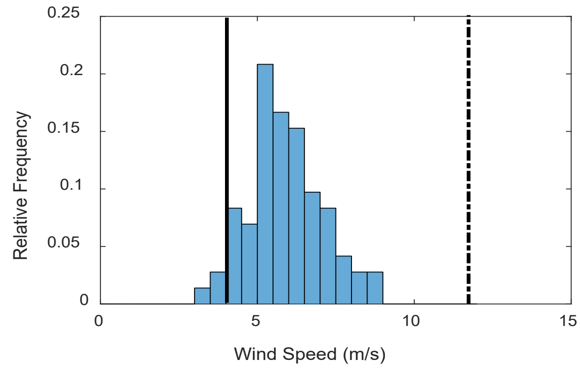

(d). High blade pitch (mean: 5.9 m/s)

Figure 3.21. Wind speed histograms (based on 7200 seconds of data) for CART3 testing of the blade-pitch ESC and comparative scenarios. Vertical solid lines denote the cut-in speed (4 m/s). Dash-dot line represents the rated speed (11.7 m/s)

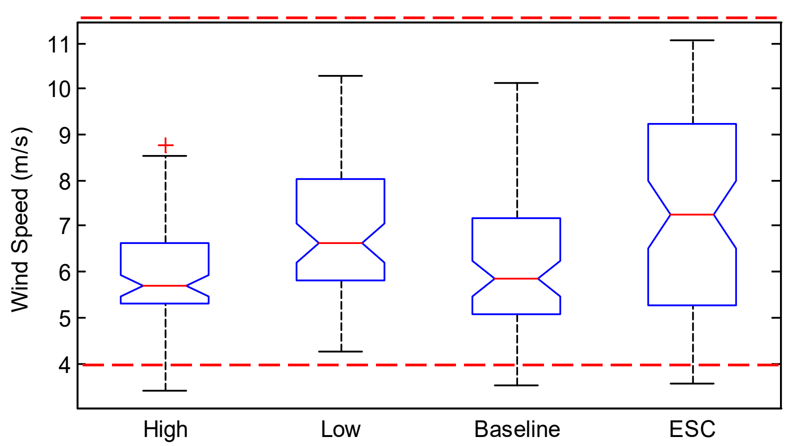

Figure 3.22. Wind speed distribution (box plots) for each blade pitch controller tested. Dashed red lines indicate rated wind speed and cut-in wind speed.

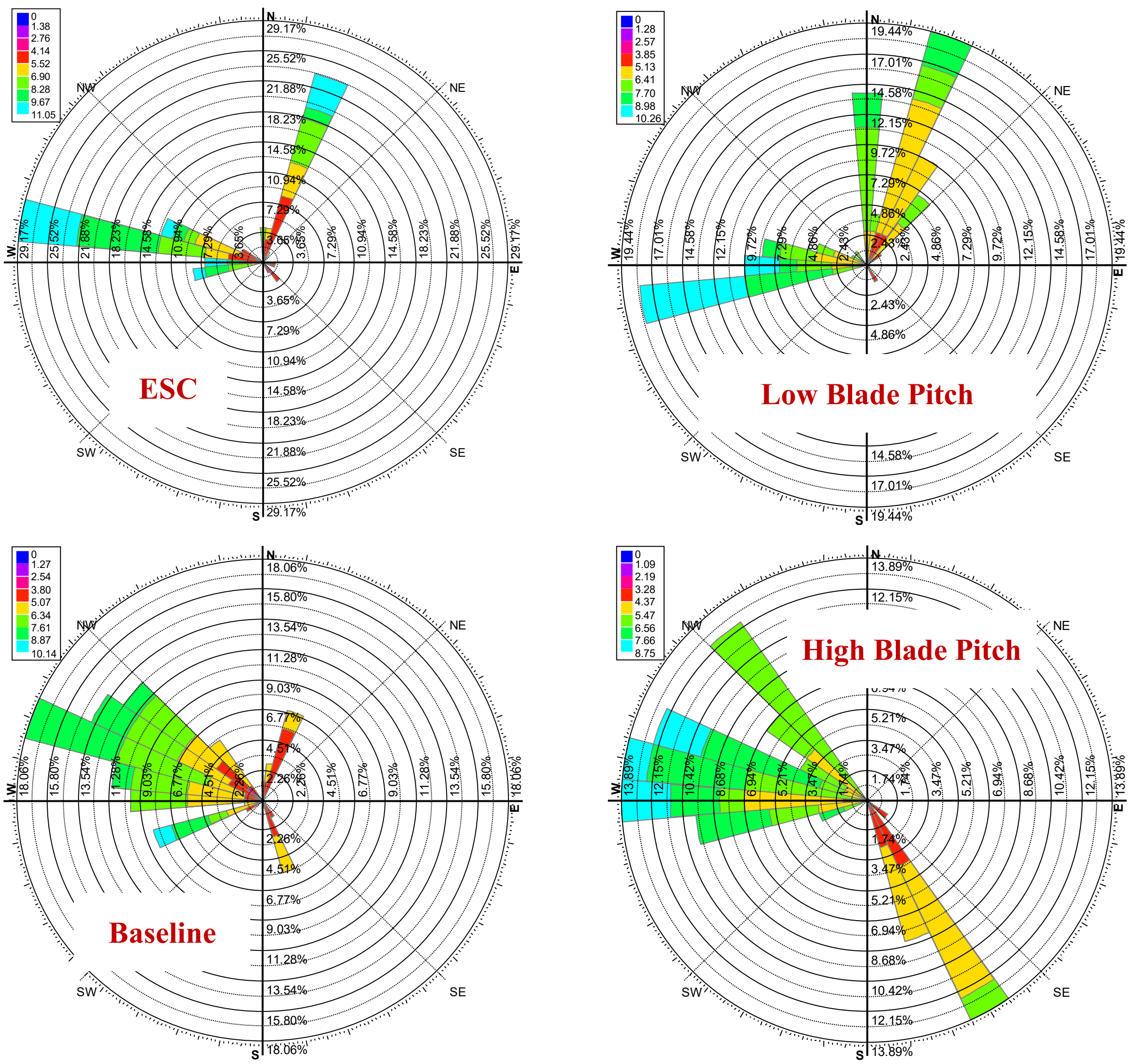

Figure 3.23. Wind roses for CART3 testing of the blade-pitch ESC and comparative scenarios

3.5.3 Two-input ESC Field Tests

For the two-input ESC field tests, the ESC parameters shown in Table 3.6 are adopted. The field tests are performed using the following testing sequence:

1. NREL baseline controller for 30 minutes.
2. Low torque gain of 3,000 N-m/(rad/s)^2 and high blade pitch of 10° for 30 minutes.

3. Run ESC with the initial control inputs as the setting in Step 2 for 60 minutes.
4. NREL baseline controller for 30 minutes.
5. Low torque gain of 3,000 N-m/(rad/s)^2 and low blade pitch of 0° for 30 minutes.
6. Run ESC with the initial control inputs as the setting in Step 5 for 60 minutes.
7. NREL baseline controller for 30 minutes.
8. High torque gain of 14,000 N-m/(rad/s)^2 and high blade pitch of 10° for 30 minutes.
9. Run ESC with the initial control inputs as the setting in Step 8 for 60 minutes.
10. NREL baseline controller for 30 minutes.
11. High torque gain of 14,000 N-m/(rad/s)^2 and low blade pitch of 0° for 30 minutes.
12. Run ESC with the initial control inputs as the setting in Step 11 for 60 minutes.
13. Repeat from Step 1

The histograms of the normalized power P_N are shown in Figure 3.24, with both mean and median values calculated. The data size for each scenario is 7200 seconds, while the respective average values of normalized power are 0.347, 0.310, 0.171, 0.185, 0.313 and 0.222. ESC demonstrates about 12% higher energy capture than the NREL baseline control.

The normalized power P_N distributions are shown in Figure 3.25, with the median value indicated by the red lines. The median normalized power P_N with the two-input ESC controller is 0.358, while the NREL baseline control yields 0.327. Thus, ESC increases the median normalized power by 10% relative to the baseline control.

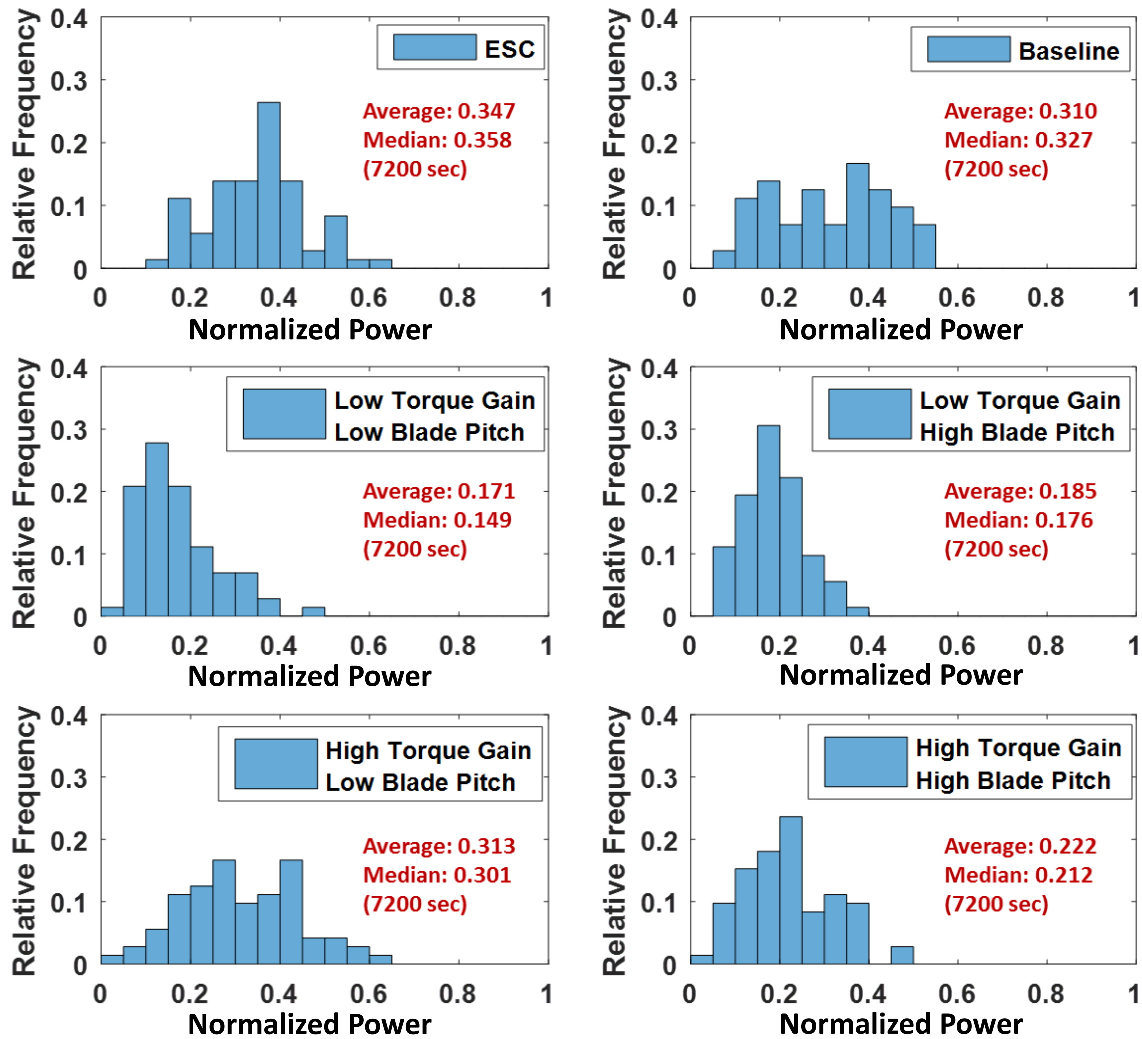

Figure 3.24. P_N histograms for CART3 testing of the two-input ESC and comparative scenarios

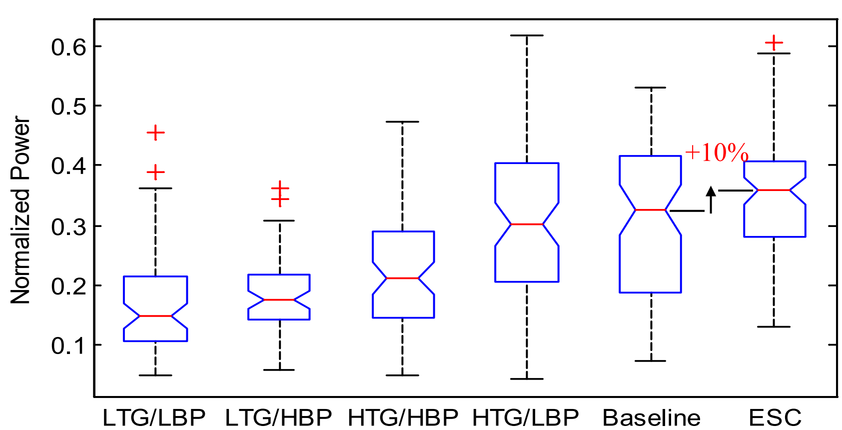

Figure 3.25. P_N box plots of CART3 testing of the two-input ESC and comparative scenarios

Figure 3.26 demonstrates the normalized DEL values of the selected fatigue loads for the six tested cases, with the values of the baseline case normalized to unity. The DEL values of the two-input ESC are all smaller (3%~22%) than those of the baseline case. The normalized results of power performance and load indices are summarized in Table 3.9.

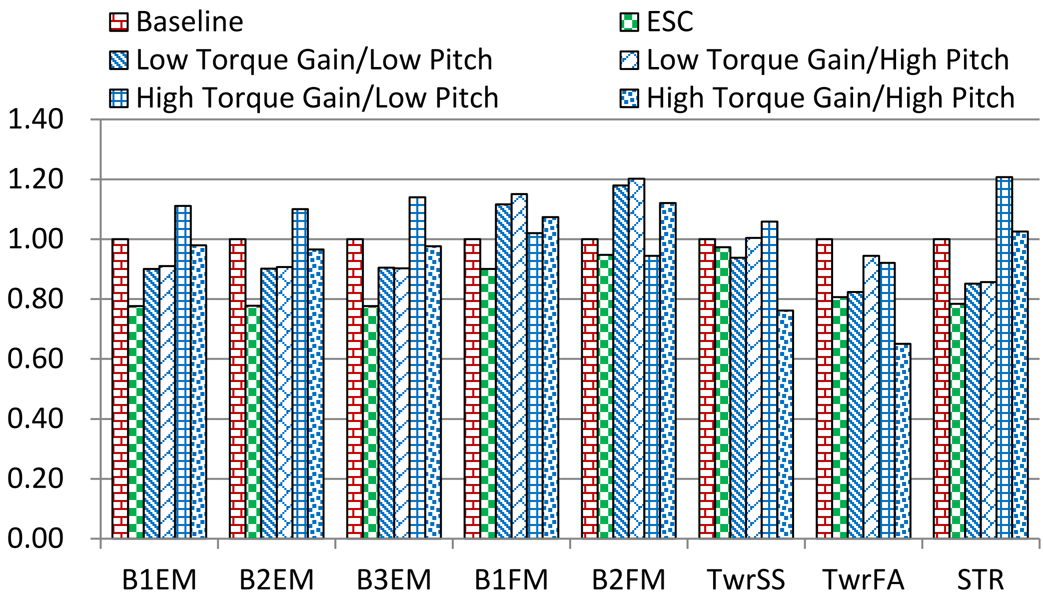

Figure 3.26. Normalized DEL values of selected load variables for CART3 testing of two-input ESC and comparative scenarios

Table 3.9. Energy capture and load indices for CART3 testing of two-input ESC and comparative scenarios

Index	Baseline	Two-input ESC	Low k_t Low β	Low k_t High β	High k_t Low β	High k_t High β
P_N	1	+12%	–45%	–40%	+1%	-28%
B1EM	1	–22%	–10%	–9%	+11%	-2%
B2EM	1	–22%	–10%	–9%	+10%	-3%
B3EM	1	–22%	–10%	–10%	+14%	-2%
B1FM	1	-10%	+12%	+15%	+2%	+7%
B2FM	1	-5%	+18%	+20%	-6%	+12%
TwrSS	1	-3%	–6%	+0.4%	+6%	-24%
TwrFA	1	-19%	–18%	–6%	-8%	-35%
STR	1	–22%	–15%	–14%	+21%	+3%

By aggregating all the test data, the histograms of hub-height wind speed for different scenarios are shown in Figure 3.27.

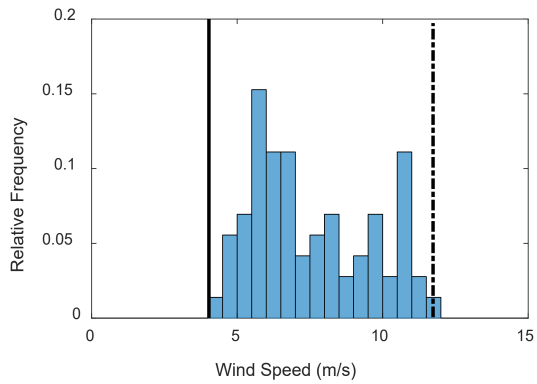

(a). ESC (mean: 7.57 m/s)

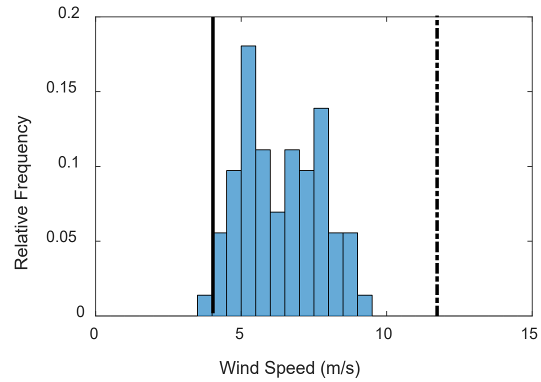

(b). Baseline (mean: 6.35 m/s)

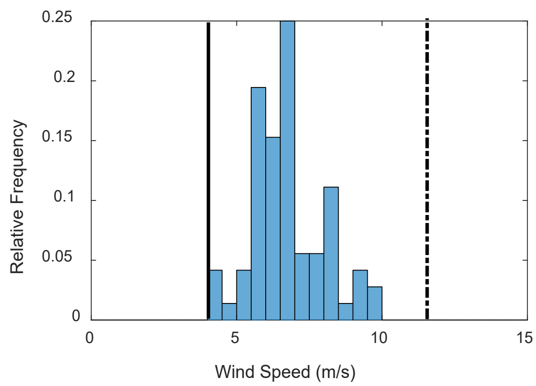

(c). LTG/LBP (mean: 6.76 m/s)

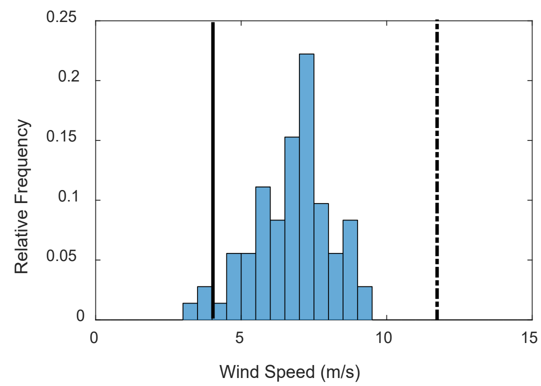

(d). LTG/HBP (mean: 6.79 m/s)

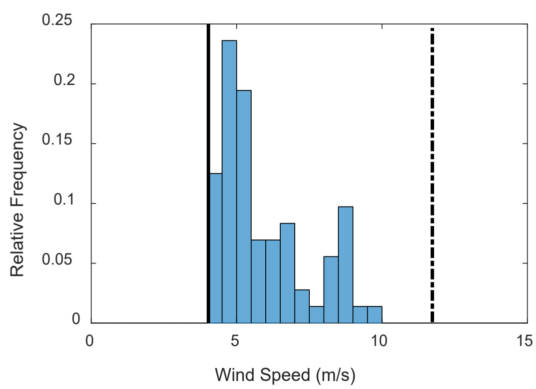

(e). HTG/LBP (mean: 6.06 m/s)

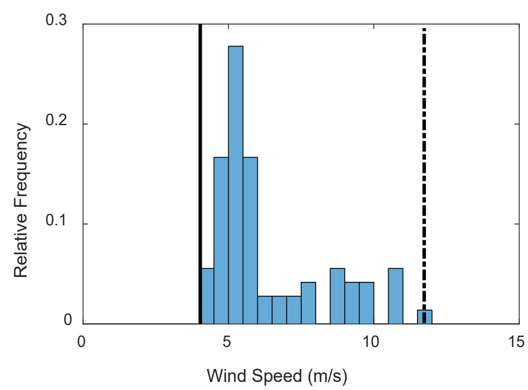

(f). HTG/HBP (mean: 6.37 m/s)

Figure 3.27. Wind speed histograms (based on 7200 seconds of data) for CART3 testing of the two-input ESC and comparative scenarios. Vertical solid lines denote the cut-in speed (4 m/s). Dash-dot line represents the rated speed (11.7 m/s)

The box plots of the wind speed for two-input ESC case and comparative scenarios are shown in Figure 3.28. From this figure, it is obvious that the wind speed is in Region-2 during the field test of two-input ESC and other five comparative scenarios.

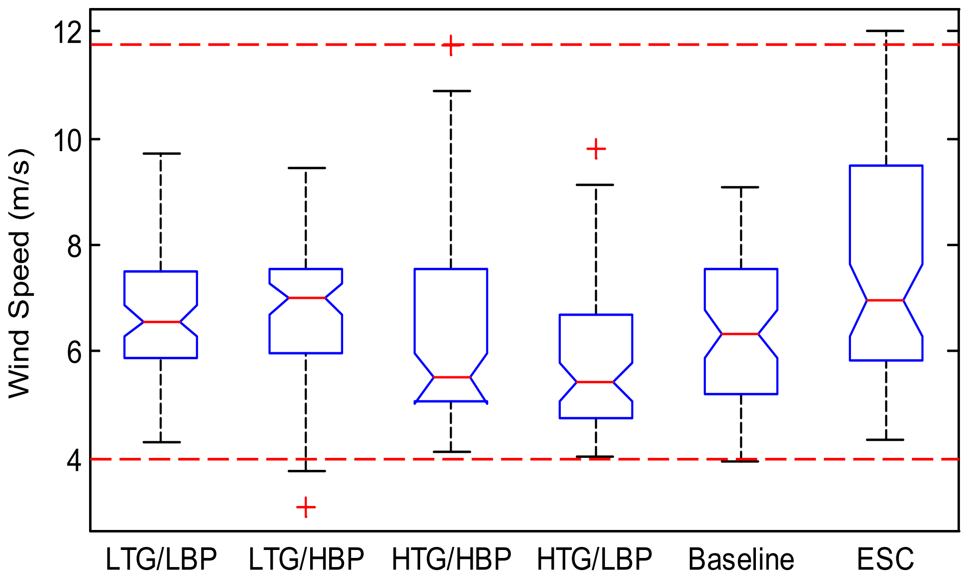

Figure 3.28. Wind speed distribution (box plots) for each two-input controller tested. Dashed red lines indicate rated wind speed and cut-in wind speed

The wind roses for CART3 field test of two-input ESC and other five comparative cases are plotted in Figure 3.29.

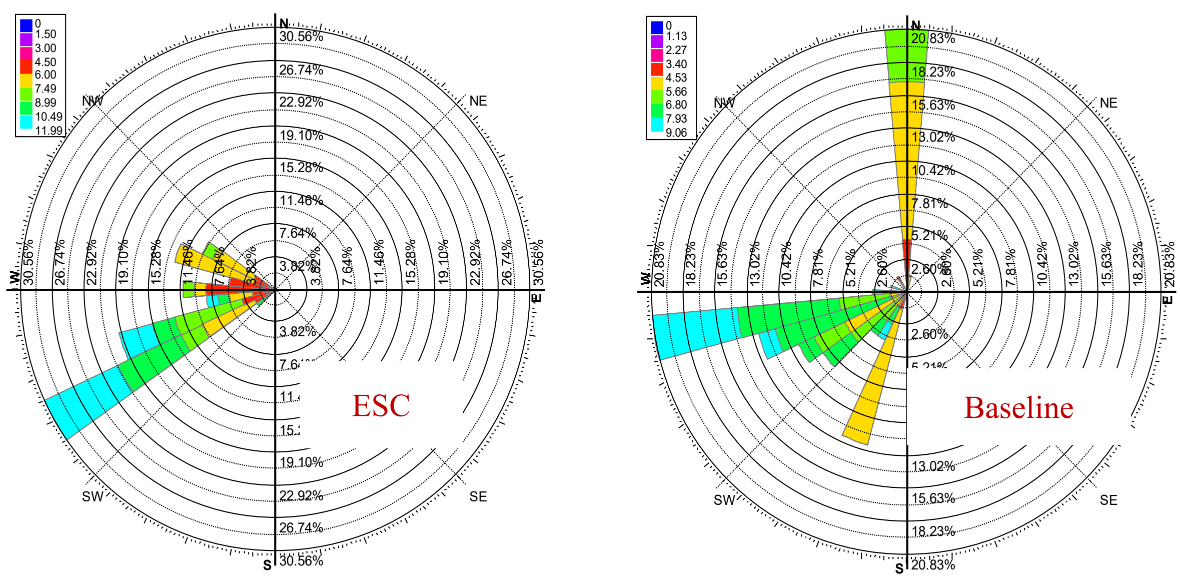

Figure 3.29. Wind roses for the CART3 testing of the two-input ESC and comparative scenarios

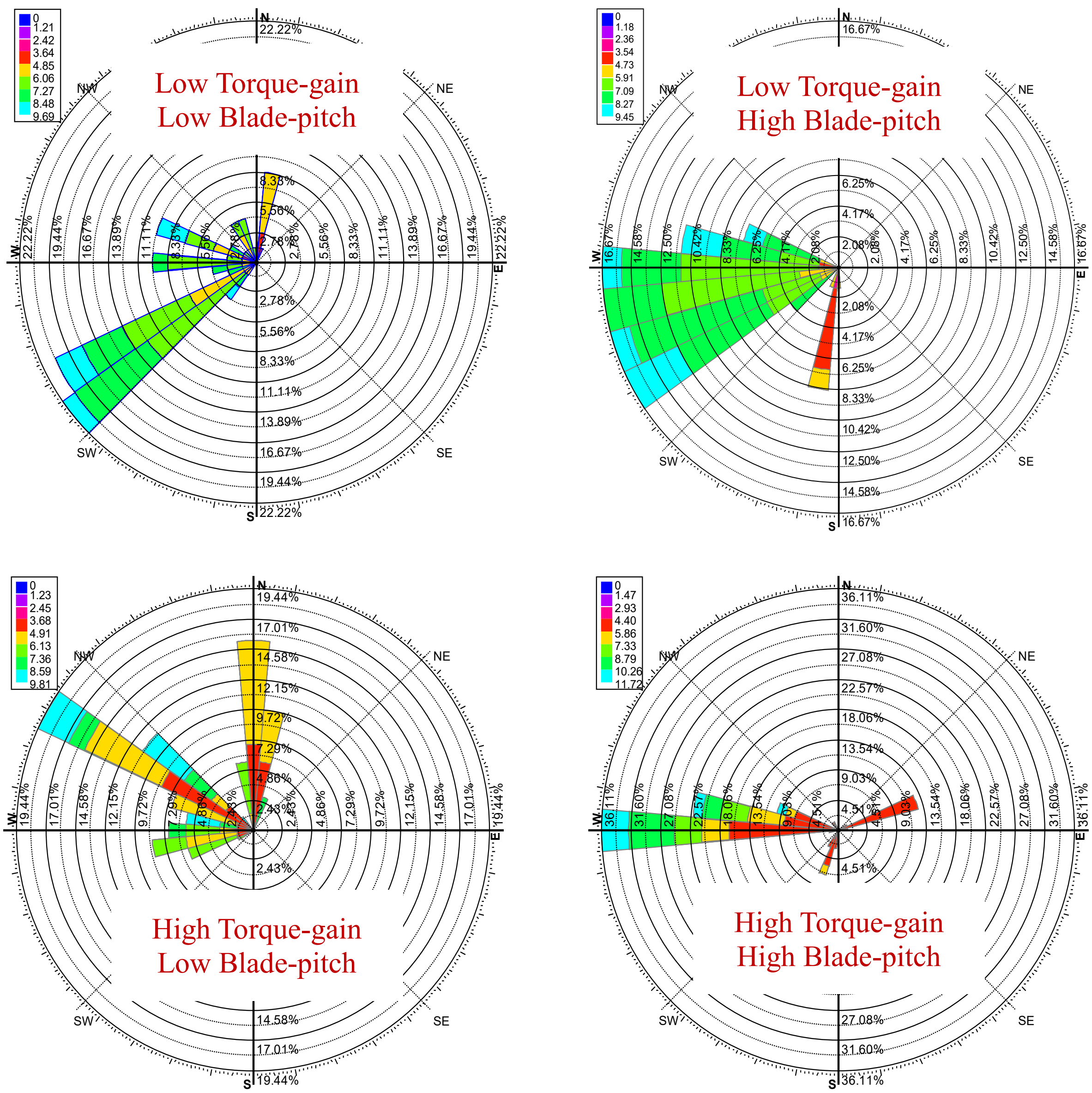

Figure 3.29. (cont.) Wind roses for the CART3 testing of the two-input ESC
and comparative scenarios

3.6 Confidence Interval Analysis

The normalized power shown in Table 3.7 through Table 3.9 indicates that for each type of field test (torque-gain, blade-pitch and two-input), ESC results in higher value of normalized power compared with baseline control. However, due to large variation of the normalized power value, as can be seen from the P_N histogram, the superiority of ESC over baseline is still not very convincing. For better evaluation of the field test result, in this section, a statistical analysis based on confidence interval is provided to assess the statistical significance of the P_N comparison between ESC and baseline.

The confidence interval analysis result is shown in Table 3.10. As can be seen, for torque-gain field test, with 90% confidence interval (Significance level: 0.1), we are 90% confident that the increase of normalized power for ESC over baseline is between the range of 3.9% - 19.2%. For blade-pitch field test, the 90% confidence interval of normalized power increase is between 0.8% to 15.9%. For two-input field test, the 90% confidence interval is in the range of 1.3% - 22.6%.

Table 3.10. Confidence interval analysis for CART3 ESC test

Test Cases	$P_{N,\,ESC} - P_{N,\,Base}$ **80 % Confidence Interval**	$P_{N,\,ESC} - P_{N,\,Base}$ **90 % Confidence Interval**
Torque-gain	[5.6%, 17.5%] × $P_{N,\,Base}$	[3.9%, 19.2%] × $P_{N,\,Base}$
Blade-pitch	[2.5%, 14.2%] × $P_{N,\,Base}$	[0.8%, 15.9%] × $P_{N,\,Base}$
Two-input	[3.7%, 20.3%] × $P_{N,\,Base}$	[1.3%, 22.6%] × $P_{N,\,Base}$

To gain further insights into power increases achieved with the ESCs, the 95% confidence intervals (CI) are computed based on the normalized power. The average value and 95% confidence interval for the extremum seeking controllers and the baseline controllers are shown in . The red dash line shown in the figure is the calibrated optimum $C_{P,max}$ = 0.47 based on the Simulink CART3 FAST model provided by NREL.

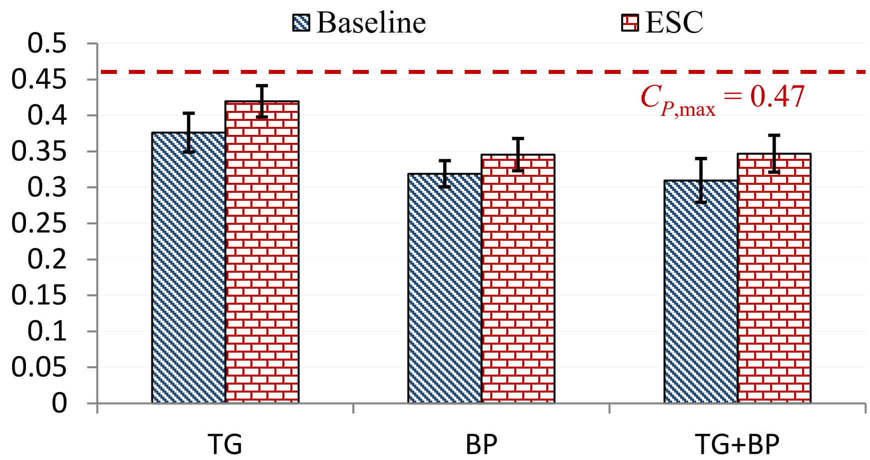

Figure 3.30. Average normalized power (bar graph) and the 95% confidence intervals for the ESC and baseline controller

To assist in the interpretation of the results, note that the experiments were conducted in 2015-2016 as follows:

- Torque-gain field test (TG): June to August
- Blade-pitch field test (BP): October to December
- Two-input field test (TG+BP): December to March

The following conclusions are supported by Figure 3.30:

1. All three ESC controllers achieve higher normalized power than the baseline controller tested during the same time period.
2. The torque-gain case attains the best performance for both ESC and baseline. This is likely due to the fact that this test was done in summer months. The performance for this case is the closest to the theoretical maximum power coefficient.
3. The normalized power is reduced for the BP and TG+BP experiments. This is likely due to the presence of snow and ice fog at the test site, which could decrease blade aerodynamic performance.

3.7 Conclusion and Discussion

This chapter presents the results of testing ESC based Region-2 controllers on the NREL CART3 wind turbine. Control strategies based on torque-gain ESC, blade-pitch ESC and two-input (torque-gain + blade-pitch) ESC were implemented and compared with a baseline controller provided by NREL. The normalized power and DEL of selected fatigue loads have been evaluated.

The ESC controllers have shown improvement in normalized power ranging from 8% for blade-pitch ESC to 12% for torque-gain ESC. The normalized power improvement for the two-input case (torque-gain + blade-pitch) is about the same as that of the torque-gain case, but the loads are reduced with respect to the torque-gain case. The DELs of most load variables under ESC operation are comparable to those of the NREL baseline controller, with some increase in the tower-base fore-aft bending moment for the torque-gain ESC.

The CART3 baseline controller has been in use since 2010 and remains the same for each test done at NREL [87]. From this point of view, our field test results have shown that the ESC is a promising algorithm for improving the energy capture of an existing wind turbine operating in Region-2, without the need of wind turbine model or wind measurements.

CHAPTER 4

MULTI-OBJECTIVE ESC FOR ENERGY CAPTURE ENHANCEMENT WITH LOAD REDUCTION*

4.1 Introduction and Research Motivation

Existing studies on ESC based Region-2 control have been focused on maximizing power without consideration of load impact. Under certain combinations of control actions, wind inputs and turbine characteristics, structural loads may increase. Also, due to undesirable structure design or construction, it is possible to excite structural modes even with the conventional Region-2 operation of blade pitch and/or generator torque control. Such resonance modes may change with site and time since they are influenced by construction and foundation variability, as well as by component degradation, which may not be predictable from the design model. Any increases in damage equivalent load (DEL) may undermine the benefit of the power increase with ESC, thus compromising the levelized cost of energy (LCOE). *Therefore, it is desirable to limit or reduce structural loads while maximizing the wind power generation, without acquisition and/or calibration of a turbine structural model.*

In this chapter, we propose a multi-objective ESC scheme for wind turbine Region-2 operation, based on modifying the objective function of the existing ESC strategies to incorporate a penalty on structural loads. The proposed method is evaluated in two scenarios: 1) a single-input ESC with the torque gain as control input: 2) a two-input ESC with both torque gain and blade pitch as control inputs. Simulations are performed with NREL's CART3 wind turbine Simulink model.

4.2 Multi-objective ESC based Region-2 Control with Load Reduction

The diagram of the proposed multi-objective ESC based Region-2 control algorithm is shown in Figure 4.1.

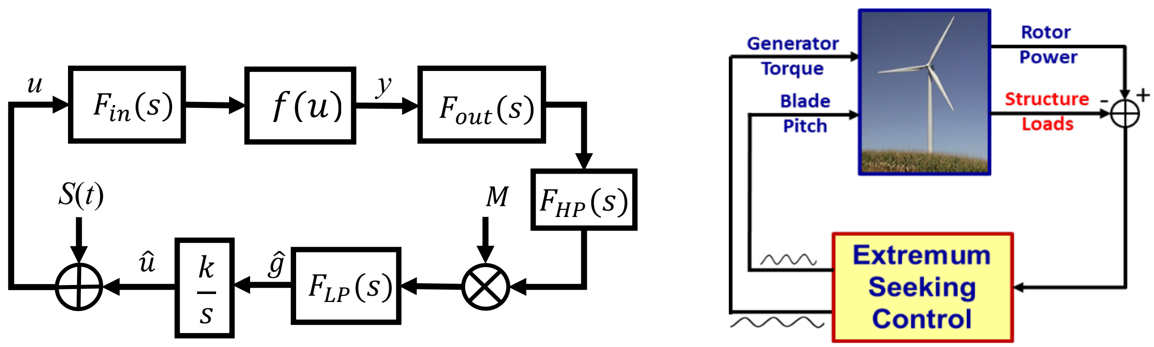

(a). Block diagram of dither ESC (b). Multi-objective ESC with load reduction

Figure 4.1. Proposed multi-objective ESC for maximizing power output with load reduction

As can be seen, to enhance power capture while reducing the fatigue loads, the performance index for the multi-objective ESC is designed as (see Figure 4.1(b)):

$$f(\beta, k_t) = P(\beta, k_t) - \sum_{i=1}^{N} c_i L_i(\beta, k_t) \tag{4-1}$$

where β and k_t denote the blade pitch angle and the torque gain, respectively, P denotes the rotor power of the wind turbine, L_i denotes load indices as functions of blade pitch angle and torque gain, and $c_i > 0$ are weight factors. The negative sign on the right-hand side of Equation (4-1) reflects the goal of minimizing the weighted loads while maximizing power P.

4.3 ESC Design for Region-2 Operation of Wind Turbine with Load Reduction

In this study, two cases are considered for the multi-objective ESC Region-2 control for increasing power production with loads mitigation. The NREL's CART3 wind turbine model is used as the illustrative platform for the simulation studies. The CART3 specifications can be found in [71].

The first case we consider is the control of vibrations due to excitation of a low-frequency tower mode under variable speed operation. For different constant wind speed at the hub height, with 3.7° blade pitch angle (NREL's Region-2 baseline setting), the torque gain dependent profiles of rotor speed Ω_r, rotor power P_r and TBSSBM (tower base side-to-side bending moment) DEL are shown in Figure 4.2(a).

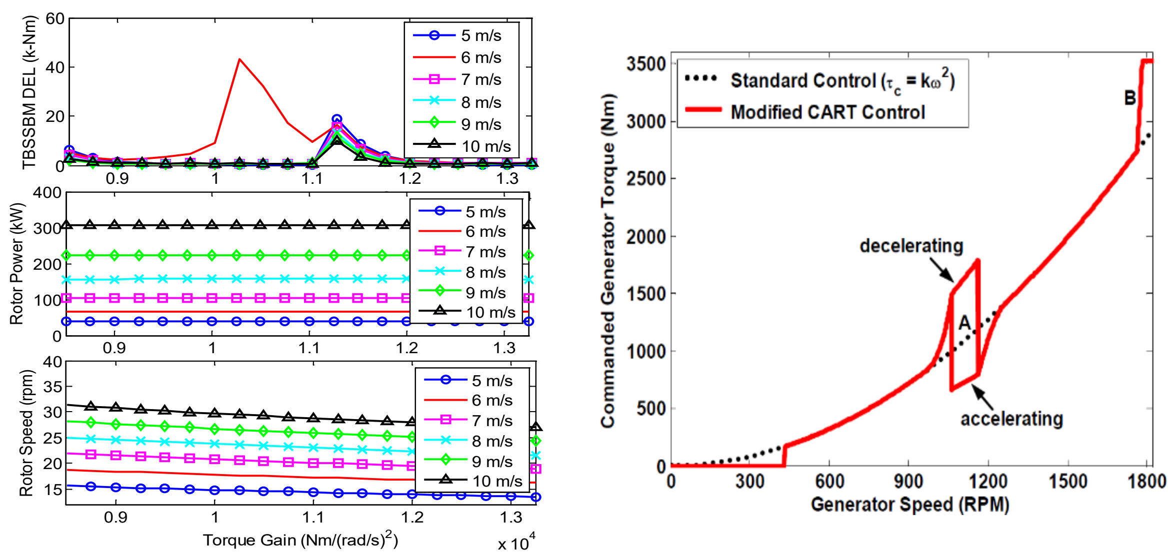

(a). P_r, Ω_r and TBSSBM DEL (various wind speeds) (b). Overriding control for tower resonance [79]

Figure 4.2. CART3 resonance load and NREL's overriding control strategy

Although the peak-power torque gain is around 11,000 N-m/(rad/s)^2, the power map is quite flat for the range of torque gain from 8,500 to 13,250 N-m/(rad/s)^2, i.e. for any given wind speed considered, the rotor power varies by less than 0.8% only. The torque-gain ESC for power maximization only may end up with any torque gain in this range. However, the TBSSBM DEL shows a significantly large peak at the torque gain of 10250 N-m/(rad/s)^2 with 6 m/s wind speed, and some smaller peaks at 11,200 N-m/(rad/s)^2 for other wind speeds. The corresponding rotor speed is around 17.7 rpm, which is associated with the 0.88 Hz structural mode of tower vibration. NREL has implemented a resonance-avoidance operation for CART3 as shown in Figure 4.2(b) [79]. The torque command follows a hysteresis loop around the generator speed corresponding to the 1st TBSSBM mode at 0.88 Hz, i.e. corresponding to the afore-mentioned 17.7 rpm critical rotor speed. This scheme reduces the excitation of this mode by reducing the dwell time around this mode. Such overriding control requires modelling or calibration for a specific wind turbine. For field operation in general, however, such structural modes depend on the actual aerodynamic properties of wind turbine, installation and foundation characteristics. It would be inconvenient to carry out such controller design as the structural modes for each turbine may vary dramatically. Calibration and/or modelling would be tedious and expensive. ESC based model-free control, by including the structural load into the performance index as shown in Equation (4-1), can lead to a simple and effective strategy to achieve an optimal compromise between power capture and load reduction.

The second scenario relates to the potential impact on the blade-root flap-wise bending moment (BRFWBM) under variable-speed variable-pitch operation. The rotor power is at the maximum for torque gain k_t = 11000 N-m/(rad/s)^2 and the pitch angle of 4°. In Figure 4.3, the normalized DEL and standard deviation of BRFWBM are plotted in terms of blade pitch and torque gain, which reveals that the BRFWBM DEL decreases monotonically with the increasing torque gain and decreasing blade pitch angle.

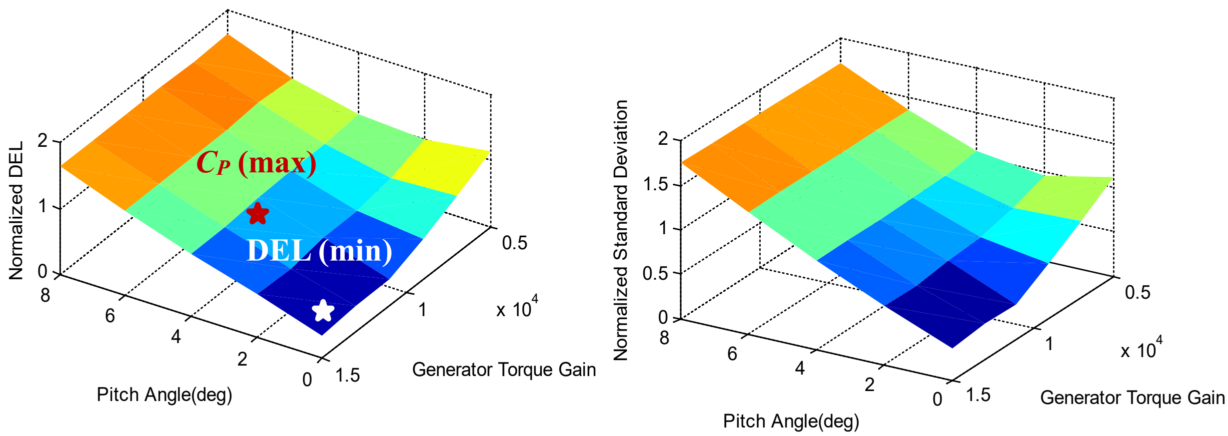

(a). Normalized DEL (b). Normalized standard deviation

Figure 4.3. Profiles of CART3 BRFWBM vs. torque gain and blade pitch (6 m/s constant)

Note that in order to manifest the value of the proposed scheme, the wind speed that result in the worst scenarios of structural vibration is chosen, instead of using a uniform wind speed. For the torque-gain ESC, 6 m/s is found as the wind speed that has the largest tower resonance, although resonance is observed for other wind speed as well. For the two-input ESC, a wind speed of 6.2 m/s would excite the most tower resonance. The difference of the worst-case wind speed is because ESC results in a slightly different blade pitch than the NREL baseline (3.7°). As shown in Equation (4-1), the rotor power feedback for the ESC controller is penalized by the load times the weight factor c. When c is small, the priority of ESC is to maximize the rotor power, and thus ESC settles close to the optimum C_P of the performance map. As c increases, higher priority of ESC will be allocated to load reduction. When c is large enough, ESC will approach the operating point with significant reduction of BRFWBM load as shown in Figure 4.3(a). For real-time optimization, however, the damage equivalent load (DEL) is not a convenient feedback signal due to the complexity of its calculation. Therefore, the standard deviation (SD) is considered as an equivalent quantity for load feedback. As shown in Figure 4.3(b), the SD value of the load demonstrates almost the same trend with pitch angle and torque gain as the DEL profile. Therefore, for the multi-objective ESC, the SD value of the measured load is adopted as the load index.

4.4 Simulation Results

To evaluate the proposed ESC scheme, three cases have been studied using simulations of CART3 operation. The simulations are performed using NREL's FAST (v7) platform[80]. The following cases are considered: (4.4.1) torque-gain ESC with TBSSBM load reduction; (4.4.2) two-input (torque-gain and blade-pitch) ESC with BRFWBM load reduction; (4.4.3) two-input (torque-gain and blade-pitch) ESC with both TBSSBM and BRFWBM loads reduction. For each case, simulations are performed under both constant wind and turbulent wind. The standard deviation (SD) of the load variables is calculated as the performance index of load feedback, obtained with a moving average filter with 6-sec window.

4.4.1 ESC with TBSSBM DEL Reduction

In this case, by tuning the torque gain, the ESC aims to maximize the power production, while avoiding the excitation of the tower structural mode at 0.88Hz. Since the wind turbine rotor speed that excites the tower resonance mode is 17.7 rpm, the proposed method would work properly if the rotor speed does not settle around 17.7 rpm. The rotor speed changes monotonically with the torque gain. Compared to the change of blade pitch angle, the change of torque gain is more responsive in tuning the rotor speed. For these reasons, the torque-gain ESC is used for the TBSSBM load reduction.

Figure 4.4 shows the torque gain and wind turbine rotor speed for both the standard ESC (which does not consider load reduction) and the proposed multi-objective ESC with load reduction. The wind used in this simulation is 6 m/s constant wind. The performance index for the torque-gain ESC is $P - c \cdot TBSSBM$, with c = 0.2. The ESC is engaged at 400 seconds. The 17.7 rpm rotor speed that excites the 0.88 Hz tower-base side-side bending mode is marked as the green solid line in Figure 4.4(b).

For standard ESC without load reduction, the torque gain and the rotor speed are settled at around 11000 N-m/(rad/s)^2 and 17 rpm, respectively. For the multi-objective ESC with load reduction, the rotor speed settles to around 16.6 rpm, which results in significantly smaller TBSSBM DEL. Table 4.1 shows the rotor power and the TBSSBM DEL change attained with the load reduction ESC as a percentage of the metrics for the standard ESC without load reduction. The ESC with TBSSBM load reduction shows 93% reduction of the TBSSBM DEL with respect to the standard ESC (power optimization only), while the rotor power decreases by only about 0.2%. The BRFWBM DEL remains almost the same, while the STR (shaft torsional rate) DEL decreases by 3%; note that these two loads are not included in the ESC performance index.

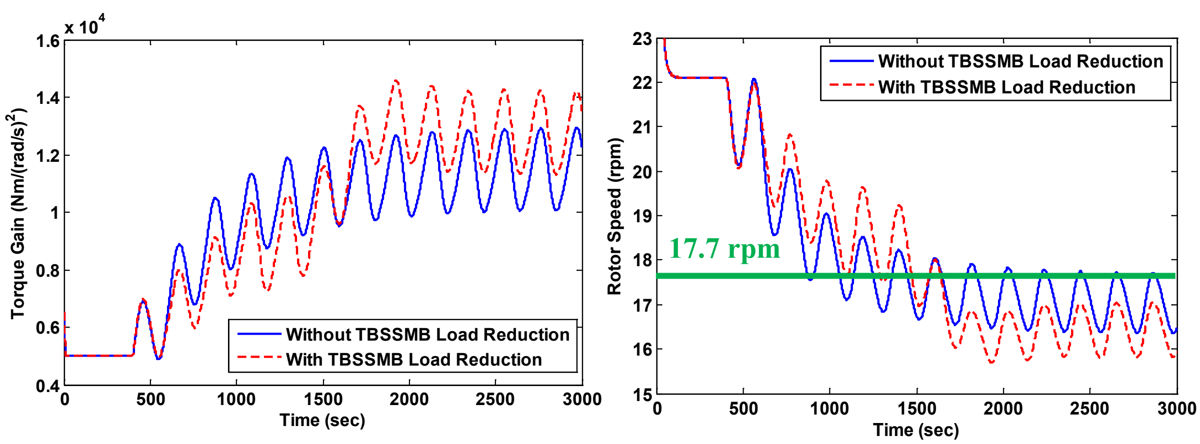

(a). Torque gain (6 m/s constant wind)   (b). Rotor speed (6 m/s constant wind)

Figure 4.4. Simulation results of torque-gain ESC with TBSSBM reduction (6 m/s constant wind)

Simulations with turbulent wind (Mean: 6 m/s, Turbulence Intensity(TI): 10%), with $c = 0.4$ are shown in Figure 4.5. The multi-objective ESC with TBSSMB load reduction steers the rotor speed higher than the 17.7 rpm critical speed that excites the tower structural mode. As shown in Table 4.1, the TBSSMB DEL decreases by 77% compared with the standard ESC, while the rotor power decreases by about 3%. In addition, the DELs for BRFWBM and the Shaft Torsional Rate (STR) are examined. The ESC with TBSSMB load reduction does not effectively reduce these loads, as shown in Table 4.1. The BRFWBM DEL remains almost the same as the standard ESC, while the STR DEL decreases by 70% with turbulent wind.

Table 4.1. Performance of ESC with TBSSBM load reduction relative to the standard ESC

	Included in ESC Performance Index $P - c \cdot TBSSBM$		Not Included in ESC Performance Index	
	Rotor Power	***TBSSBM DEL***	*BRFWBM DEL*	*STR DEL*
Constant Wind	**-0.2%**	**-93%**	-0.4%	-3%
Turbulent Wind	**-3%**	**-77%**	+1%	-70%

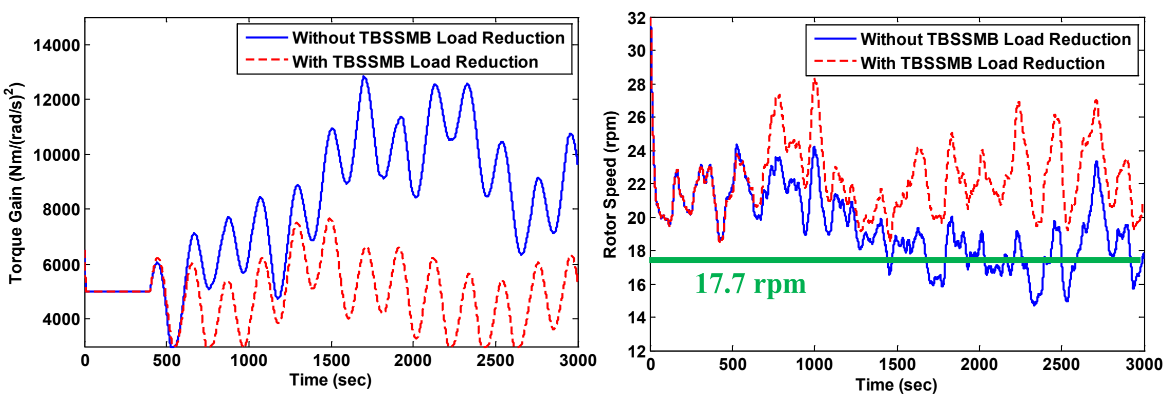

(a). Torque gain (6 m/s turbulent wind)

(b). Rotor speed (6 m/s turbulent wind)

Figure 4.5. Torque-gain ESC with TBSSBM DEL reduction
(Mean: 6 m/s, TI: 10% turbulent wind)

4.4.2 ESC with BRFWBM DEL Reduction

In this test, the objective is to achieve nearly maximum rotor power while reducing the BRFWBM DEL. The static map in Figure 4.3(a) indicates that the BRFWBM DEL decreases with the increase of torque gain and decrease of the blade pitch angle. Thus, a two-input (torque-gain + blade-pitch) ESC is implemented to reduce the BRFWBM load. The ESC performance index is $P - c \cdot BRFWBM$, with c = 0.2. As explained previously, the standard deviation (SD) of the measured loads is adopted as the load index for the ESC controller. The simulation results of ESC with BRFWBM load reduction are shown in Figure 4.6 (with 6.2 m/s constant wind).

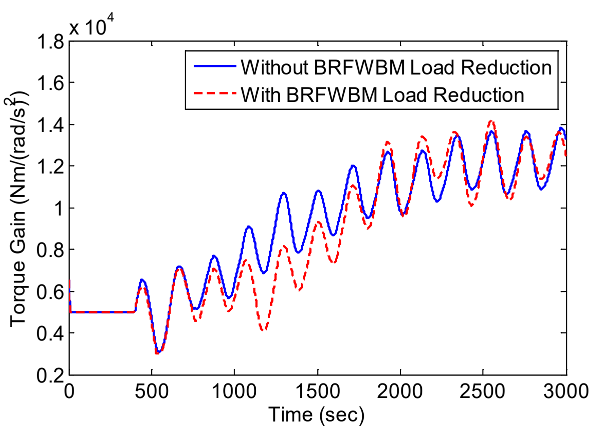

(a). Torque gain (6.2 m/s constant wind)

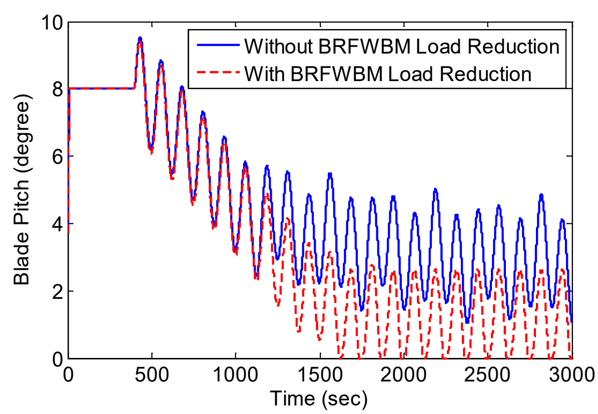

(b). Blade pitch (6.2 m/s constant wind)

Figure 4.6. Two-input ESC with BRFWBM load reduction relative to the standard ESC

The ESC controller is engaged at 400 seconds. The key performance indices of the steady-state simulation results are summarized in Table 4.2. The proposed two-input ESC yields a BRFWBM DEL reduction with smaller blade pitch angle and similar torque gain compared with the ESC with power feedback only. Recall from Figure 4.3 that the BRFWBM decreases with decreasing blade pitch angle and increasing torque gain. When the torque gain exceeds 9000 N-m/(rad/s)^2, the BRFWBM DEL decrease is dominated by the decrease of blade pitch angle. As summarized in

Table 4.2, the BRFWBM DEL decreases by 35%, while energy capture is reduced by 2%. The STR DEL decreases by 2%. Note that the TBSSBM DEL increases by 45% compared to that of the standard ESC. This is not surprising since the ESC in this scenario focused only on the limitation of BRFWBM DEL. The simulation results with turbulent wind (Mean: 6.2 m/s, TI: 10%) are shown in Figure 4.7, with $c = 0.4$. Note from Table 4.2 that the BRFWBM DEL is reduced by 7% and the power extraction remains almost the same as that of the standard ESC. Table 4.2 also shows the STR and TBSSBM DELs, which are not optimized by this controller. The TBSSBM DEL shows an increase (+45%) in constant wind but a decrease (–29%) in the turbulent wind, which is a large inconsistency. The STR DEL is similar to that of the standard ESC.

Table 4.2. Performance of ESC with BRFWBM load reduction relative to the standard ESC

	Included in ESC Performance Index $P - c \cdot BRFWBM$		Not Included in ESC Performance Index	
	Rotor Power	***BRFWBM DEL***	*TBSSBM DEL*	*STR DEL*
Constant Wind	**-2%**	**-35%**	+45%	-2%
Turbulent Wind	**+0.7%**	**-7%**	-29%	-9%

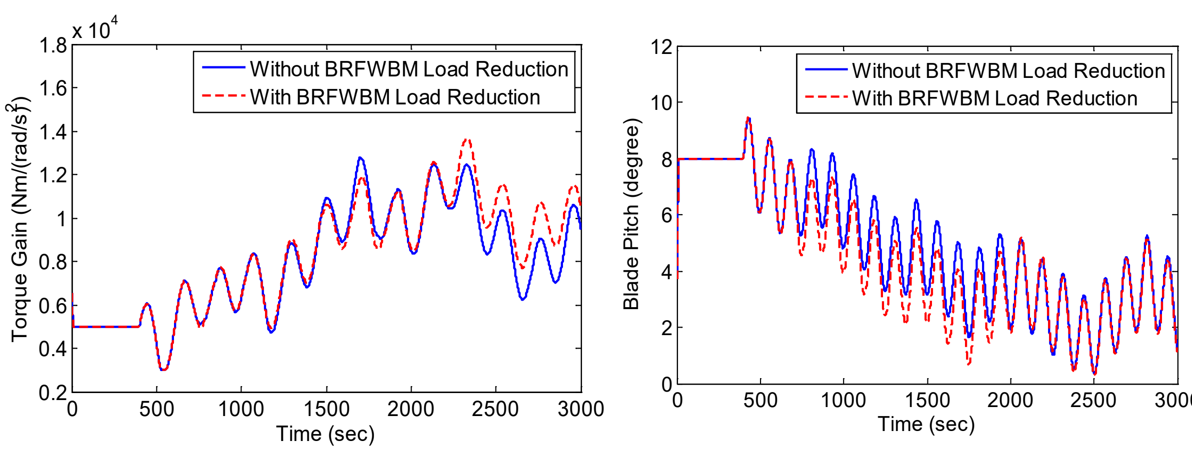

(a). Torque gain (6.2 m/s turbulent wind)

(b). Blade pitch (6.2 m/s turbulent wind)

Figure 4.7. Two-input ESC with BRFWBM reduction (mean: 6.2 m/s, TI:10% turbulent wind)

4.4.3 ESC with TBSSBM and BRFWBM DEL Reduction

As shown in the previous subsection, when only the BRFWBM DEL reduction is considered, the TBSSBM load may have large variation without any consistency. To consistently reduce both the BRFWBM and TBSSBM loads, the TBSSBM and the BRFWBM signals (moving standard deviation) are both included in the ESC performance index. As stated previously, torque-gain control is more suitable for the TBSSBM load reduction. While from Figure 4.3(a), the BRFWBM DEL is more sensitive to the change of blade pitch angle, especially when the torque gain is larger than 9000 N-m/(rad/s)^2. To choose suitable control variable for each load, the correlation coefficients (γ) between the DELs (kN-m) and the control inputs are obtained as shown in Table 4.3. The correlation coefficient between TBSSBM DEL and torque-gain/blade-pitch is 0.8149/-0.0029. The correlation coefficient between BRFWBM DEL and torque-gain/blade-pitch is -0.0631/0.9997. Therefore, the torque-gain ESC is designed by including only the TBSSBM load into the performance index; i.e., the feedback for the torque-gain ESC is $P - c_1 \cdot TBSSBM$, while the blade-pitch ESC is designed by including only the BRFWBM load into the performance index, i.e., the feedback for the blade-pitch ESC controller is $P - c_2 \cdot BRFWBM$.

Table 4.3. Correlation coefficients between loads and inputs

Pitch (°)	**2.8**	**2.9**	**3**	**3.1**	**3.2**	**3.3**	**3.4**	**3.5**	**3.6**	**γ**
BRFWBM DEL	13.55	13.87	14.28	14.67	15.04	15.49	15.83	16.25	16.61	**0.9997**
TBSSBM DEL	14.94	17.86	20.33	16.09	18.68	16.82	15.57	18.46	16.66	**-0.0029**
Torque Gain (Nm/(rad/s)^2)	9500	9600	9700	9800	9900	10000	10100	10200	10300	γ
BRFWBM DEL	17.06	17.10	17.03	17.05	17.05	17.06	17.04	17.07	17.07	**-0.0631**
TBSSBM DEL	3.50	3.76	4.31	5.29	6.83	9.20	17.30	36.64	65.54	**0.8148**

The simulation results with constant wind (6.2 m/s) are shown in Figure 4.8. The weight factors for TBSSBM load and BRFWBM load are $c_1 = 1$ and $c_2 = 0.2$, respectively. Numerical results are summarized in Table 4.4, with the BRFWBM and TBSSBM DEL reduced by 38% and 61%, respectively. The rotor power exhibits about 3% decrease.

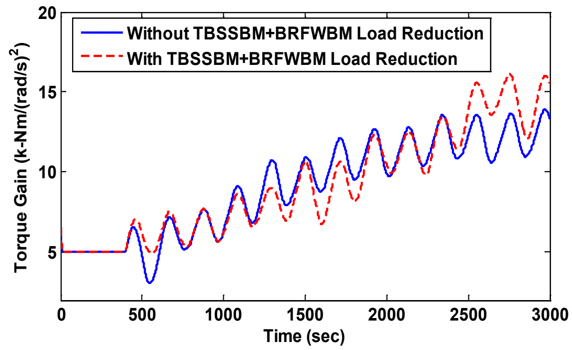

(a). Torque gain (6.2 m/s constant wind)

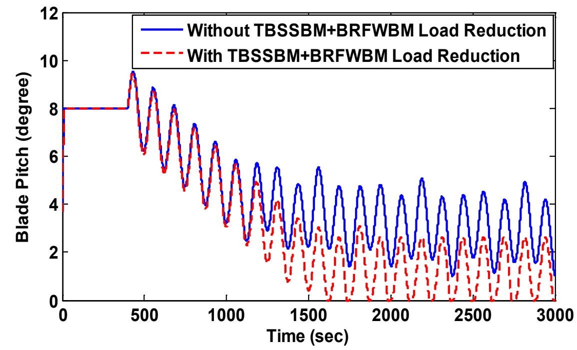

(b). Blade pitch (6.2 m/s constant wind)

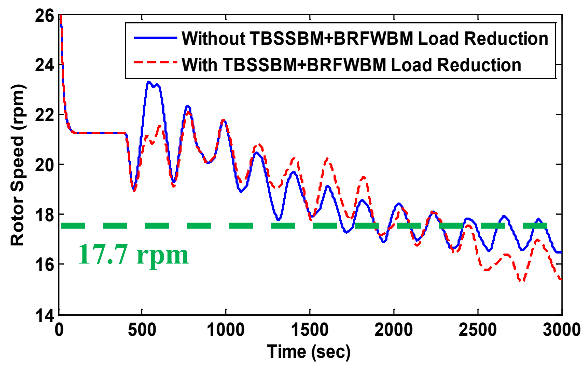

(c). Rotor speed (6.2 m/s constant wind)

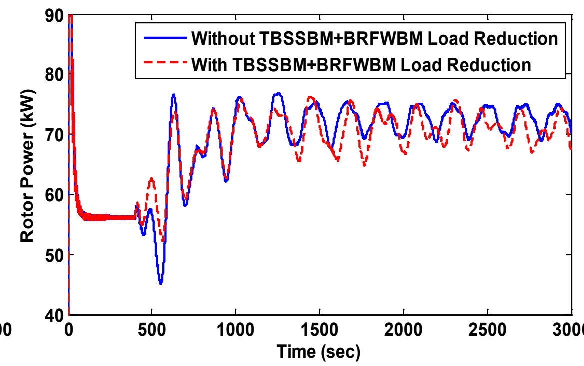

(d). Rotor power (6.2 m/s constant wind)

Figure 4.8. Two-input ESC with TBSSMB+BRFWBM reduction (6.2 m/s constant wind)

This simulation is also performed under turbulent wind (Mean: 6.2 m/s, TI: 10%), with the results shown in Figure 4.9. The weight ratio for TBSSBM and BRFWBM are 0.025 and 1.6, respectively. The performance indices of the simulation results are again summarized in Table 4.4. The TBSSBM and BRFWBM DEL are shown to reduce by 32% and 7%, respectively, with only 1% of decrease in the energy capture.

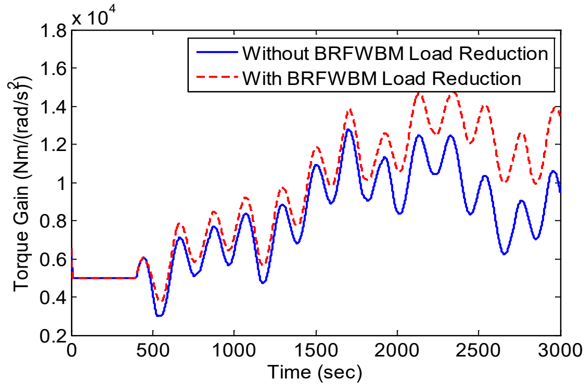

(a). Torque gain (6.2 m/s turbulent wind)

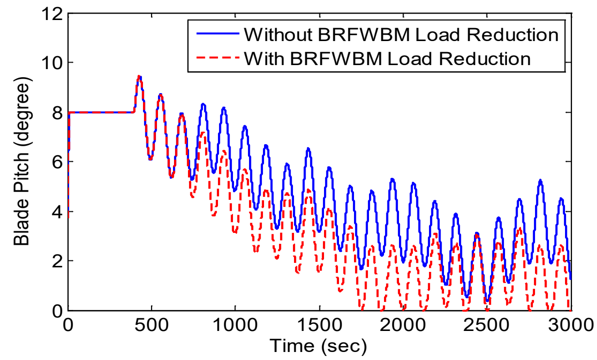

(b). Blade pitch (6.2 m/s turbulent wind)

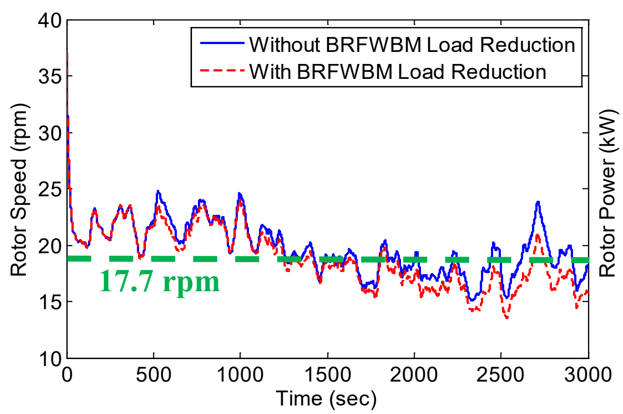

(c). Rotor speed (6.2 m/s turbulent wind)

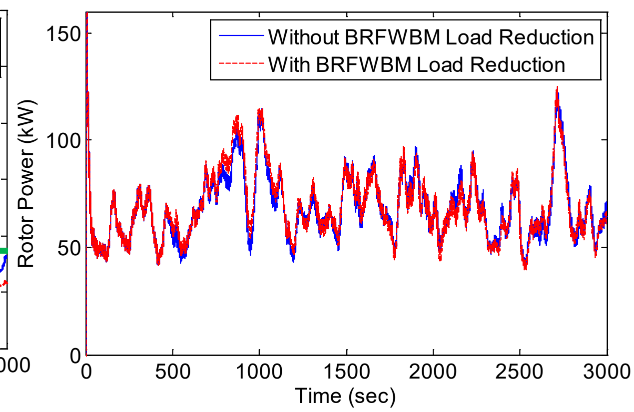

(d). Rotor power (6.2 m/s turbulent wind)

Figure 4.9. Two-input ESC with TBSSBM + BRFWBM reduction
(6.2 m/s, 10% TI turbulent wind)

Table 4.4. Performance of ESC with TBSSBM + BRFWBM load reduction
relative to standard ESC

	Included in ESC Performance Indices*			Not Included in ESC Perf. Index
	Rotor Power	***TBSSBM DEL***	***BRFWBM DEL***	*STR DEL*
Constant Wind	**-3%**	**-61%**	**-38%**	-79%
Turbulent Wind	**-1%**	**-32%**	**-7%**	-12%

*$P - c_1 \cdot TBSSBM$ for torque-gain ESC and $P - c_2 \cdot BRFWBM$ for blade-pitch ESC

4.5 Discussion and Conclusion

This chapter presents a novel Region-2 control scheme with a multi-objective ESC so that nearly optimum power capture is achieved while reducing structural loads. Three illustrative cases are studied: 1) a torque-gain ESC with TBSSBM load reduction, 2) a two-input ESC (torque-gain and blade-pitch) with the BRFWBM load reduction capability, and 3) a two-input ESC (torque-gain and blade-pitch) with reduction of both the TBSSBM and BRFWBM loads. Simulation studies have been performed on the CART3 turbine model under both constant and turbulent wind inputs. For all the cases, the proposed multi-objective ESC reduces the relevant DELs with only slight reduction in the rotor power. Therefore, the effectiveness of the proposed scheme has been demonstrated at least with a limited number of simulations. Future work should be directed at field testing the multi-objective ESC with load control, as has been done in reference [88][49] for the conventional ESC.

The structural modes of field turbines, as demonstrated in CART3 operation, are affected not only by the turbine aerodynamics, but also installation and foundation characteristics, which can often be difficult to determine from a design model. The proposed model-free strategy can be a cost-effective solution of Region-2 control avoiding fatigue loading due to such uncertain structural modes.

CHAPTER 5

DFIG-DC TORQUE RIPPLE MITIGATION BASED ON MULTIPLE REFERENCE FRAME CONTROLLER

In this chapter, a multiple reference frame (MRF) based approach is proposed to mitigate the torque ripple of the DFIG-DC system. The DFIG-DC system uses a diode bridge rectifier between the stator of DFIG and DC link. A reduced-power three-phase PWM converter is connected between the rotor of the DFIG and DC link. Due to the diode commutation, the stator current and stator flux linkage are distorted with harmonics. To reduce the resulting torque ripple, the rotor currents need to track a pulsating reference signal to compensate the distortion of the stator flux. MRF based estimators are used to calculate the main harmonics in both the command value and actual value of the rotor current. Then an MRF based regulator is implemented to achieve an accurate tracking for the harmonics of the rotor current command. Both simulation and experimental results demonstrate the effectiveness of the proposed scheme in reducing the torque ripple. The robustness of the proposed algorithm against deviation of stator frequency is also validated by the simulations and experiments.

5.1 Introduction and Research Motivation

For wind energy system, it is of crucial importance to reduce the levelized cost of energy (LCOE). The DFIG-DC framework studied in this dissertation reduces the cost of the system by eliminating the grid side three-phase PWM converter of the conventional DFIG-AC system. However, the torque ripple caused by the diode commutation needs to be addressed to avoid the increased mechanical stress to the drivetrain structure. Otherwise, the cost saving advantage of the

DFIG-DC system might be offset by the increased maintenance and/or repair cost of the wind turbine.

As discussed in Chapter 2, the existing studies on reduction of torque ripple for DFIG-DC system either lack robustness against stator frequency variation or relies heavily on the accuracy and availability of the model information. In this chapter, a MRF based algorithm is proposed to mitigate the torque ripple in the DFIG-DC system. The proposed MRF controller is composed of two major components. One is the MRF estimator, which decomposes a signal to different reference frames corresponding to different order of harmonics. The other component is the so-called MRF regulator, which is essentially several integral feedback controllers working on different reference frames [81]. Since the reference frame is synchronized with the stator frequency, as a result, MRF based method is very robust against stator frequency deviation. Also, the MRF itself does not rely on too much model information. These advantages justify the motivation of the proposed research.

5.2 Configuration and Modeling of DFIG-DC System

The configuration of the DFIG-DC system is illustrated in Figure 5.1. As can be seen, a three-phase diode bridge rectifier is connected between the stator side of the DFIG and the DC link. The DC side of the rotor side converter is connected to the DC link directly. As a result, the grid side converter found on conventional DFIG-AC system is not used in this framework. The elimination of the grid side converter results in cost savings to the system.

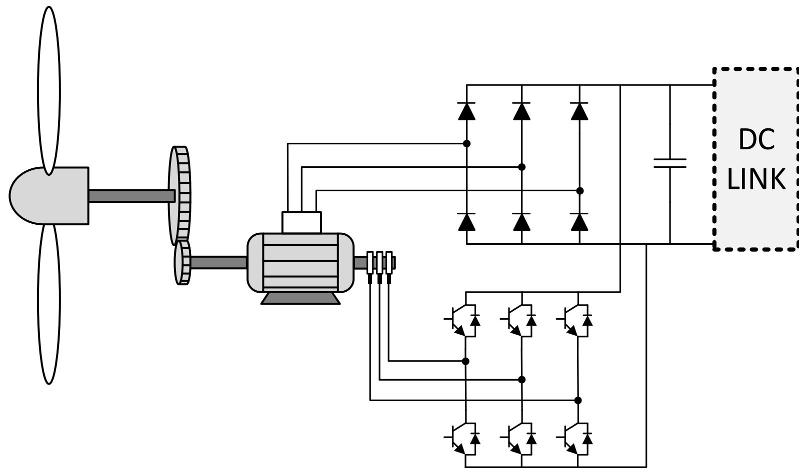

Figure 5.1. Configuration of DFIG-DC system

The per-phase equivalent circuit of the DFIG in synchronous *d-q* reference frame is shown in Figure 5.2. In which all the rotor side quantities are referred to the stator side. R_s and R_r stand for stator and rotor resistances, respectively. L_{ls} and L_{lr} stand for stator and rotor leakage inductances. L_m is the magnetizing (mutual) inductance. R_m represents the core (iron) losses.

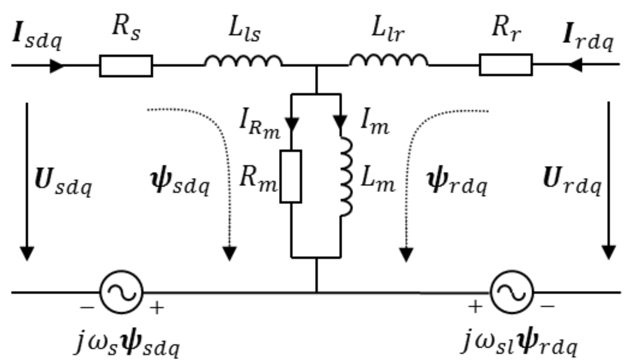

Figure 5.2. Equivalent circuit of DFIG (synchronous d-q reference frame)

Based on the equivalent circuit, the stator and rotor voltage equations can be expressed as

$$\begin{cases} \boldsymbol{U}_{sdq} = \boldsymbol{I}_{sdq}R_s + \dfrac{d\boldsymbol{\psi}_{sdq}}{dt} + j\omega_s\boldsymbol{\psi}_{sdq} \\ \boldsymbol{U}_{rdq} = \boldsymbol{I}_{rdq}R_r + \dfrac{d\boldsymbol{\psi}_{rdq}}{dt} + j\omega_{sl}\boldsymbol{\psi}_{rdq} \end{cases} \tag{5-1}$$

In which, $\omega_{sl} = \omega_s - \omega_r$ is the slip frequency that is defined as the difference between the synchronous stator frequency and DFIG rotor shaft angular speed. In general, the iron loss current I_{R_m} is much smaller than magnetizing current I_m, as a result, the flux linkage equation for the stator and rotor can be approximately formulated as

$$\begin{cases} \boldsymbol{\psi}_{sdq} = L_s \boldsymbol{I}_{sdq} + L_m \boldsymbol{I}_{rdq} \\ \boldsymbol{\psi}_{rdq} = L_r \boldsymbol{I}_{rdq} + L_m \boldsymbol{I}_{sdq} \end{cases} \tag{5-2}$$

Note that $L_s = L_{ls} + L_m$, $L_r = L_{lr} + L_m$. The electromagnetic torque can be calculated as

$$T_e = -\frac{3}{2} p \,\mathrm{Im}\{\boldsymbol{\psi}_{sdq} \hat{\boldsymbol{I}}_{sdq}\} \tag{5-3}$$

In which, p represents the pole pair number, $\hat{\boldsymbol{I}}_{sdq}$ is the conjugate vector of $\boldsymbol{I}_{sdq}$.

5.3 Analysis of Torque Ripple in DFIG-DC System

In this proposed research, it is assumed that the DC link voltage is approximately constant. And, the diode bridge rectifier is assumed to be working in continuous commutation mode (CCM). As explained in [82], the stator voltage of DFIG will be clamped to a three-step square wave as shown in Figure 5.3. Note that V_{DC} shown in the figure represents the DC link voltage.

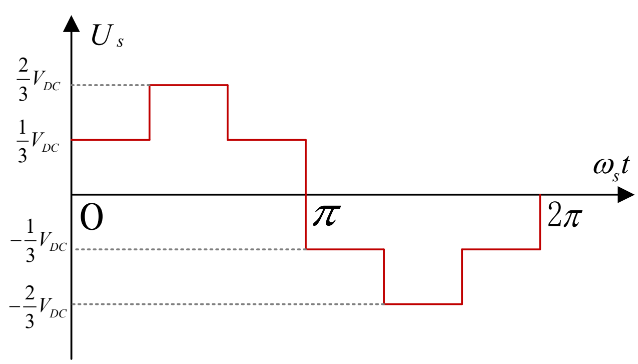

Figure 5.3. Stator voltage of the DFIG-DC system

Based on Fourier's theorem, the periodic waveform shown in Figure 5.3 can be written as the sum of the fundamental and a series of harmonic voltages. Assuming the voltage waveform shown is for phase A, then we have

$$U_{sa} = \frac{2V_{DC}}{\pi}\left\{\sin(\omega t) + \sum_{n=1}^{\infty}\frac{1}{6n\pm 1}\sin[(6n\pm 1)\omega t]\right\} \tag{5-4}$$

Similarly, the stator voltage for B and C phases are expressed by Equation (5-5) and (5-6) respectively.

$$U_{sb} = \frac{2V_{DC}}{\pi}\left\{\sin(\omega t - \frac{2}{3}\pi) + \sum_{n=1}^{\infty}\frac{1}{6n\pm 1}\sin[(6n\pm 1)(\omega t - \frac{2}{3}\pi)]\right\} \tag{5-5}$$

$$U_{sc} = \frac{2V_{DC}}{\pi}\left\{\sin(\omega t + \frac{2}{3}\pi) + \sum_{n=1}^{\infty}\frac{1}{6n\pm 1}\sin[(6n\pm 1)(\omega t + \frac{2}{3}\pi)]\right\} \tag{5-6}$$

From the Equation (5-4) through (5-6), the following three conclusions can be made:

1. Only the non-triplen odd harmonics (i.e. 5^{th}, 7^{th}, 11^{th}, 13^{th}, etc.) exist in the stator voltage.
2. All the $(6n-1)^{th}$ order harmonics are rotating in the reverse direction (negative sequence), while all the $(6n+1)^{th}$ order harmonics are rotating in the forward direction (positive sequence).
3. The amplitude of the harmonics decreases with the increase of order number.

In this study, only the low order harmonics (5^{th} and 7^{th}) are considered due to their dominating amplitude over higher order harmonics. Therefore, the stator voltage in the synchronous *d-q* reference frame can be approximately represented as

$$\boldsymbol{U}_{sdq} = \boldsymbol{U}_{sdq}^{(1)} + \boldsymbol{U}_{sdq}^{(5)}e^{-j6\omega_s t} + \boldsymbol{U}_{sdq}^{(7)}e^{j6\omega_s t} \tag{5-7}$$

Notice that the negative sequence 5th order harmonic is rotating at the speed of $-6\omega_s$ with reference to the synchronous reference frame. While the positive 7th order harmonic is rotating at the speed of $+6\omega_s$. The stator resistance R_s is typically very small and can be ignored. From the stator voltage shown in Equation (5-1) and (5-7), the stator flux linkage equation can be derived as

$$\boldsymbol{\psi}_{sdq} = \frac{\boldsymbol{U}_{sdq}^{(1)}}{j\omega_s} - \frac{\boldsymbol{U}_{sdq}^{(5)}}{j5\omega_s} e^{-j6\omega_s t} + \frac{\boldsymbol{U}_{sdq}^{(7)}}{j7\omega_s} e^{j6\omega_s t} \tag{5-8}$$

As explained in [62], it is assumed that the rotor side of DFIG is regulated with sinusoidal voltage. Also, the rotor resistance R_r is typically very small and can be neglected. Then, the stator current can be calculated as

$$\boldsymbol{I}_{sdq} = \boldsymbol{I}_{sdq}^{(1)} + \boldsymbol{I}_{sdq}^{(5)} e^{-j6\omega_s t} + \boldsymbol{I}_{sdq}^{(7)} e^{j6\omega_s t} = \boldsymbol{I}_{sdq}^{(1)} - \left(\frac{\boldsymbol{U}_{sdq}^{(5)}}{j5\omega_s \sigma L_s} e^{-j6\omega_s t} - \frac{\boldsymbol{U}_{sdq}^{(7)}}{j7\omega_s \sigma L_s} e^{j6\omega_s t}\right) \tag{5-9}$$

where $\sigma = 1 - L_m^2 / (L_s L_r)$ is defined as the leakage factor. By substituting Equation (5-8) and Equation (5-9) into Equation (5-3), the electromagnetic torque of the DFIG can be expressed as

$$T_e = T_e^{(1)} + T_e^{(6)} + T_e^{(12)} \tag{5-10}$$

In which, $T_e^{(1)}$, $T_e^{(6)}$ and $T_e^{(12)}$ represents the fundamental, 6th order and 12th order harmonic component in the electromagnetic torque, and they can be calculated as

$$T_e^{(1)} = \frac{3}{2}\frac{p}{\omega_s} \mathrm{Re}\left\{ \boldsymbol{U}_{sdq}^{(1)} \hat{\boldsymbol{I}}_{sdq}^{(1)} - \frac{\boldsymbol{U}_{sdq}^{(5)} \hat{\boldsymbol{I}}_{sdq}^{(5)}}{5} + \frac{\boldsymbol{U}_{sdq}^{(7)} \hat{\boldsymbol{I}}_{sdq}^{(7)}}{7} \right\} \tag{5-11}$$

$$T_e^{(6)} = \frac{3}{2}\frac{p}{\omega_s} \mathrm{Re}\left\{ [\boldsymbol{U}_{sdq}^{(1)} \hat{\boldsymbol{I}}_{sdq}^{(7)} - \frac{\boldsymbol{U}_{sdq}^{(5)} \hat{\boldsymbol{I}}_{sdq}^{(1)}}{5}] e^{-j6\omega_s t} + [\boldsymbol{U}_{sdq}^{(1)} \hat{\boldsymbol{I}}_{sdq}^{(5)} + \frac{\boldsymbol{U}_{sdq}^{(7)} \hat{\boldsymbol{I}}_{sdq}^{(1)}}{7}] e^{j6\omega_s t} \right\} \tag{5-12}$$

$$T_e^{(12)} = \frac{3}{2}\frac{p}{\omega_s}\mathrm{Re}\left\{-\frac{\boldsymbol{U}_{sdq}^{(5)}\hat{\boldsymbol{I}}_{sdq}^{(7)}}{5}e^{-j12\omega_s t} + \frac{\boldsymbol{U}_{sdq}^{(7)}\hat{\boldsymbol{I}}_{sdq}^{(5)}}{7}e^{j12\omega_s t}\right\} \tag{5-13}$$

From Equation (5-4) through (5-6), it can be derived that

$$\left\|\boldsymbol{U}_{sdq}^{(1)}\right\| = 5\left\|\boldsymbol{U}_{sdq}^{(5)}\right\| = 7\left\|\boldsymbol{U}_{sdq}^{(7)}\right\| \tag{5-14}$$

As a result, Equation (5-11), (5-12) and (5-13) can be further expressed as

$$T_e^{(1)} = \frac{3}{2}\frac{p}{\omega_s}\mathrm{Re}\left\{\boldsymbol{U}_{sdq}^{(1)}[\hat{\boldsymbol{I}}_{sdq}^{(1)} - \frac{\hat{\boldsymbol{I}}_{sdq}^{(5)}}{25} + \frac{\hat{\boldsymbol{I}}_{sdq}^{(7)}}{49}]\right\} \tag{5-15}$$

$$T_e^{(6)} = \frac{3}{2}\frac{p}{\omega_s}\mathrm{Re}\left\{\boldsymbol{U}_{sdq}^{(1)}[(\hat{\boldsymbol{I}}_{sdq}^{(7)} - \frac{\hat{\boldsymbol{I}}_{sdq}^{(1)}}{25})e^{-j6\omega_s t} + (\hat{\boldsymbol{I}}_{sdq}^{(5)} + \frac{\hat{\boldsymbol{I}}_{sdq}^{(1)}}{49})e^{j6\omega_s t}]\right\} \tag{5-16}$$

$$T_e^{(12)} = \frac{3}{2}\frac{p}{\omega_s}\mathrm{Re}\left\{\boldsymbol{U}_{sdq}^{(1)}[-\frac{\hat{\boldsymbol{I}}_{sdq}^{(7)}}{25}e^{-j12\omega_s t} + \frac{\hat{\boldsymbol{I}}_{sdq}^{(5)}}{49}e^{j12\omega_s t}]\right\} \tag{5-17}$$

Comparing Equation (5-16) with Equation (5-17), it can be observed that the magnitude of the 12th order torque harmonic term is much smaller than that of the 6th order harmonic component. Therefore, in this study, the main focus is on reducing the 6th order torque harmonic since higher order harmonics have negligible magnitude.

5.4 Torque Ripple Reduction Strategy Based on Multiple Reference Frame Control

As analyzed in the previous section, if the rotor voltage is regulated as pure sinusoidal waveform by the rotor side converter, then considerable harmonics in the electromagnetic torque will be generated. To reduce the most significant torque harmonic component (6th order), according to Equation (5-16), the stator current needs to be injected with appropriate harmonics to compensate for the stator voltage distortion caused by diode commutation.

To implement the torque ripple reduction scheme, however, it is complex and not straight forward to design a control logic based on Equation (5-16). Note that from Equation (5-2) and (5-3), the electromagnetic torque of the DFIG can also be calculated as

$$T_e = \frac{3}{2} p \frac{L_m}{L_s} \mathrm{Im}\left\{ \boldsymbol{\psi}_{sdq} \hat{\boldsymbol{I}}_{rdq} \right\} = -\frac{3}{2} p \frac{L_m}{L_s} (\psi_{sd} i_{rq} - \psi_{sq} i_{rd}) \tag{5-18}$$

In this study, stator flux field-oriented control (FOC) scheme is adopted. As a result, we have

$$\begin{cases} \psi_{sd} \approx \psi_s \\ \psi_{sq} \approx 0 \end{cases} \tag{5-19}$$

Then, the electromagnetic torque equation can be further expressed as

$$T_e = -\frac{3}{2} p \frac{L_m}{L_s} \psi_{sd} i_{rq} \tag{5-20}$$

For a given torque command T_e^*, the corresponding q-axis rotor current command is given by

$$i_{rq}^* = \frac{T_e^*}{-\frac{3}{2} p \frac{L_m}{L_s} \psi_{sd}} \tag{5-21}$$

If the actual q-axis rotor current i_{rq} can accurately track the command value given by Equation (5-21), then the torque ripple would be very small. However, as analyzed in the previous section, the stator flux linkage is distorted with harmonics. As shown in Equation (5-8), the most significant components are the -5th and +7th order harmonic, which will cause the stator flux linkage to pulsate at a frequency of $6\omega_s$. As a result, the corresponding q-axis rotor current command i_{rq}^* will also contain significant oscillating component at six times of the stator frequency. As explained in [9] and [62], for stability requirement, the bandwidth of the PI current control loop cannot be too high.

Therefore, the PI based current controller is not capable of tracking the fast-changing q-axis rotor current command that oscillates at the frequency of $6\omega_s$.

To deal with the tracking speed limitation of PI current control loop, in this study, a multiple reference frame (MRF) based algorithm is proposed to ensure good tracking performance for the harmonic components in the q-axis rotor current command i_{rq}^*. The so-called multiple reference frame concept was first introduced in [84]. For the past decades, MRF was mainly used as an off-line analysis tool for the unbalanced or non-sinusoidal operation of electric machine or AC grid. The major limitation which prevents the MRF from being used as a real-time controller is that the multiple reference frame transformations requires a lot of computational power. Thanks to the fast development of semiconductor technology, the micro-controllers nowadays are much cheaper and powerful enough to handle the intensive computation of multiple reference frame transformation.

Based on [81], a complete MRF control loop is mainly consist of a MRF estimator and a MRF regulator. The MRF estimator is used to convert the oscillating harmonic component from stationary reference frame to a relatively constant value in the corresponding rotational reference frame. The MRF regulator is then used to ensure each harmonic command value be precisely tracked. The MRF regulator is essentially a combination of PI based controllers which work in parallel under different rotating reference frame. Since each harmonic component is transformed to a slowly-varying value in the corresponding rotational reference frame, a slow PI controller, or even an integrator in the MRF regulator could deliver good tracking performance for the corresponding harmonic command value.

The overall control diagram is shown in Figure 5.4. As explained in [9], the feed-forward term $\omega_{sl}\sigma L_r I_{rq}$ and $\omega_{sl}\sigma L_r I_{rd}$ are used to compensate the cross-coupling between d and q axis. σ is the leakage factor which is defined as

$$\sigma = \frac{L_s L_r - L_m^2}{L_s L_r} \tag{5-22}$$

The proposed MRF based torque ripple mitigation controller is shown in the red dashed box. As can be seen, the output of the MRF controller U_{rq_MRF} is added to the q-axis rotor voltage command directly without passing through the q-axis rotor current PI controller. A stator flux estimator similar to the one used in [58] is adopted to estimate the stator flux linkage, as well as stator flux angle and slip angle. The diagram of the stator flux estimator for stator flux angle estimation is shown in Figure 5.5.

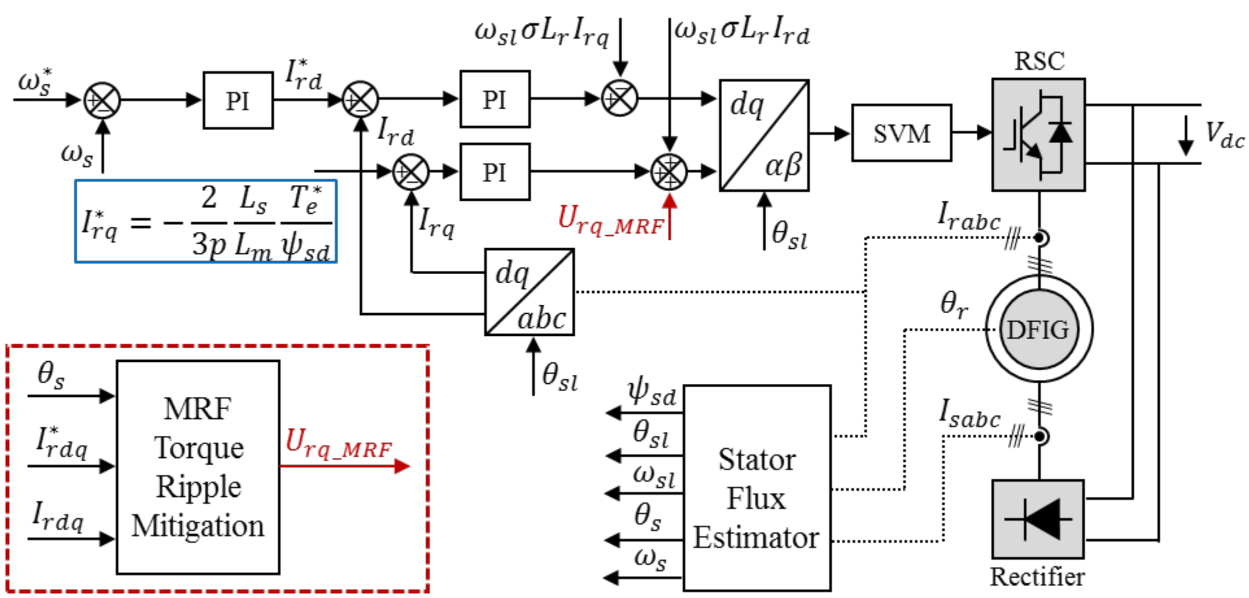

Figure 5.4. Control diagram of MRF based torque ripple mitigation control (simulation test)

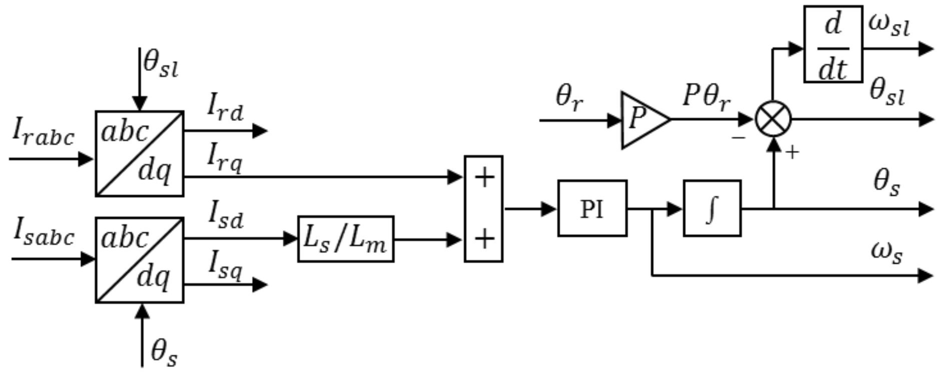

Figure 5.5. Stator flux angle estimator

As introduced previously, the MRF controller is consist of two major parts: a MRF estimator and a MRF regulator. In this application, two MRF estimators are used. One is used on the rotor current command I_{rdq}^{*} to extract the harmonic component, as shown in Figure 5.6. The other MRF estimator is used on the actual rotor current I_{rdq}, as shown in Figure 5.7. Both of these two MRF estimators have the same structure. Note that for this application, only the -5th harmonic and the +7th harmonic are considered since higher harmonic components have negligible magnitude.

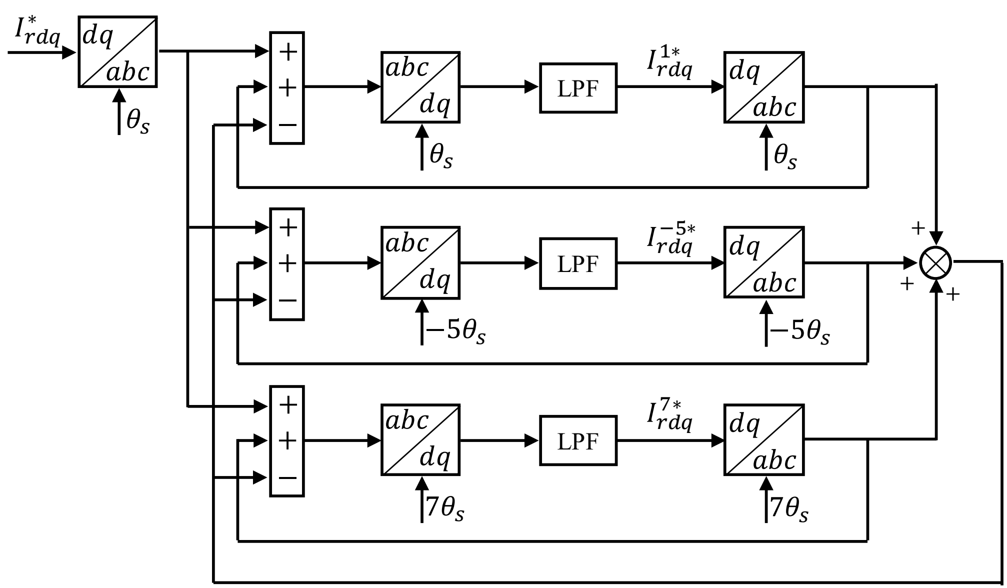

Figure 5.6. MRF based estimator for rotor current command

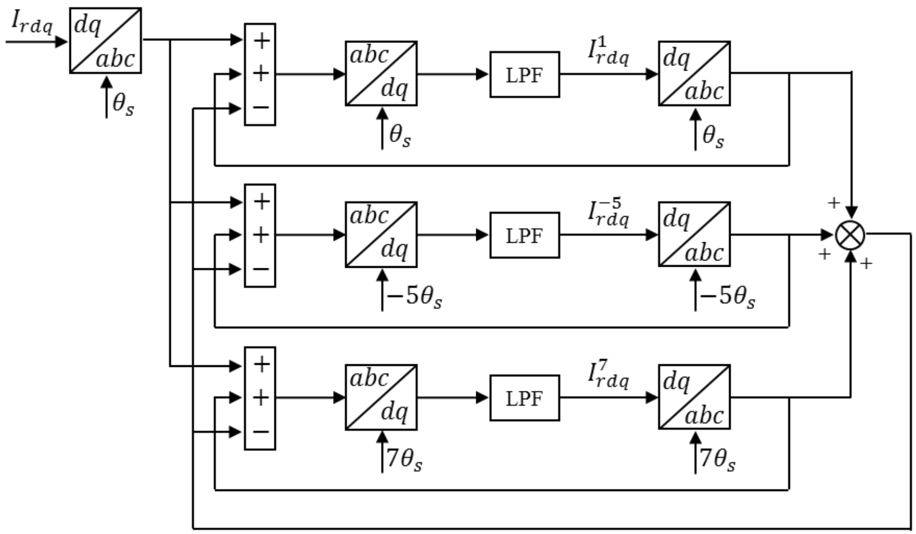

Figure 5.7. MRF based estimator for actual rotor current

After the harmonic components in both the rotor current command and the actual rotor current are extracted by the MRF estimators, these values are sent to a MRF regulator as shown in Figure 5.8. Based on Equation (5-20), the electromagnetic torque mainly depends on q-axis rotor current i_{rq}. Therefore, in this study, The MRF regulator is only dedicated to ensuring the tracking performance of the q-axis rotor current. Since the rotor current reference in its corresponding reference frame is a slow changing signal, a slow PI controller or even a simple integrator could ensure the tracking performance. The output of each PI controller in the MRF regulator is then transformed back to the stator flux synchronous reference frame, and then added together to form the constructed signal U_{rq_MRF} that is to be injected into the q-axis voltage command signal.

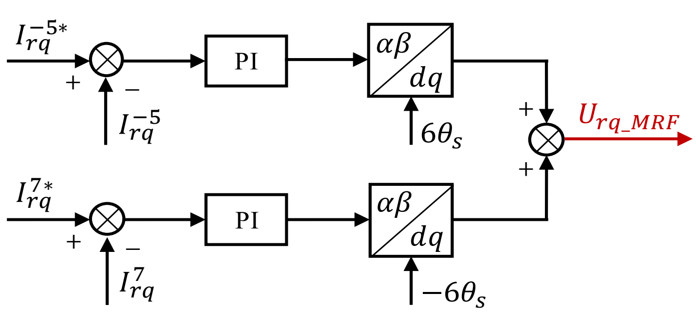

Figure 5.8. MRF based regulator for q-axis rotor current

5.5 Simulation Results

For the simulation study, a model of the experimentally available DFIG-DC system is built in Simulink environment to evaluate the performance of the proposed scheme. The parameters of the DFIG are summarized in the table in Appendix A. The control scheme implemented is shown in Figure 5.4. Two different tests were performed on the simulation platform. The first test is focused on the comparison between the performance with and without MRF controller. During the second test, the stator frequency is constantly varying. The objective of the second test is to demonstrate the robustness of the proposed scheme against stator frequency variation. For both tests, generator rotor speed is set as 900 rpm and generator torque command is set as -50 Nm (generator mode).

5.5.1 Simulation Comparison: MRF Controller ON vs. OFF

In this test, the MRF controller is engaged before 0.1 second. After 0.1 second, the MRF controller is turned off and the output of the MRF controller U_{rq_MRF} is set as zero. The simulation results are shown in Figure 5.9. The stator flux linkage field-oriented control (FOC) is adopted in this study. In this framework, the direction of the stator flux linkage φ_s is defined as the d-axis. As a result, the q-axis stator flux is approximately zero. As can be seen from Figure 5.9(a).

In this simulation test, the stator frequency command is set as 50 Hz. The actual stator frequency curve is shown in Figure 5.9(b). Assuming the voltage of the DC link is relatively constant, then, according to [64], the product of the stator flux linkage and the stator frequency is approximately constant. Since the stator flux linkage is distorted with harmonics as analyzed previously, the stator frequency will also be distorted. This explains why the actual stator frequency is oscillating around the commanded value as shown in Figure 5.9(b).

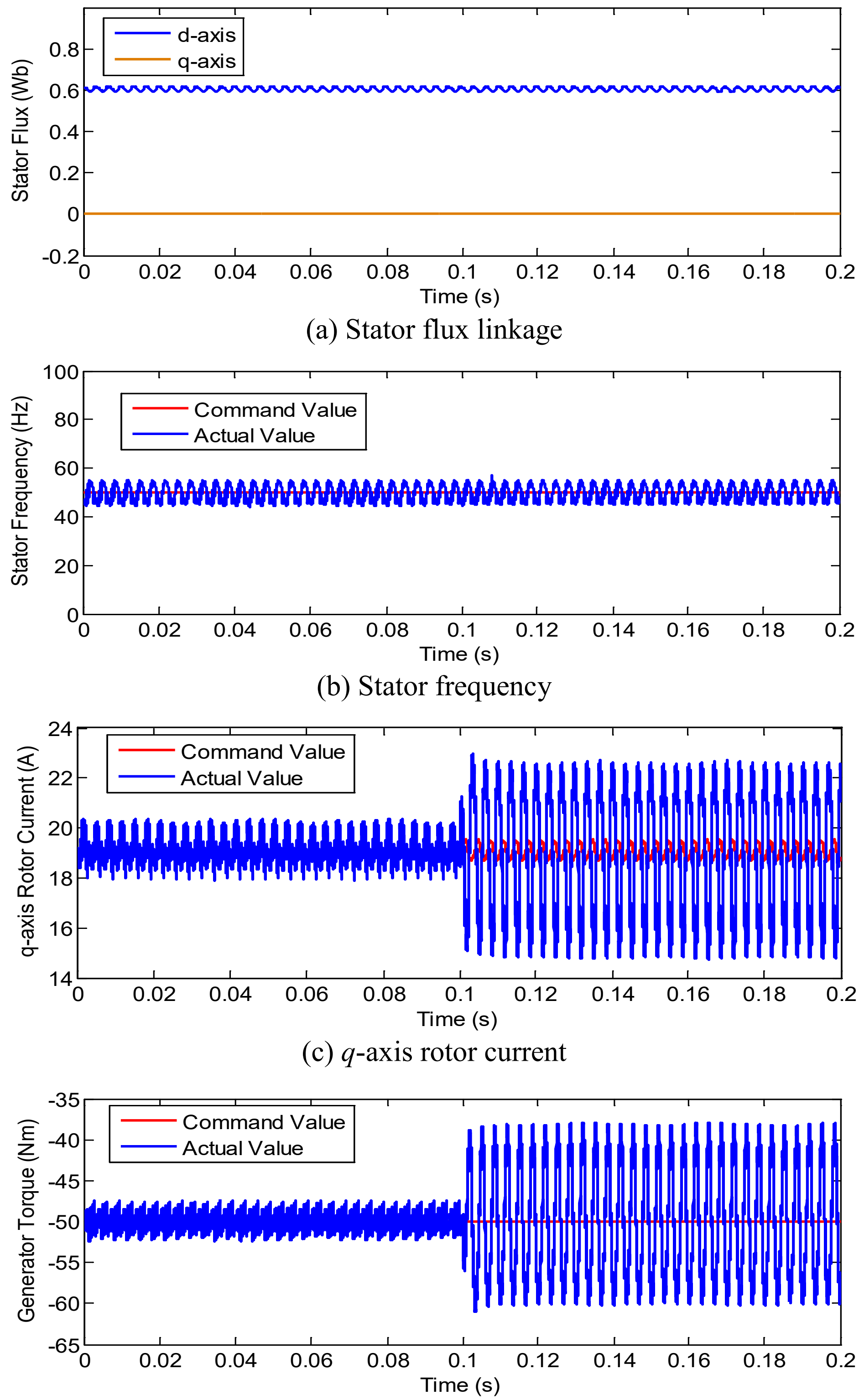

(a) Stator flux linkage

(b) Stator frequency

(c) q-axis rotor current

(d) Electromagnetic torque

Figure 5.9. Simulation test with MRF controller on before 0.1 second (constant stator frequency)

The simulation result for the q-axis rotor current is shown in Figure 5.9(c). As can be seen, with the MRF controller engaged, the system demonstrates much better tracking performance compared with the case without the proposed MRF controller. The electromagnetic torque of the DFIG is shown in Figure 5.9(d). With the MRF controller engaged, the actual torque value is much closer to the torque command, the torque ripple (peak-peak value) is around 0.06 (p.u.), i.e. 6% of the rated torque. In contrast, without the MRF controller, the actual torque value demonstrates large oscillation around the commanded value, the torque ripple is as large as 0.35 (p.u.).

FFT analysis result of the actual electromagnetic torque is summarized in Table 5.1. Note that in this study, the MRF controller is mainly designed to reduce the 6^{th} order harmonics in the electromagnetic torque. From Table 5.1, it is shown that the magnitude of the 6^{th} order harmonic component in the electromagnetic torque is as large as 0.16 (p.u.) in the absence of the proposed MRF controller. When the MRF controller is engaged, the 6^{th} order harmonic magnitude of the electromagnetic torque is reduced drastically to 0.00071 (p.u.), which is merely 0.44% of the case without the MRF controller. The magnitude of the 12^{th} order harmonic component in the electromagnetic torque is also shown in Table 5.1. Without the MRF controller, the 12^{th} order harmonic magnitude is about 0.014 (p.u.). When the MRF controller is active, the 12^{th} order harmonic magnitude is reduced to 0.0095 (p.u.).

Table 5.1. FFT analysis of the electromagnetic torque (simulation test)

Case	**6^{th} order harmonic magnitude**	**12^{th} order harmonic magnitude**
MRF ON	0.00071 p.u.	0.0095 p.u.
MRF OFF	0.16 p.u.	0.014 p.u.

5.5.2 Simulation Results with Varying Stator Frequency

For the studied DFIG-DC system, unlike conventional DFIG-AC system, the stator frequency is not restricted. The freedom in the operation of stator frequency requires the torque ripple mitigation scheme to be robust against stator frequency variation. As introduced previously, the rotating reference frame of the MRF based controller is synchronized with the stator frequency. As a result, the proposed MRF based torque ripple mitigation scheme should be robust against changes in the stator frequency.

In this simulation test, the performance of the MRF controller with varying stator frequency will be demonstrated. The initial stator frequency reference is set as 50 Hz. Then, in 0.2 seconds, the stator frequency command is ramped up to 60 Hz. The simulation test results are shown in Figure 5.10.

Due to the fact that the DC link voltage is relatively constant, then, the product of stator flux linkage and the stator frequency will also be approximately constant, to increase the stator frequency, the stator flux linkage need to be reduced, as can be seen from Figure 5.10(a). Figure 5.10(b) demonstrates that the actual stator frequency increases from 50 Hz to 60 Hz, as the d-axis stator flux decreases. The *q*-axis rotor current is shown in Figure 5.10(c). As can be seen, during the test, the actual i_{rq} can closely track the command value i_{rq}^*, even with varying stator frequency The electromagnetic torque shown in Figure 5.10(d) indicates that the torque ripple mitigation performance of the proposed MRF controller is consistent with variation of stator frequency. In another word, the robustness of the proposed MRF based controller against stator frequency deviation has been demonstrated.

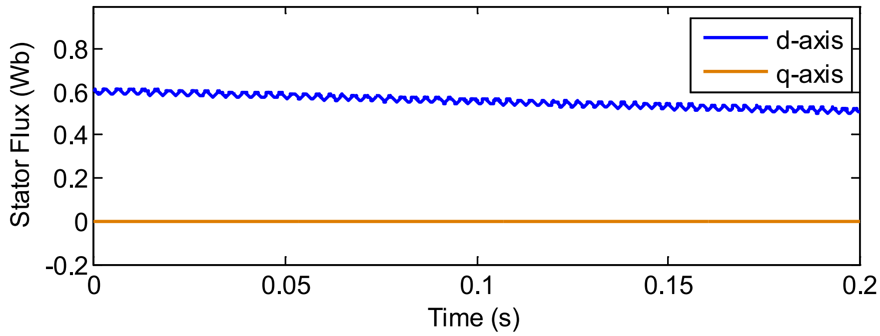

(a) Stator flux linkage

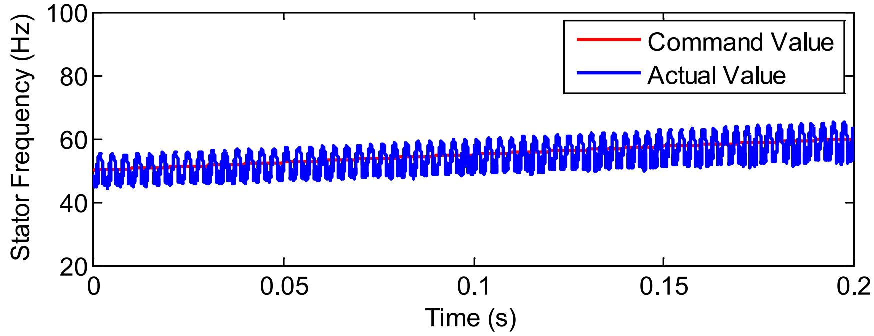

(b) Stator frequency

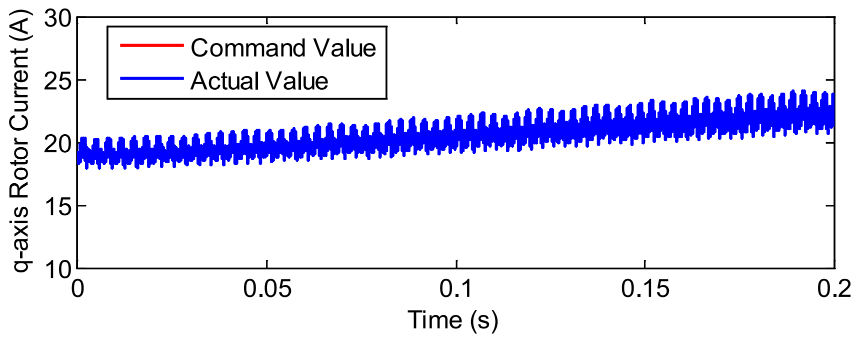

(c) q-axis rotor current

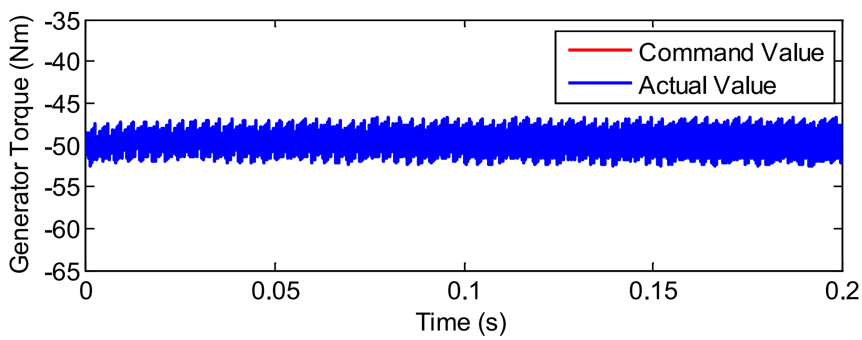

(d) Electromagnetic torque

Figure 5.10. Simulation test with MRF controller on (varying stator frequency)

To serve as a benchmark for comparison, the varying stator frequency test is then performed without the proposed MRF controller. The electromagnetic torque profile with MRF controller on and off is plotted in Figure 5.11 for easy comparison.

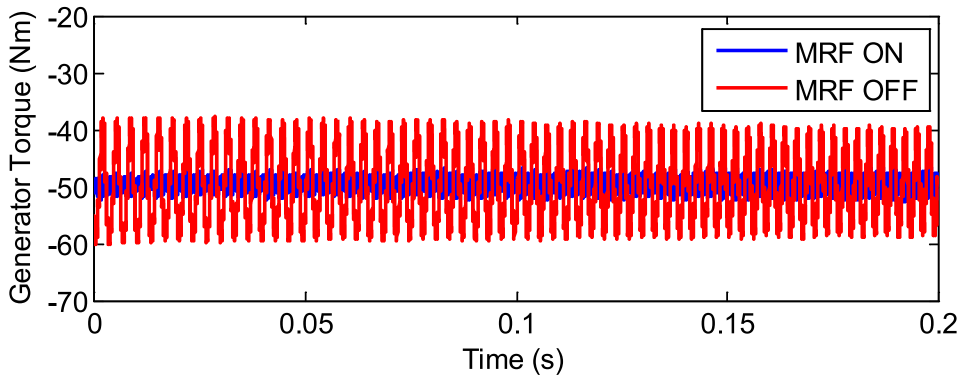

Figure 5.11. Electromagnetic torque: MRF ON vs. MRF OFF (varying stator frequency)

As can be seen, even with varying stator frequency, compared to the case without the MRF controller, the torque ripple is much smaller when the proposed MRF controller is used.

5.6 Experimental Results

To better investigate the performance of the proposed algorithm, it is necessary to perform experimental evaluation. To this end, a test rig is designed and built as shown in Figure 5.12. The parameters of the DFIG used in the experimental study are the same with the ones used in simulation study, the parameters are summarized in the table included in Appendix A.

A 10 KW permanent magnetic synchronous motor (PMSM) is used as the prime mover to emulate the high-speed shaft of the gearbox in a wind turbine. A universal off-the-shelf motor driver is used to drive the prime mover PMSM. A hollow-shaft encoder is mounted on the DFIG rotor shaft to measure the rotor angular position during operation.

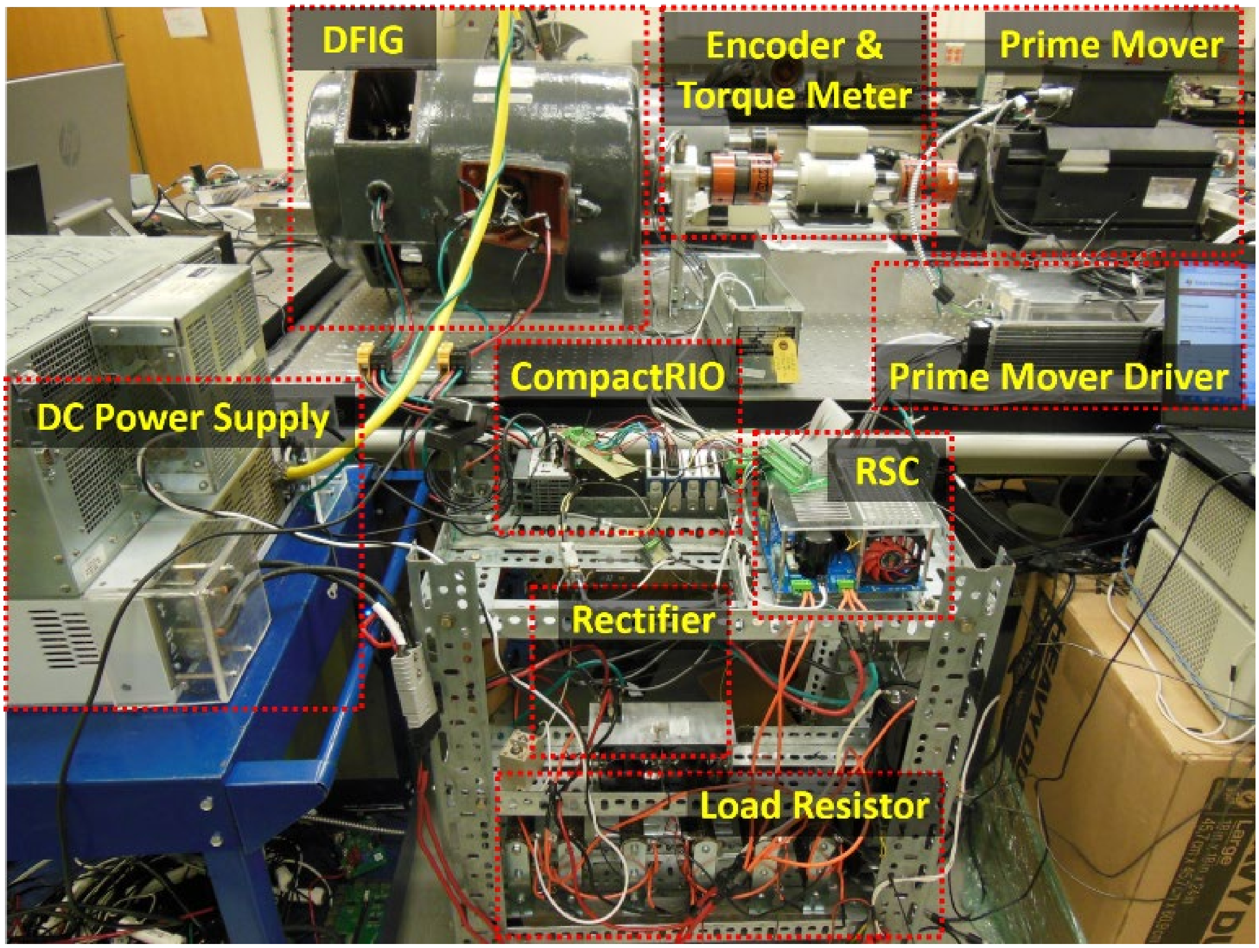

Figure 5.12. Test rig of the DFIG-DC system

A 2 KW motor control evaluation board (STEVAL-IHM028V2) is used as the rotor side converter (RSC). For fast prototyping, CompactRIO from National Instruments is used as the controller. The CompactRIO consists of a real-time controller (cRIO-9025), an FPGA controller (cRIO-9118) and reconfigurable plug-n-play I/O modules. For this application, the control algorithm is mainly implemented on the FPGA controller for fast processing speed. A resistor bank composed of 18 power resistors is used as the load resistor. A large capacitor (3 mF) and the load resistor are connected to the DC terminal of the system to emulate the DC link. Hall effect current sensors are used to measure both the stator side and rotor side phase currents. During start up, a

DC power supply is connected to the DC link to provide the power for the RSC. Once the system starts to generate electricity, the system will be able to sustain the DC bus voltage by itself. Then, the DC power supply will be disconnected.

The control scheme implemented for the experimental study is shown in Figure 5.13. As can be seen, the control structure is almost the same as the one used in simulation study. The only difference is that the stator frequency PI is eliminated in the experimental study to simplify the controller design. Similar to simulation study, two different tests were performed. During the first test, the stator frequency is kept constant. The stator frequency in the second test is changing to evaluate the performance consistency of the MRF controller under varying stator frequency.

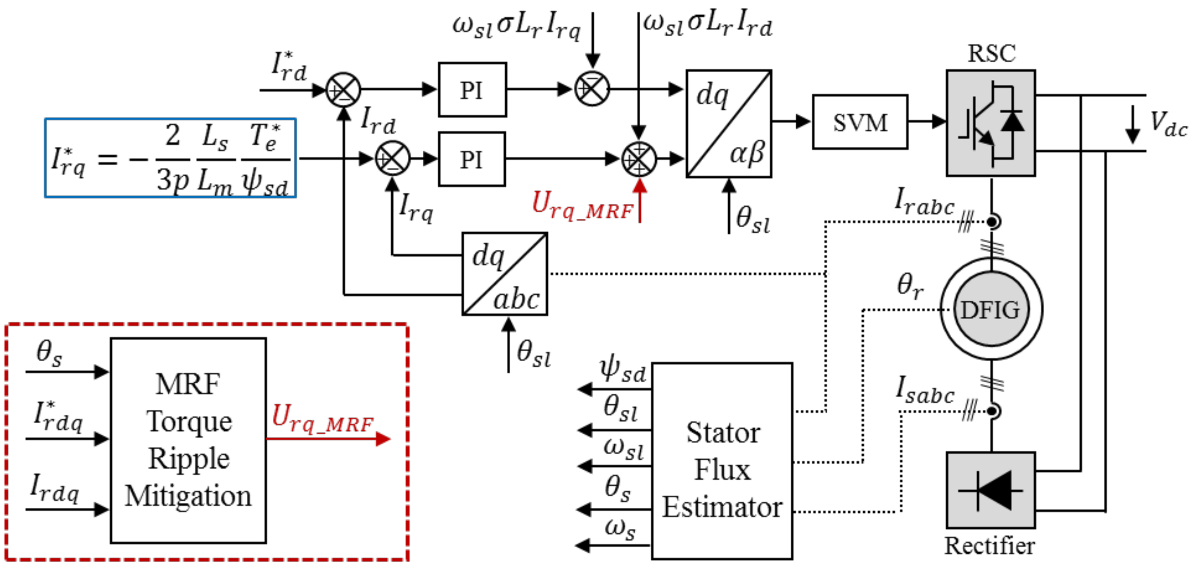

Figure 5.13. Control diagram of MRF based torque ripple mitigation control (experimental test)

5.6.1 Experimental Comparison: MRF Controller ON vs. OFF

In this experimental test, the MRF controller is engaged before 1 second. After 1 second, the MRF controller is turned off and the output of the MRF controller U_{rq_MRF} is set as zero. The experimental results are shown in Figure 5.14.

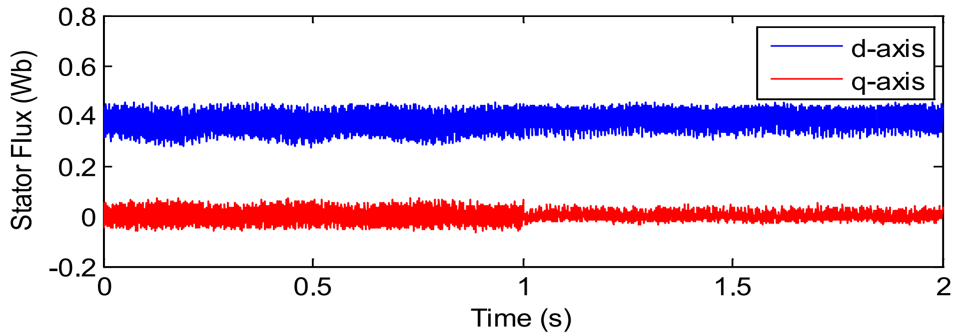

(a). Stator flux linkage

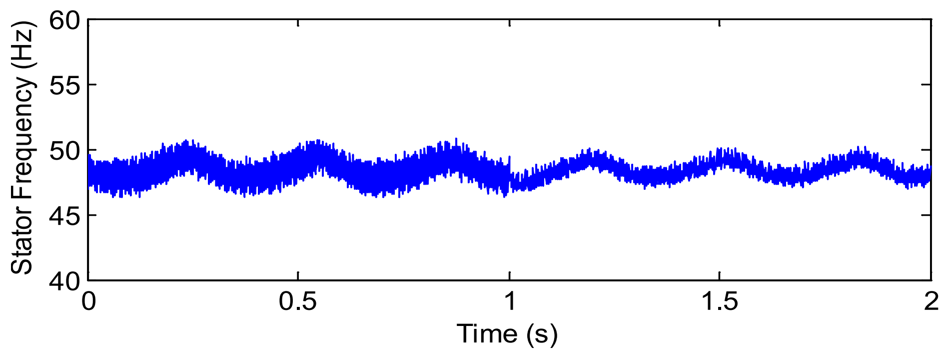

(b). Stator frequency

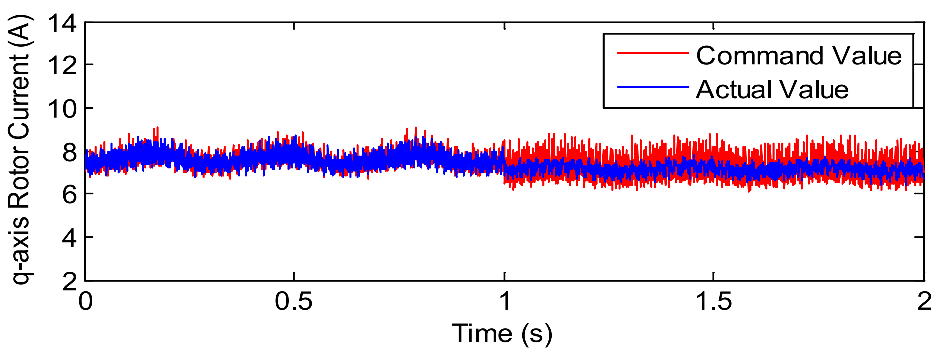

(c). q-axis rotor current

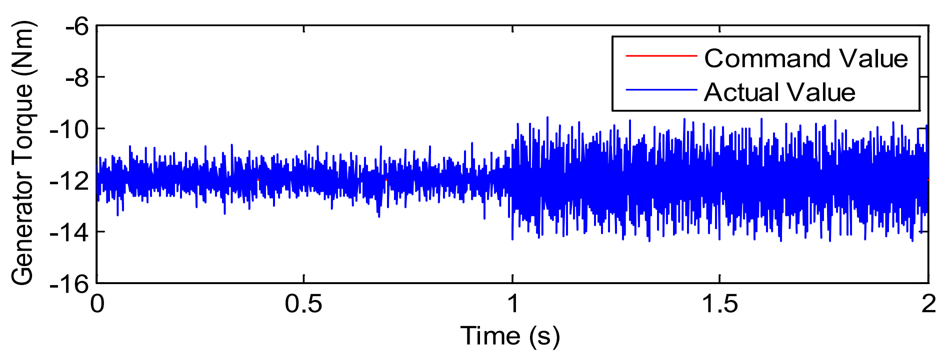

(d). Electromagnetic torque

Figure 5.14. Experiment test with MRF controller on before 1 second (constant stator frequency)

In this test, the *d*-axis rotor current command is set as a constant value (8 A). As a result, the average value of the stator flux and the stator frequency will also be constant, assuming the DC link voltage is relatively constant. Notice that there exists a low frequency oscillation in the stator frequency waveform shown in Figure 5.14(b). This is due to the voltage ripple in the DC link. From Figure 5.14(c), it is obvious that the system can track the q-axis rotor command much closely when the MRF controller is activated. With the MRF controller on, the torque ripple (peak-peak value) is around 0.035 (p.u.). When the MRF controller is turned off, the torque ripple increases to 0.073 (p.u.). The torque ripple is reduced by more than 50% when the MRF controller is used.

The FFT analysis result for the electromagnetic torque is summarized in Table 5.2. As can be seen, without the proposed MRF controller, the magnitude of the 6^{th} order harmonic in the electromagnetic torque is 0.0151 (p.u.). When the MRF controller is engaged, this value is reduced to 0.0017 (p.u.), which is about 11.3% of the case without the MRF controller. The 12^{th} order harmonic torque is almost the same for both cases, this is no surprising since the MRF controller in this study is designed to reduce the 6^{th} order torque harmonic only.

Table 5.2. FFT analysis of the electromagnetic torque (experimental test)

Case	**6^{th} order harmonic magnitude**	**12^{th} order harmonic magnitude**
MRF ON	0.0017 p.u.	0.006 p.u.
MRF OFF	0.0151 p.u.	0.0061 p.u.

5.6.2 Experiment Results with Varying Stator Frequency

As stated in the simulation study, it is important to evaluate the performance of the proposed MRF controller under varying stator frequency operation. The experimental test results with varying stator frequency are shown in Figure 5.15. In this test, the d-axis rotor current command

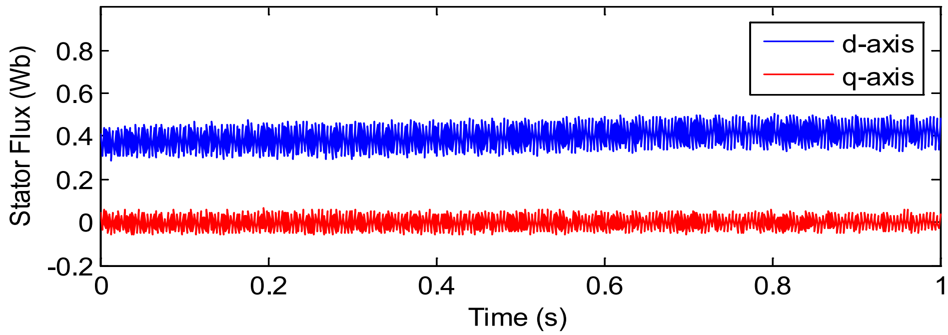

(a). Stator flux linkage

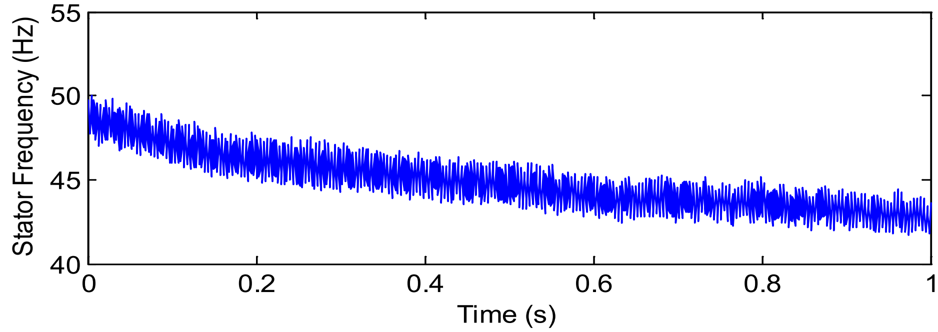

(b). Stator frequency

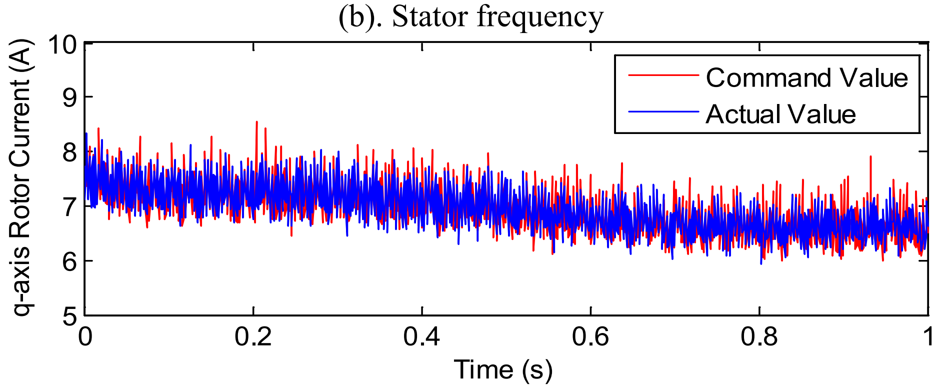

(c). q-axis rotor current

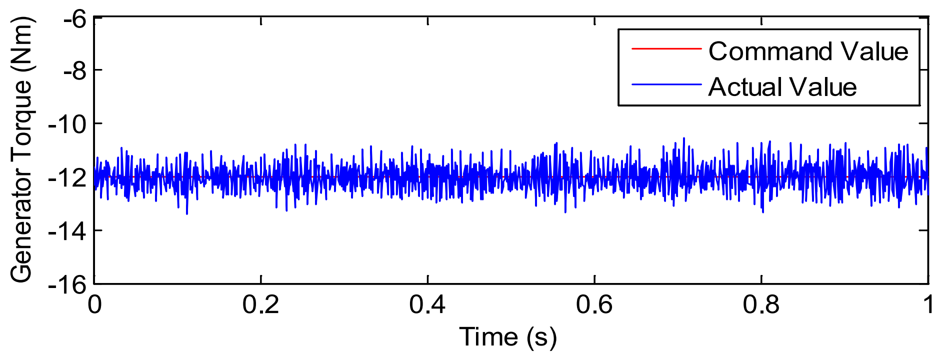

(d). Electromagnetic torque

Figure 5.15. Experiment test MRF controller on (varying stator frequency)

value is increased from 8 A to 10 A in 1 second. Based on Equation (5-2), the increase of I_{rd} will lead to increase of stator flux value (see Figure 5.15(a)). Since the DC link voltage is approximately constant, the increase of stator flux will cause decrease of stator frequency, which can be observed in Figure 5.15(b). The actual and command value of q-axis rotor current is shown in Figure 5.15(c).

The electromagnetic torque profile is shown in Figure 5.15(d). During the variation of stator frequency, the performance of torque ripple reduction does not show apparent deterioration, which indicates that the proposed MRF controller is very robust against stator frequency deviation.

The same test with varying stator frequency is then performed without the MRF controller. The electromagnetic torque for the case with MRF and the case without MRF are plotted in Figure 5.16. Through the comparison, it is demonstrated that the proposed MRF controller can effectively suppress the torque ripple regardless of the stator frequency variation.

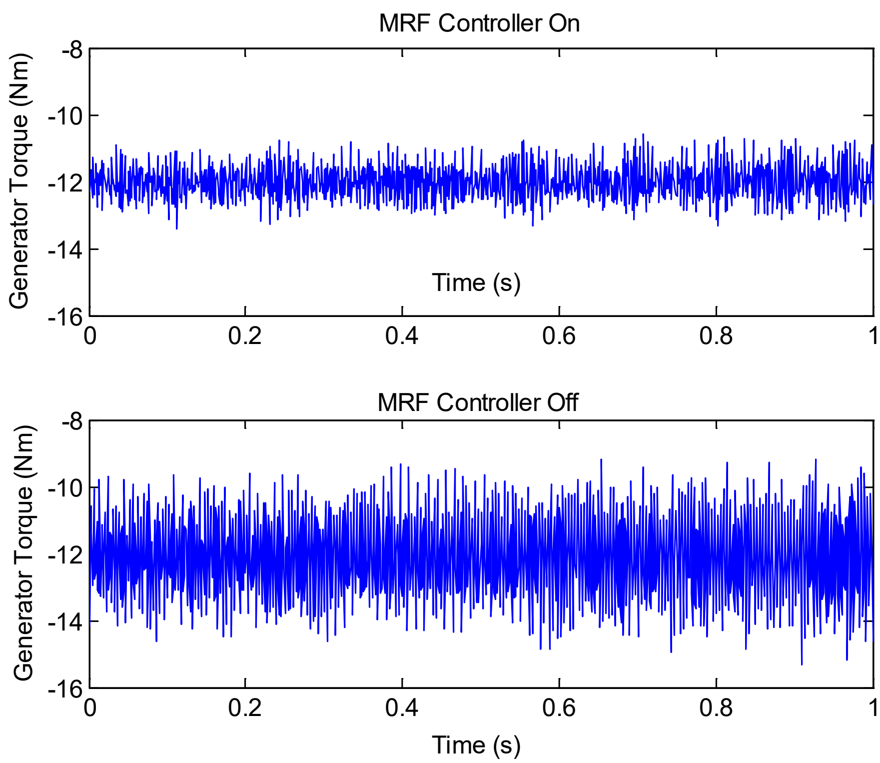

Figure 5.16. Experiment test MRF controller ON vs OFF (varying stator frequency)

5.7 Summary and Conclusion

In this chapter, a multiple reference frame (MRF) based scheme is proposed to reduce the torque ripple in the DFIG-DC system. Compared with other algorithms investigated in the existing literature, the proposed MRF based method does not require detailed model information. Also, since the rotating reference frame of the MRF control scheme is synchronized with the stator frequency, the proposed MRF based torque ripple mitigation scheme is very robust against stator frequency variation.

To evaluate the performance of the proposed algorithm, both simulation and experimental tests were performed in this study. The test results demonstrate that the proposed control algorithm can successfully suppress the torque ripple in the DFIG-DC system.

Through variable stator frequency operation test, the proposed MRF controller demonstrates consistent performance with varying stator frequency, which indicates that the proposed scheme is indeed very robust against stator frequency variation.

CHAPTER 6

OPTIMAL STATOR FREQUENCY CONTROL OF DFIG-DC SYSTEM*

The problem of optimal stator frequency control for DFIG-DC system is investigated in this chapter. For DFIG-DC system, the extra degree of freedom in stator frequency control introduces an interesting question: how to optimally regulate the stator frequency of the DFIG-DC system? It is demonstrated through simulation and experimental tests that the efficiency of the DFIG-DC system varies with the change of stator frequency. At certain frequency, the efficiency of the DFIG-DC system is maximized. However, it is not viable in practice to determine the optimal stator frequency using model-based approaches, since an accurate power losses model is typically difficult to acquire. To this end, an Extremum Seeking Control (ESC) based scheme is proposed as a model-free solution to track the optimal stator frequency in real time, based on the feedback of estimated efficiency. Both simulations and experiments included in this chapter demonstrate that ESC can accurately find the optimal stator frequency that results in the highest operation efficiency for the DFIG-DC system.

6.1 Introduction and Research Motivation

As mentioned in Chapter 1, unlike conventional DFIG-AC system, the stator frequency of the DFIG-DC system is not imposed by the DC grid. To maximize the efficiency of power conversion for field operation of DFIG wind turbine generators with DC link, it is necessary to investigate how the stator frequency of the DFIG-DC system affects its operating efficiency, and how the optimal stator frequency regulation be achieved in practical implementation.

As introduced in Chapter 2, existing studies on optimal stator frequency control of DFIG-DC system relies heavily on the accuracy and availability of the model information. However, a simple analysis given in this chapter indicates that it is typically very difficult, if not impossible, in practice to acquire an accurate power losses model for the DFIG-DC system. Therefore, it is favorable to seek for an optimization scheme such as extremum seeking control that does not rely on model information.

Both simulation and experimental tests included in this chapter indicate that the efficiency of the DFIG-DC system demonstrates a unimodal curve with reference to the stator frequency. Therefore, the global optimal working point is readily achievable by ESC.

In this chapter, an ESC based optimal stator frequency control algorithm is designed and implemented, with the objective to increase the operation efficiency of the DFIG-DC system. To evaluate the effectiveness and performance of the proposed control scheme, both simulation test and experimental tests are performed.

6.2 Overview of the DFIG-DC System

The configuration and basic mathematical model of the DFIG-DC have already been introduced in Chapter 5. In this subsection, the focus is on a simple analysis of electrical power losses in DFIG-DC system and how the stator frequency could potentially affect the power losses.

6.2.1 Electrical Power Losses in DFIG-DC System

As can be seen from Figure 6.1, the electrical power losses in the studied DFIG-DC system mainly occur in three locations: 1) DFIG; 2) diode bridge rectifier; 3) rotor side converter (RSC).

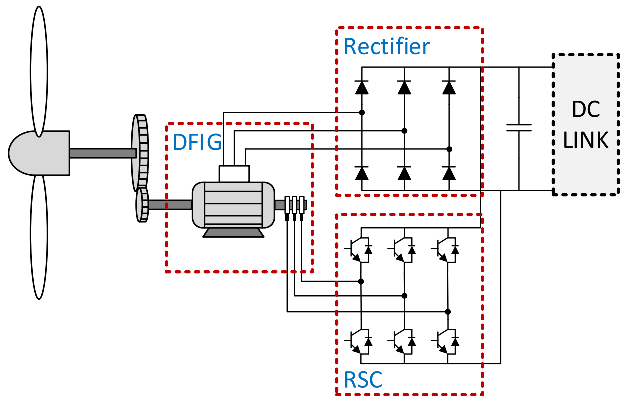

Figure 6.1. Electrical power loss location in DFIG-DC system

To analyze the power losses in the DFIG, for ease of reference, the equivalent circuit of DFIG originally shown in Figure 5.2 is again plotted as shown in Figure 6.2.

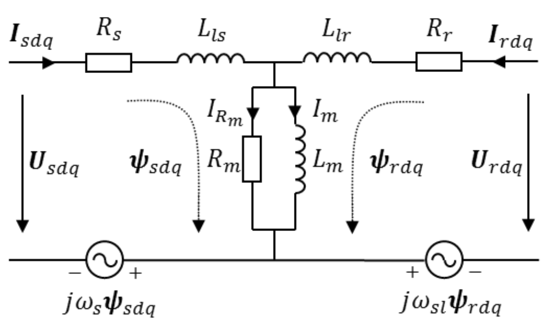

Figure 6.2. Equivalent circuit of DFIG (per phase)

Based on the equivalent circuit, the power losses in one phase of the DFIG can be expressed as

$$P_{DFIG\_Loss} = \left|\boldsymbol{I}_{sdq}\right|^2 R_s + \left|\boldsymbol{I}_{rdq}\right|^2 R_r + \left|\boldsymbol{I}_{R_m}\right|^2 R_m \tag{6-1}$$

The first two terms represent the copper power losses of DFIG. The last term, as introduced previously, represents the iron losses, which is consist of eddy current loss and magnetic hysteresis loss. An engineering calculation of the per unit value iron loss (W/kg) can be approximated formulated as [85]

$$w_f = B_m^2 \left[\sigma_H \left(\frac{f}{100} \right) + \sigma_E d^2 \left(\frac{f}{100} \right)^2 \right] \tag{6-2}$$

Where B_m is the maximum magnetic flux density, f stands for the electromagnetic field frequency, d is the thickness of the iron core lamination sheet, σ_H and σ_E stands for magnetic hysteresis power loss coefficient and eddy current power loss coefficient respectively. As can be seen, for a given electric motor, the iron loss generally increases with the magnetic flux density and the frequency of the alternating electromagnetic field. As a result, the pseudo resistor R_m that is used to represent the iron loss varies with both the change of flux density and frequency and is therefore difficult to determine.

As shown in Figure 6.1, besides power loss in the DFIG, power loss also occurs in the diode bridge rectifier and the rotor side converter. The average power loss in one diode can be calculated as

$$P_{Diode\_Loss} = \frac{1}{T} \int_{t_{on}}^{t_{off}} u_f(t) i_f(t) dt \tag{6-3}$$

Where T is the switching period, t_{on} is the time for the start of commutation of the diode, t_{off} is the time for the termination of commutation of the diode. $u_f(t)$ is the forward voltage of the diode at time instance t. $i_f(t)$ is the forward current of the diode at time instance t. When ignoring the switching transit during switching on and switching off, the forward voltage $u_f(t)$ can be seen as a relatively constant value. This is only valid when the switching frequency is low. For the application of DFIG-DC system, the switching frequency of the diode bridge rectifier is limited to a range around the rated frequency (60 Hz) of the DFIG machine. Therefore, the switching loss in the diode bridge rectifier can be ignored. The power loss in the diode bridge rectifier can then be approximately seen as in proportional with the stator current.

The rotor side converter is essentially a three-phase full bridge PWM inverter. The power loss equation for each IGBT is similar to Equation (6-3) and can be expressed as

$$P_{IGBT\_Loss} = \frac{1}{T}\int_{t_{on}}^{t_{off}} u_f(t) i_f(t) dt \tag{6-4}$$

However, the switching transit can no longer be ignored since the switching frequency of the rotor side converter is typically 10 kHz or even higher. Therefore, it is much more difficult to accurately calculate the power loss in the rotor side converter.

By combining all the power loss terms analyzed above and assuming a balanced operation for both the stator and rotor of the DFIG, the total electrical power losses in the DFIG-DC system can be formulated as

$$P_{Total\_Loss} = 3\left|\boldsymbol{I}_{sdq}\right|^2 R_s + 3\left|\boldsymbol{I}_{rdq}\right|^2 R_r + 3\left|\boldsymbol{I}_{R_m}\right|^2 R_m + 6P_{Diode\_Loss} + 6P_{IGBT\_Loss} \tag{6-5}$$

To maximize the efficiency of the DFIG-DC system, one needs to minimize the total power losses, without compromising other control objective such as generator torque.

6.2.2 Stator Frequency and Efficiency of DFIG-DC System

As mentioned in the previous section, the stator frequency in DFIG-DC system is not imposed by the DC grid. This extra degree of freedom in control introduces an interesting question regarding the value at which the stator frequency should be regulated.

For a given DFIG rotor shaft speed ω_r, the slip ratio $s = \frac{\omega_s - \omega_r}{\omega_s}$ will change with the variation of synchronous stator frequency ω_s. Based on [86], the power flow through the rotor winding of the DFIG is approximately given by

$$P_r = sP_e \tag{6-6}$$

Where P_e is the total electric power generated by the DFIG. The approximate power flow through the stator winding of the DFIG can be represented as

$$P_s = (1-s)P_e \tag{6-7}$$

For a given setting of rotor speed and generator torque, based on Equation (6-6) and (6-7), it is obvious that the proportion of power flow through the rotor/stator is determined by the slip and hence the stator frequency. Assuming constant DC bus voltage, the stator current will increase with the proportion of power flow through the stator winding. From Equation (6-5), one can see that the power loss through the stator resistor and the diode rectifier will increase. Similarly, when more power is flown through the rotor side of the DFIG, the power loss in the rotor resistor and RSC will increase. For the iron loss term in Equation (6-5), however, it is difficult to find a direct correlation with reference to the slip or stator frequency change. The reason will be explained later in the subsequent section.

To maximize the efficiency of the DFIG-DC system equals to minimizing the total power losses. The control objective for the optimal stator frequency controller is to find the optimal stator frequency that achieves optimal distribution of rotor power and stator power, so that the total power losses are minimized. Since it is difficult to obtain an accurate power loss model of the system (especially for the iron loss term and the power inverter loss term), it is not feasible in practice to rely on model-based optimization algorithm. In this chapter, a non-model-based optimization algorithm (ESC) is implemented to find the optimal stator frequency that results in improved operation efficiency of the DFIG-DC system.

6.3 ESC Based Optimal Stator Frequency Control

In this subsection, the principle of stator frequency control is first introduced. Then, the structure of the ESC based optimal stator frequency control is illustrated. The principle and general design guideline of ESC controller have already been introduced in Chapter 3.

6.3.1 Stator Frequency Control of DFIG-DC System

As analyzed in [53] and [11], the stator voltage of the DFIG is clamped to the three-step waveform as shown in Figure 5.3. Then, the fundamental component of the stator voltage (RMS value) can be expressed as

$$V_{s1} = \frac{\sqrt{2}V_{dc}}{\pi} \tag{6-8}$$

The relationship between the fundamental stator voltage V_{s1} and fundamental stator EMF (electromotive force) E_{s1} can be described as

$$E_{s1} = V_{s1} - R_s I_{s1} \approx V_{s1} \tag{6-9}$$

The approximation in the upper equation is due to the fact that the stator resistance is typically very small and can be neglected. By considering the stator flux at steady state, the relationship between the fundamental stator EMF E_{s1} and stator frequency ω_s can be expressed as

$$E_{s1} = \omega_s \psi_s \tag{6-10}$$

Assuming the DC link voltage is relatively constant, from Equation (6-8) through Equation (6-10), it is obvious that the product of stator flux and stator frequency is approximately constant. As a result, the increase/decrease of stator flux will lead to a decreased/increased stator frequency. Since the iron loss shown in Equation (6-2) is affected by both stator frequency and stator flux level, it is not straight forward to determine how the iron loss would change with the variation of the stator frequency.

By varying the magnitude of the stator flux, the stator frequency of the DFIG-DC system can be regulated to the desired value. Under the stator flux FOC (field-oriented control) framework adopted in this study, the *q*-axis stator flux linkage is close to zero. In addition, the *d*-axis stator flux is approximately the same as the combined stator flux. Also, it is analyzed in [53] that the *d*-axis stator current is almost zero. As a result, the stator flux equation shown in Equation (5-2) can be further written as

$$\begin{cases} \psi_s \approx \psi_{sd} = L_s I_{sd} + L_m I_{rd} \approx L_m I_{rd} \\ \psi_{sq} = L_s I_{sq} + L_m I_{rq} \approx 0 \end{cases} \tag{6-11}$$

From the equation shown above, it is clear that the stator flux and hence the stator frequency can be readily regulated by properly controlling the *d*-axis rotor current.

6.3.2 Design of The ESC Based Optimal Stator Frequency Controller

With stator flux linkage FOC, as shown in Equation (5-20), the *q*-axis rotor current can be used to regulate the generator torque. The overall control diagram is shown in Figure 6.3. As introduced in Chapter 5, a stator flux angle estimator similar to the one used in [58] is adopted to estimate the stator flux angle and slip angle in real time.

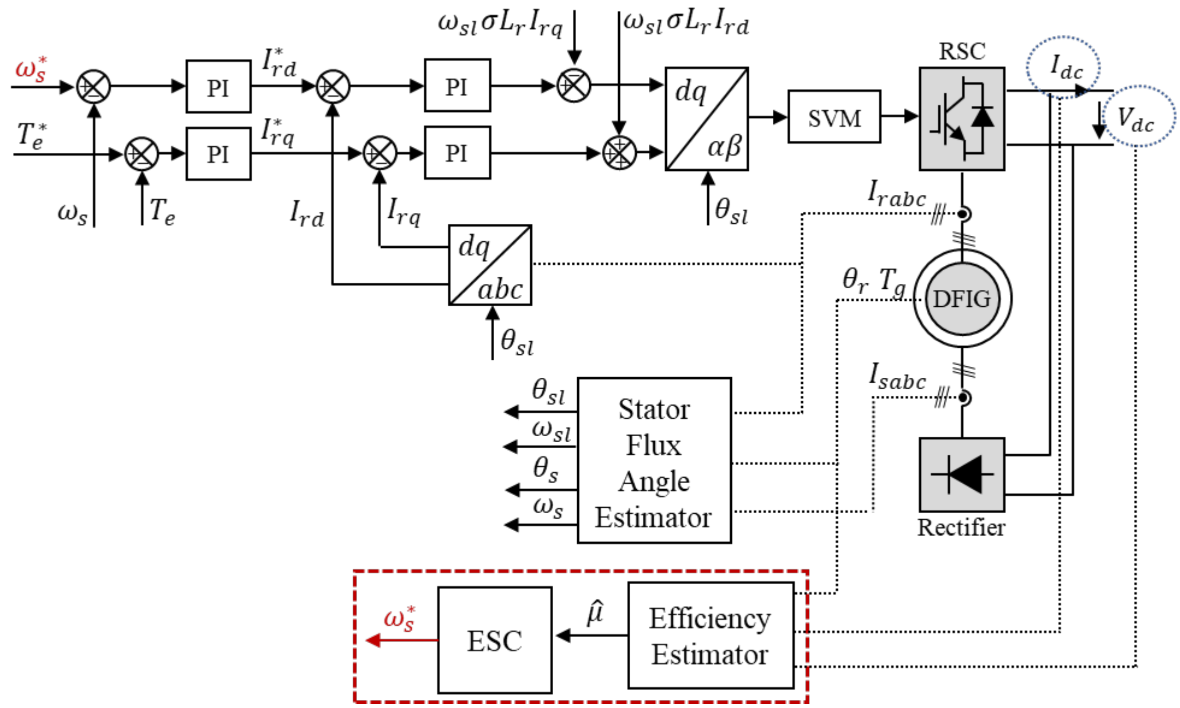

Figure 6.3. Overall control diagram of ESC based optimal stator frequency control for DFIG-DC system

The efficiency of the DFIG-DC system is defined as

$$\mu = \frac{V_{dc} I_{dc}}{\omega_r T_g} \tag{6-12}$$

Where the product of DC bus voltage V_{dc} and current I_{dc} represents the electrical power generated by the DFIG, while the product of DFIG shaft torque T_g and shaft rotational speed ω_r is the mechanical power input through the DFIG rotor shaft. Note that ω_r is derived by taking time derivative of rotor position measurement θ_r. The calculated efficiency μ is then passed through a low pass filter to obtain a smoothed-out estimation of efficiency $\hat{\mu}$. The estimated efficiency $\hat{\mu}$ is then fed into the ESC controller to calculate the stator frequency reference ω_s^*.

6.4 Simulation Study

To evaluate the performance of the proposed control algorithm, a DFIG-DC system model is built in Simulink environment. The parameters of the DFIG model are included in Appendix A. Note that for all the tests (performance map test, ESC test), the generator torque command is fixed at -20 Nm.

6.4.1 Performance Map: Efficiency vs. Stator Frequency

As a benchmark for the evaluation of the ESC controller test results, it is important to obtain the performance map of efficiency with reference to different stator frequency. Figure 6.4(a) shows the efficiency curve of DFIG-DC system with different setting of stator frequency. Note that the rotor speed is fixed at 1600 rpm during this performance map test.

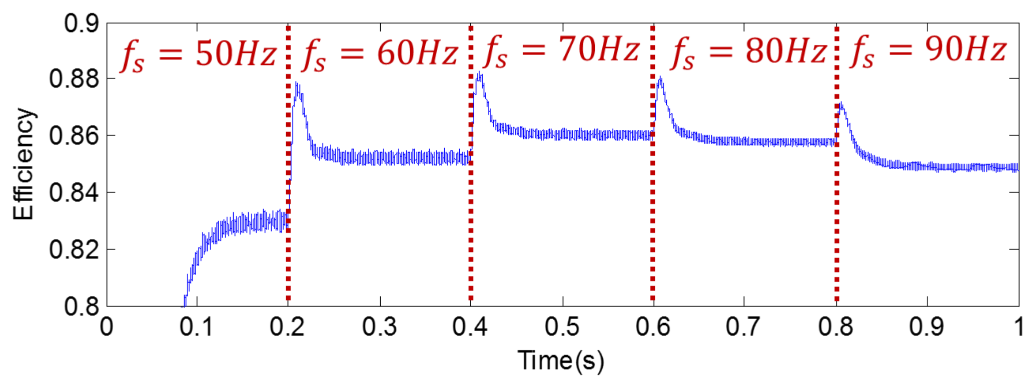

(a). Efficiency curve with different stator frequency setting

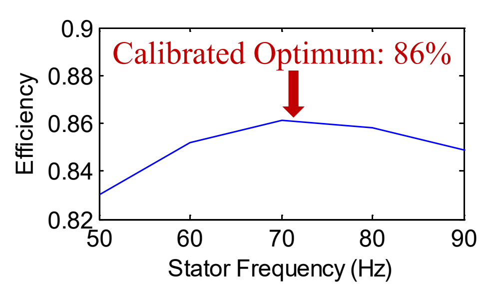

(b). Static efficiency map with reference to stator frequency

Figure 6.4. DFIG-DC system efficiency vs. stator frequency (rotor speed: 1600 rpm)

The peaks shown in Figure 6.4(a) are due to the transient of the stator frequency control. From the efficiency static map shown in Figure 6.4(b), one can see that the efficiency is maximized at around 70 Hz stator frequency. Table 6.1 summarizes the calibrated optimal stator frequency under different DFIG rotor speed. The synchronized stator frequency corresponding to the rotor speed is also shown in this table. Note that the pole pairs of the DFIG used in the simulation is $p = 3$. As can be seen, the optimal stator frequency results in highest efficiency generally increases with the rotor speed. Also, the stator frequency synchronized with the rotor speed is not always the optimal frequency that results in the highest efficiency.

Table 6.1. Optimal stator frequency vs. rotor speed

rotor speed (rpm)	**600**	**800**	**1000**	**1200**	**1400**	**1600**	**1800**
synchronize frequency (Hz)	30	40	50	60	70	80	90
optimal frequency (Hz)	40	50	50	60	70	70	80

6.4.2 Simulation Test: ESC Based Optimal Stator Frequency Control of DFIG-DC System

As introduced in the previous subsection, the calculated efficiency μ is passed through a low pass filter to obtain a smoothed-out estimation of system efficiency $\hat{\mu}$. The low pass filter in the efficiency estimator can be seen as the dominating part of the plant's dynamics. For this simulation study, the bandwidth of the low-pass filter is set at 60 rad/s. As a result, the overall bandwidth of the plant is approximately 60 rad/s as well.

Based on the design guideline introduced in Chapter 3, the dither frequency should be selected to be in the pass band of the plant's dynamics. For this simulation test, dither frequency is set as 50 rad/s. The cut-off frequency of both the low-pass filter (48 rad/s) and high-pass filter (48 rad/s) should be smaller than the dither frequency. The dither amplitude is set as 2.5 Hz, the integrator gain is set as 20000.

For the ESC test, the DFIG rotor speed is fixed at 1600 rpm. the initial stator frequency is set as 40 Hz. The ESC controller is turned on from 0.4 second. The simulation result is shown in Figure 6.5.

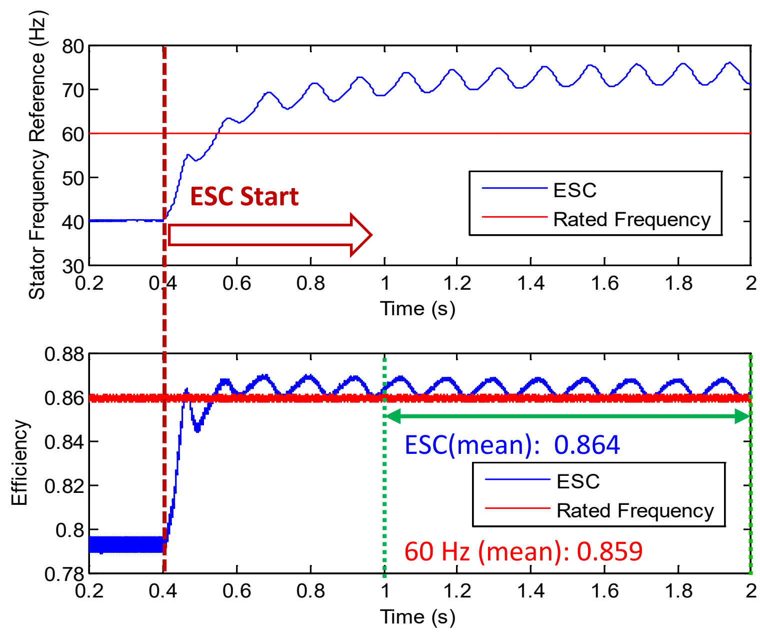

Figure 6.5. Simulation result of ESC based optimal stator frequency control (rotor speed: 1600 rpm)

As can be seen, about 0.6 second after the ESC controller is engaged, the ESC converges to around 72 Hz, which is close to the calibrated optimal value shown in Table 6.1. The average efficiency of the DFIG-DC system increased from 79.3% at 40 Hz to 86.4% at around 72 Hz. The efficiency of the DFIG-DC system is increased by 7.1%. If the stator frequency is fixed at the rated value of 60 Hz, the efficiency of the system is 85.9%, which is 0.5% lower than what the ESC achieved. Note that ESC achieves even higher efficiency than the calibrated optimal efficiency (80%) shown in Figure 6.4[b], this is due to the relatively low resolution of the efficiency map.

6.5 Experimental Study

To further evaluate the performance of the proposed scheme, the same test rig shown in Figure 5.12 is used to perform the experimental study. Five hall effect current sensors are used in this test rig. One of the current sensors is used to measure the DC current flow through the load resistor. The other four sensors are used to measure the stator currents and rotor currents of the DFIG. The DC bus voltage can be readily measured from the inverter board that is used as the rotor side converter.

The control scheme for the experimental study is almost the same with the one shown in Figure 6.3 for the simulation study, with the exception that the stator frequency control loop is eliminated in the experimental study to simplify the controller design. Therefore, the output of the ESC controller is d-axis rotor current command instead of stator frequency command.

Note that for all the experimental tests (performance map test, ESC test), the generator torque command is fixed at -12 Nm, and the DFIG rotor speed is fixed at 900 rpm.

6.5.1 Performance Map: Efficiency vs. *d*-axis Rotor Current

Prior to ESC test, the performance map of efficiency with reference to *d*-axis rotor current I_{rd} is obtained as a benchmark for the evaluation of the ESC test result. The efficiency at different setting of I_{rd} (and the corresponding stator frequency) is summarized in Table 6.2.

Table 6.2. Efficcciency vs. *d*-axis rotor current (rotor speed: 900 rpm)

I_{rd} (A)	3.5	4.5	5.5	6.5	7.5	8.5	9.5	10.5	11.5	12.5	13.5	14.5
f_s (Hz)	60.4	57.2	53.9	51.0	48.1	45.2	42.8	40.3	37.8	35.1	33.7	33.5
μ (%)	72.4	73.4	75.1	76.4	77.7	78.4	80.0	78.7	77.6	73.1	67.5	65.1

As can be seen from the table, the efficiency of the DFIG-DC system reaches the maximum value of 80% when the d-axis rotor current is set as 9.5 A. The corresponding stator frequency is 42.8 Hz. Notice that if the stator frequency is regulated to the rated value (60 Hz), the efficiency is around 72.4%, which is considerably smaller than the maximum value (80%). The potential of big improvement in system efficiency shown in this table further justify the value of this study.

The efficiency curve with reference to the *d*-axis rotor current and stator frequency is shown in Figure 6.6. This figure indicates that the efficiency curve of the DFIG-DC system is unimodal with reference to *d*-axis rotor current or stator frequency. Since there is no local optimal working point, it should be very easy for the ESC controller to converge to the global optimal working point that results in the highest possible efficiency.

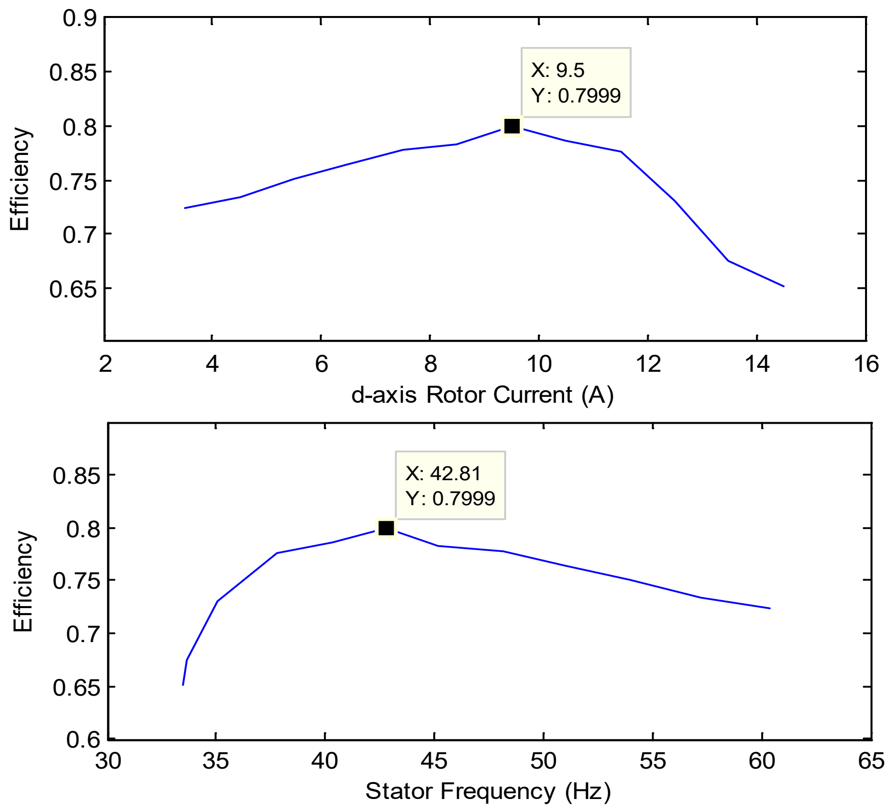

Figure 6.6. Efficiency map of the DFIG-DC test rig (rotor speed: 900 rpm)

6.5.2 Experimental Test: ESC Based Optimal Stator Frequency Control of DFIG-DC System

For the experimental study, the low-pass filter for the efficiency estimator has a cut-off frequency of 5 Hz (31.42 rad/s). For the ESC controller, the dither frequency is selected as 1 Hz (6.28 rad/s). 0.9 Hz (5.65 rad/s) is selected as the cut-off frequency for both the high-pass filter and the low-pass filter. The dither amplitude is set as 0.5 A. The integrator gain is set as 100.

To demonstrate the effectiveness of the proposed control scheme, two tests were performed with different settings of initial value (i.e. starting point of ESC controller). ESC test results with initial value of 4 A for the *d*-axis rotor current is shown in Figure 6.7. ESC is engaged at 1 second. After about 14 seconds, the ESC converges to around 9.5 A, which is the calibrated optimal working point according to Table 6.2. From the *d*-axis rotor current plot, high frequency harmonics are seen in the actual *d*-axis rotor current. This is normal for DFIG-DC system, since the stator voltage is highly distorted with harmonics (mainly -5^{th} & $+7^{th}$ order) due to the uncontrollable rectification process. The harmonics in the stator voltage would cause harmonics (mainly 6^{th} order) in the *d-q* axis rotor current. The detailed rationale can be found in [58]. Even with harmonics, it is obvious that the actual I_{rd} can successfully track the reference value given by the ESC controller.

Since the rotor speed is fixed at 900 rpm during the test, and the pole pair number of the DFIG used is 3, therefore, the corresponding rotor speed synchronous frequency is 45 Hz. From the measurement of the U-phase rotor current, one can see that as the stator frequency approaches to 45 Hz, the slip would approach zero. As a result, the frequency of the rotor current becomes lower. The calculated efficiency μ is shown in the bottom sub-plot. Note that at some point, the efficiency is even higher than 100%. This is normal due to the energy storage capability in the capacitor, inductance and mechanical rotating inertia. During the searching time (from 1 to 15 second) of ESC, the calculated efficiency demonstrates an increasing trend. The average value of the calculated efficiency after the ESC converges (15 - 30 second) is 79.3%, which is very close to the calibrated optimum value of 80% shown in Table 6.2.

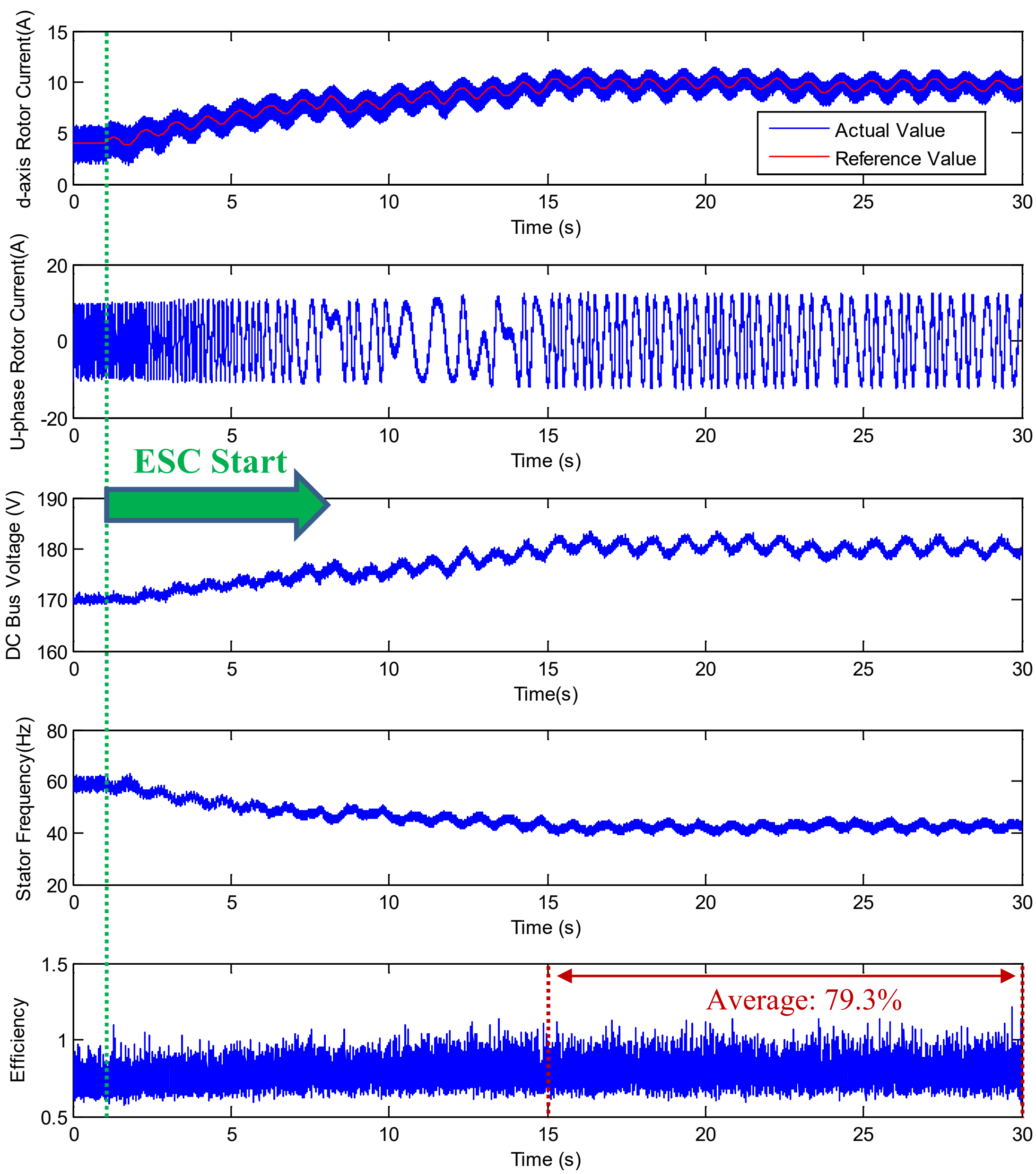

Figure 6.7. ESC test with initial d-axis rotor current of 4 A

The second ESC test is performed with the initial value of 14 A for the d-axis rotor current. The results are shown in Figure 6.8. Except for the setting of initial value, all the other control parameters are the same with the ones used in the first ESC test.

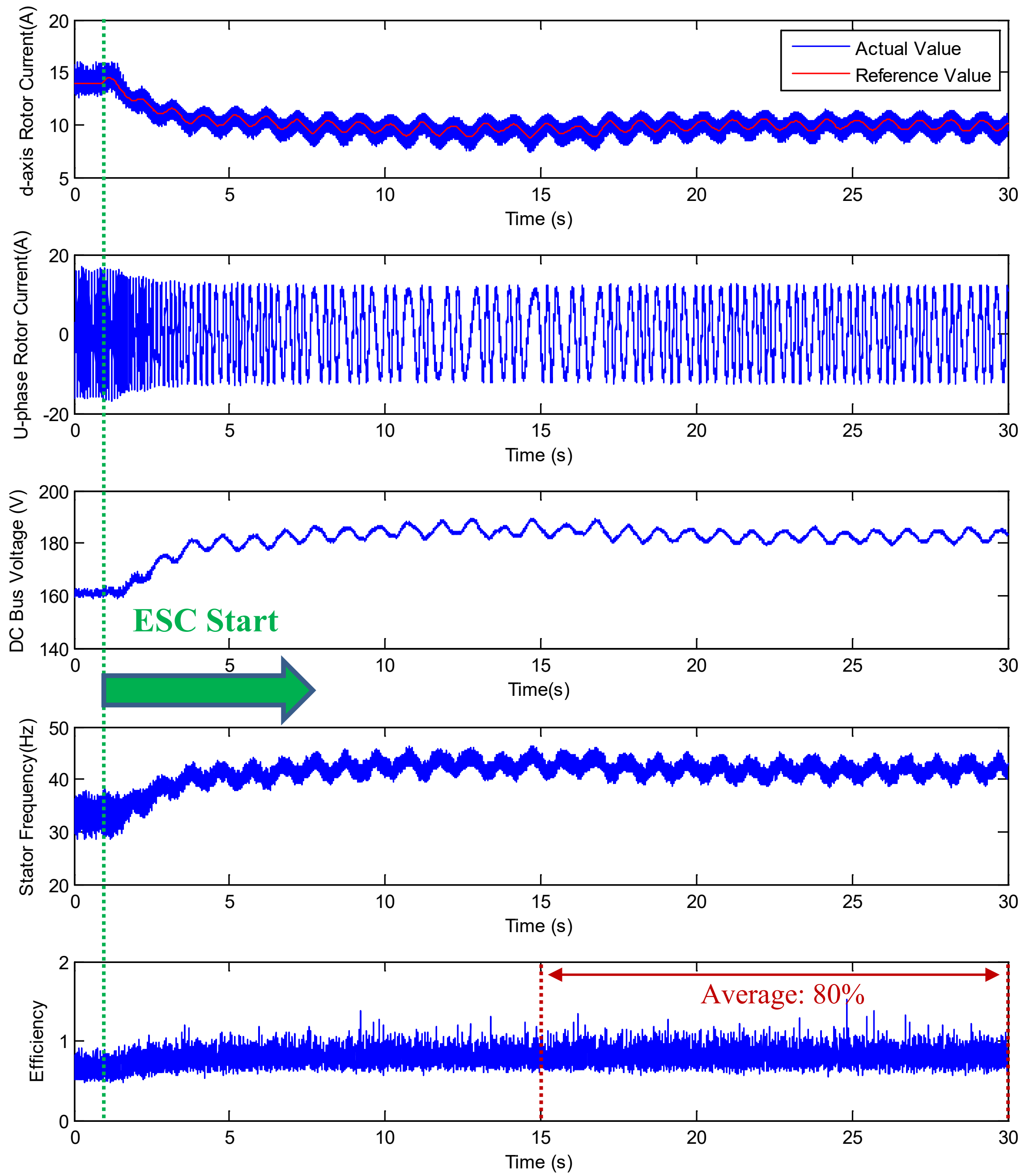

Figure 6.8. ESC test with initial d-axis rotor current of 14 A

The ESC controller is engaged at 1 second, after about 9 seconds, the ESC converged to the optimal working point. Compared with the previous ESC test, the convergence speed is much faster. The difference in the convergence speed is consistent with the performance map shown in the upper plot of Figure 6.6. Since slope on the right side of the optimal working point is steeper than that of the left side. Steeper slope means larger gradient (absolute value). With the same integrator gain, larger gradient generally results in faster convergence speed. From the calculated efficiency plot shown in the bottom subplot of Figure 6.8, an obvious increasing trend can be observed during the ESC searching process. To better evaluate the test results, the average value of the calculated efficiency is obtained based on 15 to 30 second data section. The calculated average efficiency after ESC converged is 80%, which is identical with the calibrated optimum value shown in Table 6.2.

6.6 Summary and Conclusion

For the DFIG-DC system, to generate as much electricity as possible, it is crucial to maximize the efficiency (or minimize the power losses) of the DFIG-DC system. To achieve the objective of minimizing the power losses, existing studies use model-based approach to derive the equation for the optimal control action. However, as discussed in subsection 2 of this chapter, it is very difficult to obtain an accurate power losses model for the studied DFIG-DC system.

In this chapter, as a model-free optimization algorithm, extremum seeking control (ESC) is adopted as the optimal stator frequency controller. Prior to ESC test, performance maps of efficiency under different settings of control input (stator frequency or d-axis rotor current) are obtained as a benchmark for the evaluation of the ESC test. The performance map demonstrates the potential of big improvement in system efficiency compared with the case where stator frequency is simply regulated at the rated value (60 Hz). For the ESC test, both simulation study and experimental study demonstrate that the proposed ESC based optimal stator frequency controller can successfully find the optimal control input that results in the maximum efficiency of the DFIG-DC system.

CHAPTER 7

CONCLUSIONS AND FUTURE RESEARCH

7.1 Conclusions

This dissertation is focused on investigating novel control algorithms with the potential for improving the energy conversion efficiency and the reliability of WECS. The levelized cost of energy of the wind power systems generation can thus be reduced. The dissertation research has involved controls on both aeromechanical and electrical subsystems of WECS operation.

7.1.1 Aeromechanical Subsystem

To increase the overall energy conversion efficiency, it is necessary to increase the power coefficient of wind turbine during Region-2 operation. As a nearly model-free algorithm, ESC can find the optimal control parameters for wind turbine operation, which leads to the maximum power coefficient in real time, without relying on wind measurements. Existing works have demonstrated the effectiveness of ESC based Region-2 control through simulation study, to better evaluate the performance of such control scheme, it is necessary to perform field test on a utility-scale wind turbine. The NREL CART3 ESC field test results presented in Chapter 3 indicate that the ESC controllers can improve the power production by 8% ~ 12% over the baseline controller provided by NREL.

To improve the reliability of the wind power system, another major challenge of ever increasing importance is to reduce fatigue loads of the wind turbine structure. Control strategies those simply aim to maximize the energy capture may lead to excessive fatigue load with only trivial enhancement of power yield. A multi-objective extremum seeking control (MOESC) based

Region-2 controller is proposed in Chapter 4 to increase the energy capture while limiting the increase of structural loads. Simulation study based on the NREL CART3 model indicates that the proposed algorithm can successfully reduce the specified structure load(s) with little to no degradation of energy capture performance.

7.1.2 Electrical Subsystem

To increase the overall energy conversion efficiency, besides the power coefficient which is defined for the aeromechanical energy conversion efficiency, it is also important to increase the efficiency of power conversion at the electrical generator. For the DFIG-DC system interested in this study, both simulation and experimental studies indicate that the efficiency of the DFIG-DC system is a unimodal function of the stator frequency, i.e., the efficiency of the DFIG-DC system is maximized when the DFIG operates at a particular (optimal) stator frequency. Model-based optimal stator frequency control is not viable in practical applications due to the difficulty in obtaining an accurate power losses model. In Chapter 6, an ESC based algorithm for optimization of the stator frequency control is proposed to find the optimal stator frequency in real time such that the energy conversion efficiency of the DFIG-DC system is maximized. The effectiveness of the proposed strategy is validated with both simulation and experimental studies.

For the DFIG-DC system, another research problem of interest is the torque ripple caused by uncontrollable rectification need to be addressed to reduce the structure load. To reduce the torque ripple, the q-axis rotor current needs to track a high-frequency pulsating command. The bandwidth of the PI current controller developed in the traditional single reference frame is inadequate due to the stability requirement. In Chapter 5, a multiple reference frame (MRF) based controller is proposed to improve the current tracking performance, so that the torque ripple could be reduced.

Both simulations and experiments demonstrate that the proposed MRF controller can effectively mitigate the torque ripple in the DFIG-DC system. Also, the robustness against stator frequency deviation is also validated by the simulation and experimental results.

7.2 Recommended Future Research

For the ESC based Region-2 control, it was found out that as the wind speed turbulence intensity increases, the performance of such scheme would deteriorate. The future research could be directed to developing a modified ESC framework which can deliver more consistent performance even with high turbulence intensity level.

For the multi-objective ESC (MOESC) controller which aims to increasing the energy capture while reducing the specified load(s), the recommended future research direction is to incorporate the levelized cost of energy (LCOE) model into the MOESC design. In this case, the performance index for the MOESC controller would be directly correlated with the estimated LCOE.

For the DFIG-DC system, the proposed MRF controller evaluated in this dissertation is designed to reduce the 6^{th}-order harmonic in the torque ripple due to its dominating magnitude. To further reduce the torque ripple, a revised MRF controller could be developed to simultaneously suppress the 12^{th}-order or even higher order torque harmonics as well.

Although the experimental results shown in Chapter 6 demonstrate that the ESC based optimal stator frequency controller can successfully find the optimal stator frequency that results in the highest efficiency, the convergence rate could be improved in future research. Also, it would be of more practical value to evaluate the tracking performance of the ESC based algorithm when the optimal stator frequency is time-varying instead of time-invariant.

Last but not the least, it would be worthwhile to implement the MRF based torque ripple mitigation scheme and the ESC based optimal stator frequency control algorithm simultaneously. This joint implementation would facilitate the study of any coupling between the two controllers. If strong interactions are presented between these two control loops, some unified/centralized/decoupled control strategies should be investigated such that both control objective can be accomplished.

APPENDIX A

PARAMETERS OF THE DFIG

Table A.1. Parameters of the DFIG used for simulation and experimental study

Parameters	Value
Rated power	7457 W
Rated voltage (rotor/stator)	460/195 V
Rated current (rotor/stator)	14.3/26.5 A
Rated speed	1150 rpm
Pole pair number	3
Stator-rotor turns ratio	0.42
R_s	0.2167 Ω
R_r	0.457 Ω
L_{ls}	0.7486 mH
L_{lr}	0.7486 mH
L_m	19.9 mH

APPENDIX B

SIMULINK MODEL OF MRF BASED TORQUE RIPPLE MITIGATION

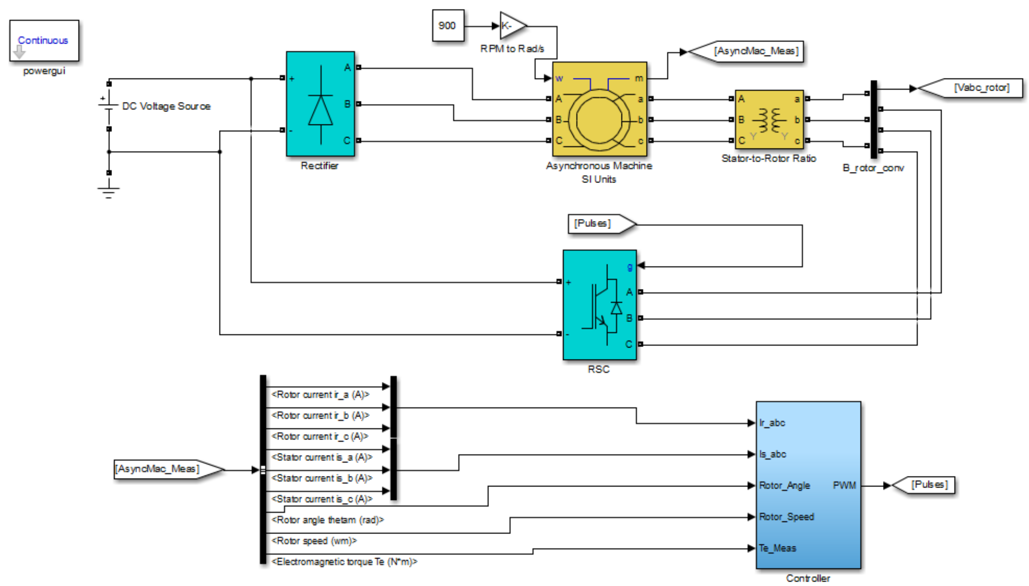

Figure B.1. Simulink layout of the overall system

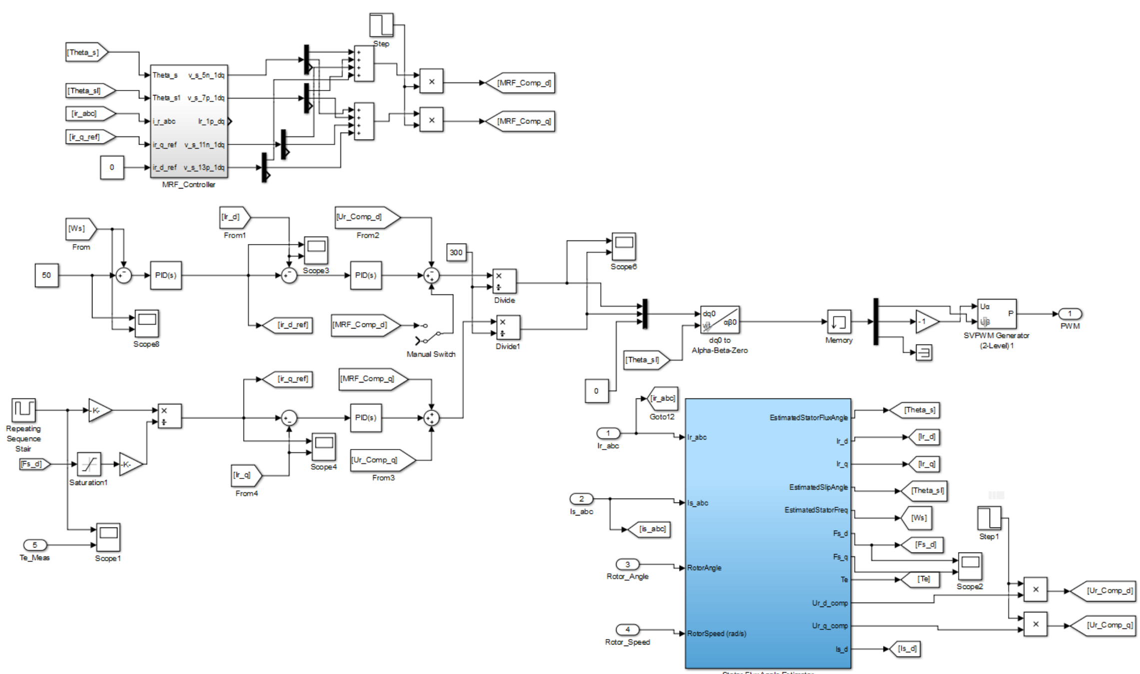

Figure B.2. Simulink layout of the controller

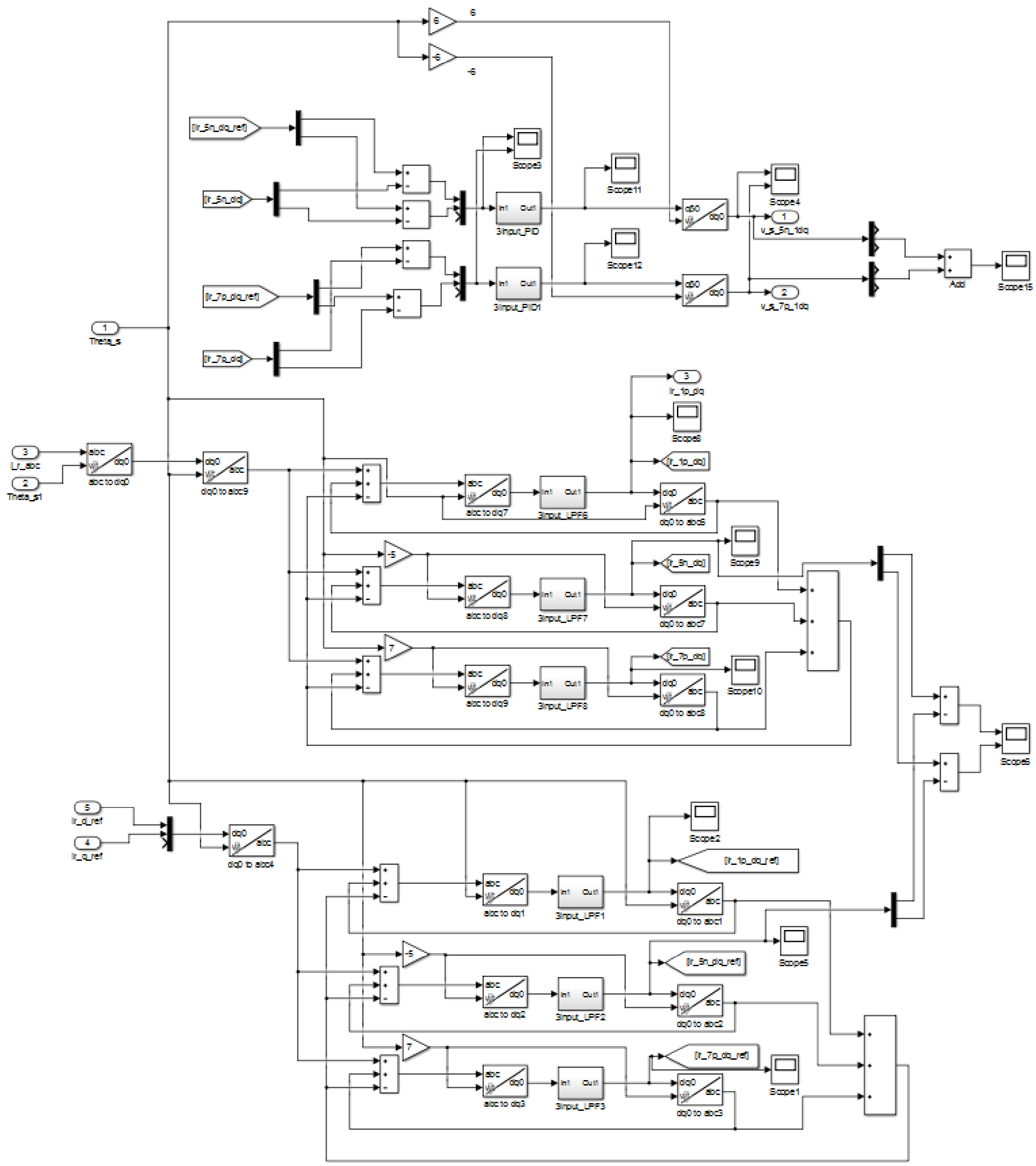

Figure B.3. Simulink layout of the MRF controller

Simulink model parameters:

```
% DFIG Parameter   Note: All the parameters are referred to the stator side
Pn = 7600;
Vn = 460;
fn = 60;
```

```
P = 3;    % pole pair number

Rs = 0.2167;
Rr = 0.4570;

Lls = 0.0007486;
Llr = 0.0007486;
Lm = 0.0199;

Ls = Lls + Lm;
Lr = Llr + Lm;

Sigma = 1-(Lm*Lm)/(Ls*Lr);


% Controller Parameter
Flux_Kp = 1000;
Flux_Ki = 1000;

Ir_d_Kp = 0.473*5;
Ir_d_Ki = 147.04*5;

Ir_q_Kp = 0.473*5;
Ir_q_Ki = 147.04*5;

fs_Kp = 0.5;
fs_Ki = 6.5*5;

Te_Kp = 0.5;
Te_Ki = 6.5*4;

Ge = 500;

MRF_P = 1;
MRF_I = 500;
```

APPENDIX C

LABVIEW PROGRAM CODES FOR EXPERIMENTAL STUDY OF MRF BASED TORQUE RIPPLE MITIGATION

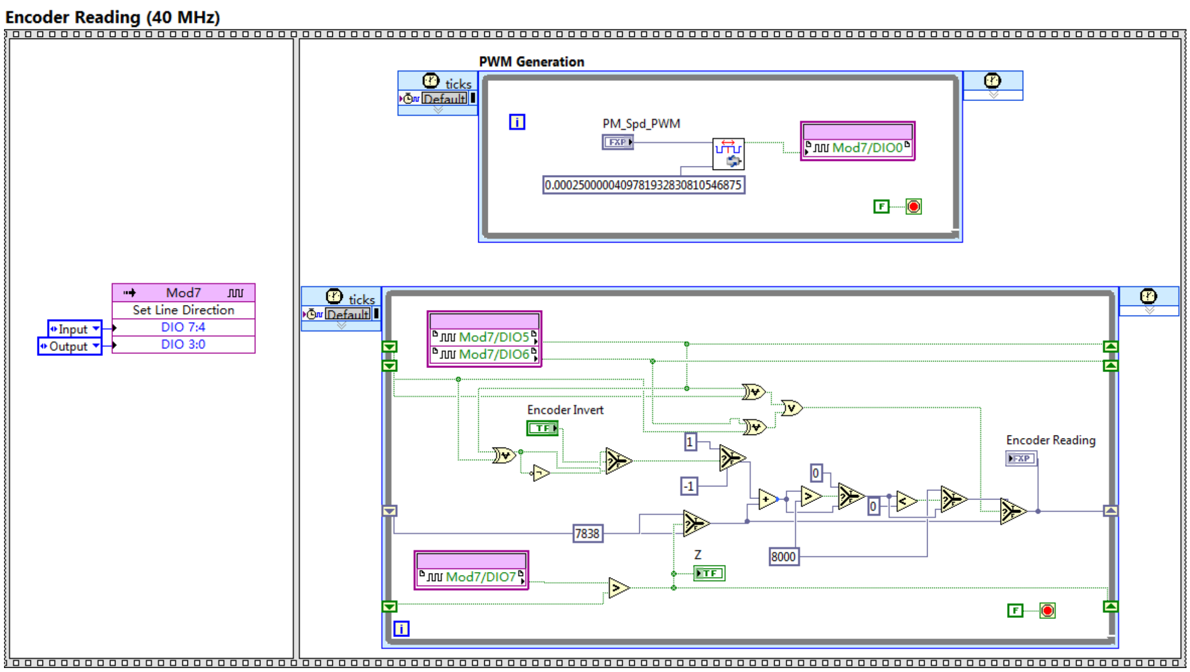

Figure C.1. Labview code for encoder reading and PMW output for prime mover speed command (FPGA target)

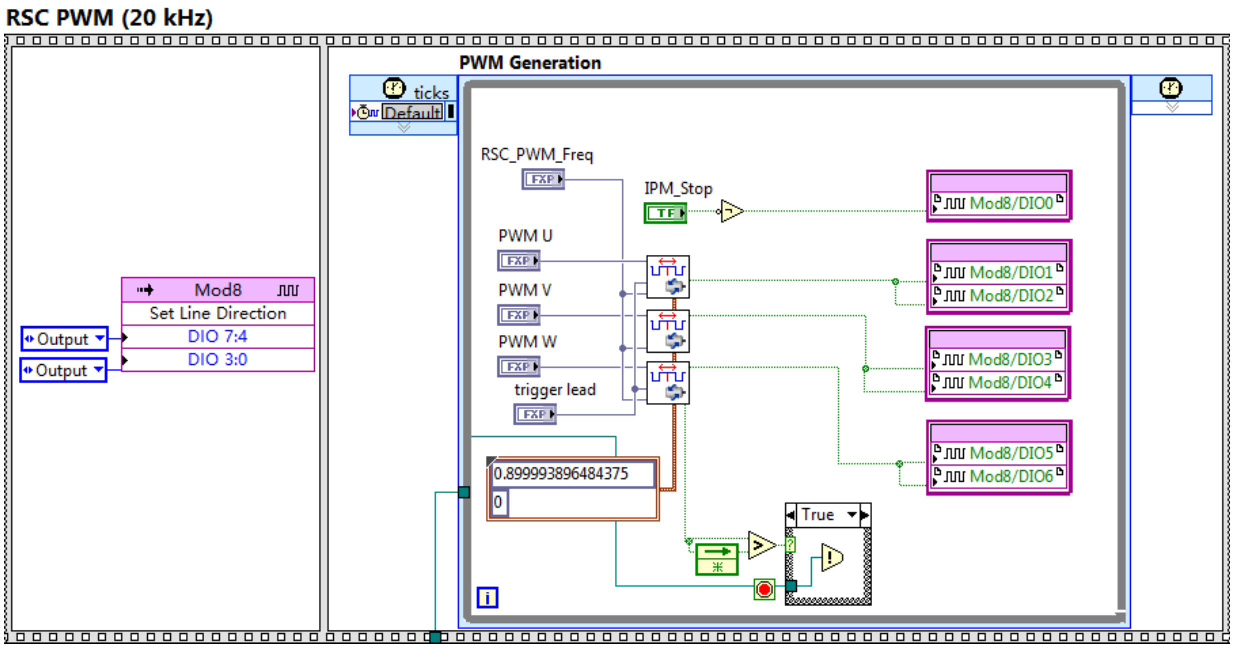

Figure C.2. Labview code for rotor side converter PWM generator (FPGA target)

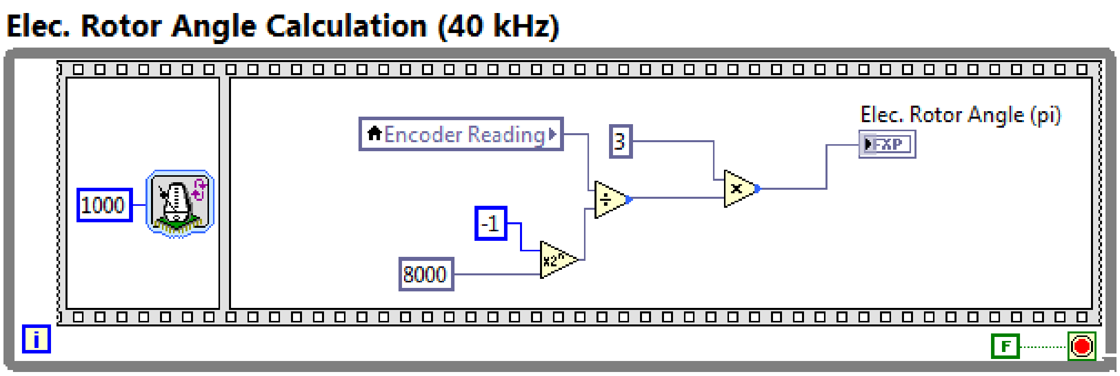

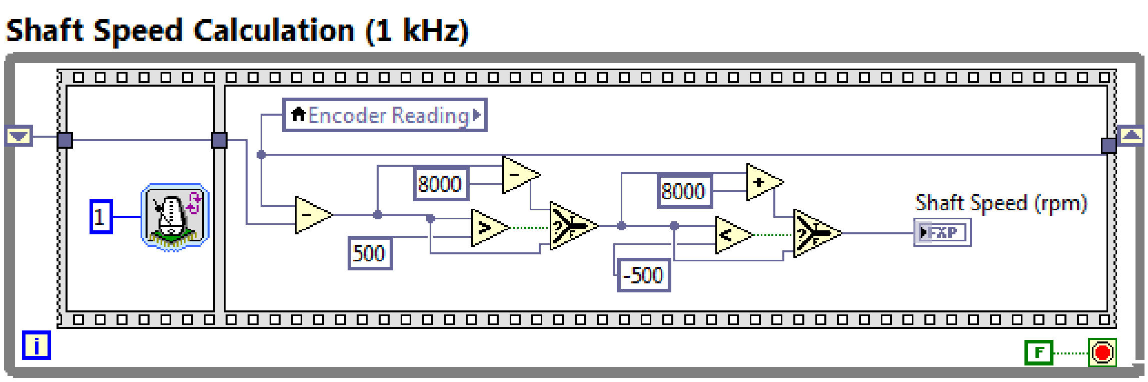

Figure C.3. Labview code for electrical rotor angle calculation and rotor shaft speed calculation (FPGA target)

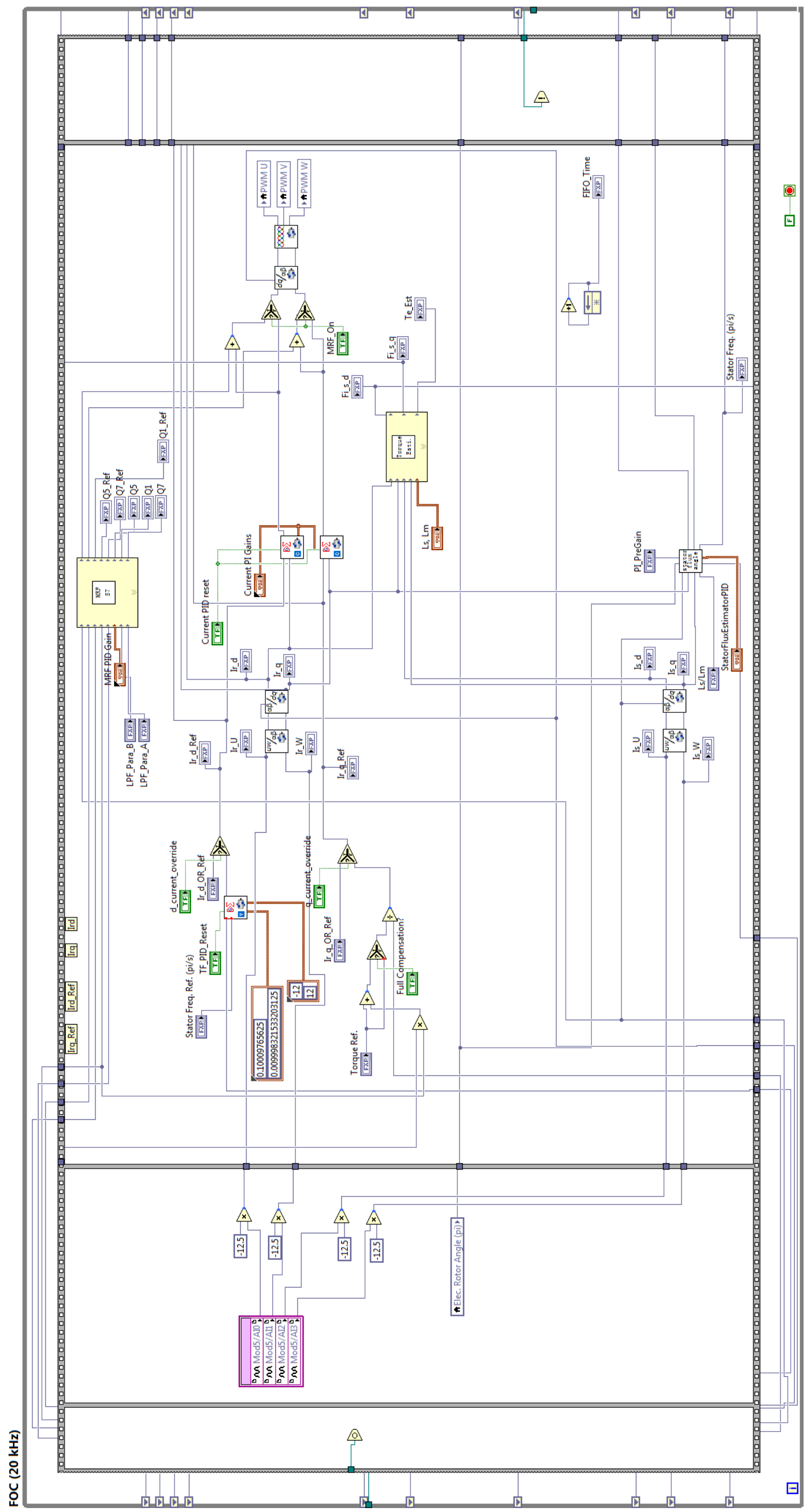

Figure C.4. Labview code for FOC of the DFIG (FPGA target)

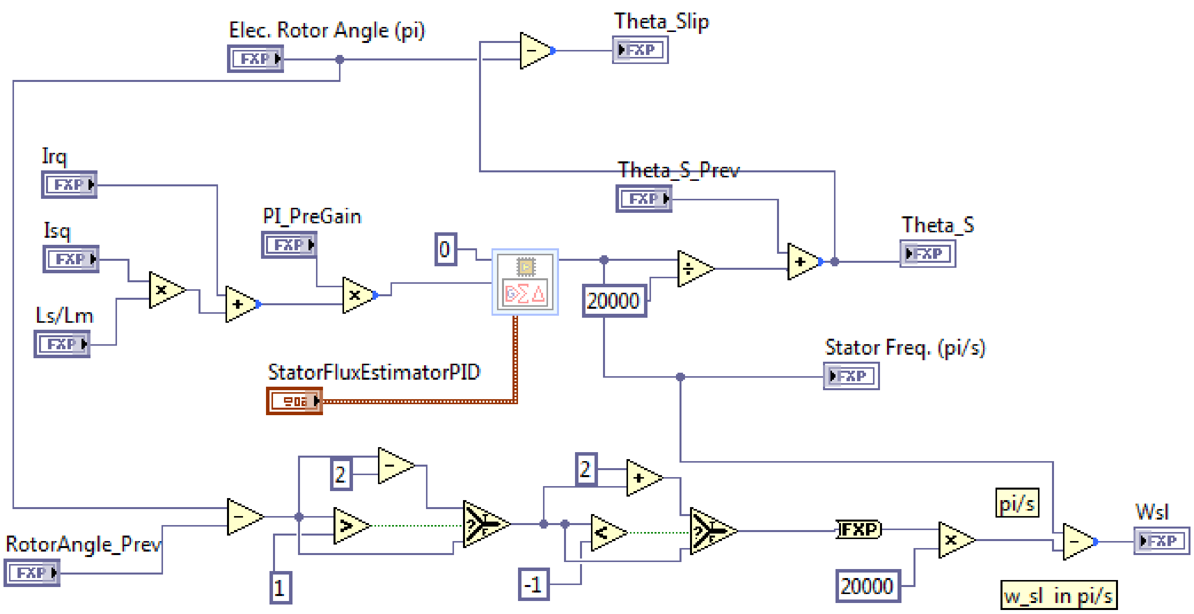

Figure C.5. Labview code for stator flux angle estimation (FPGA target)

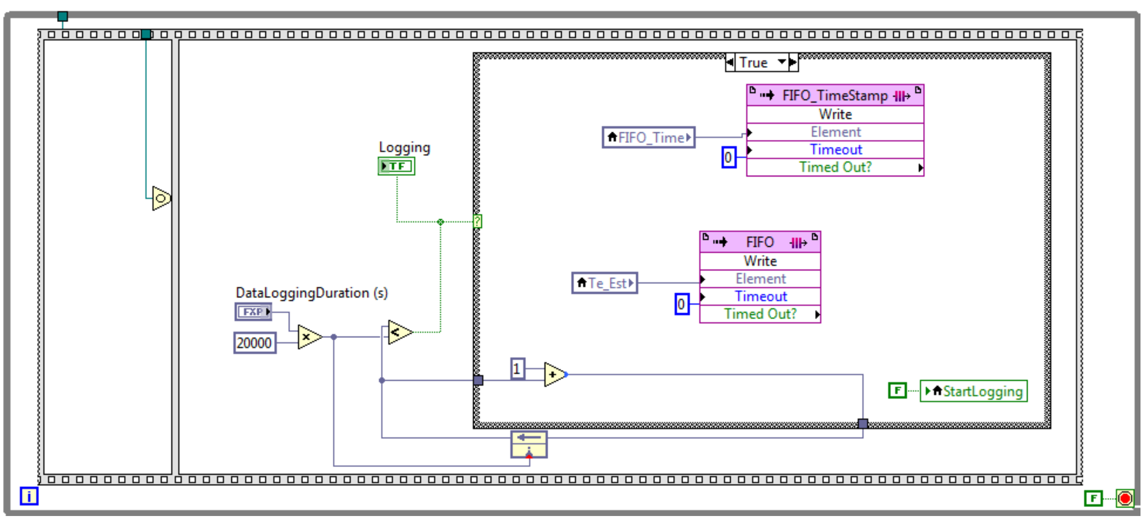

Figure C.6. Labview code for data logging (FPGA target)

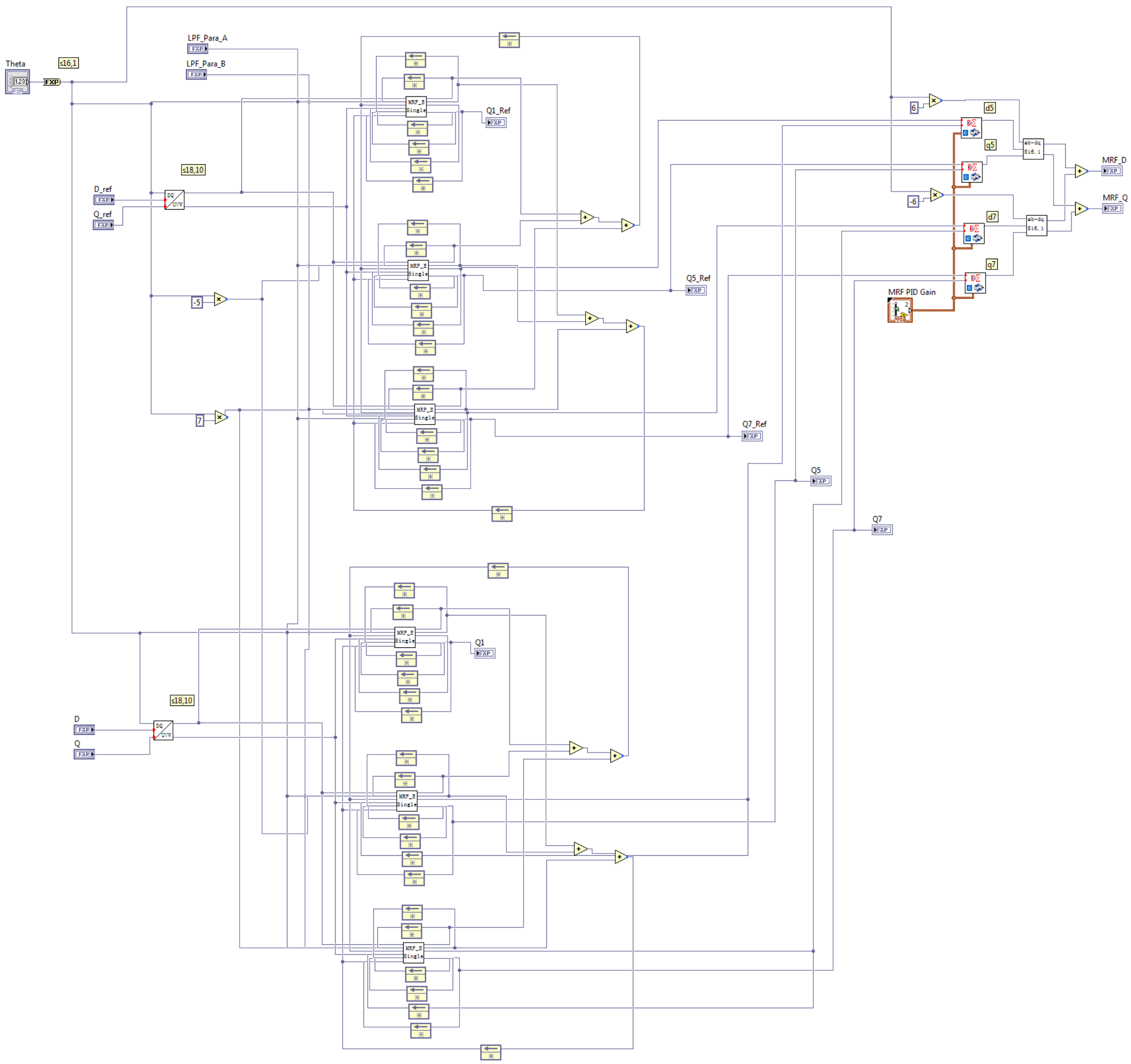

Figure C.7. Labview code for MRF controller (FPGA target)

APPENDIX D

SIMULINK MODEL OF ESC BASED OPTIMAL STATOR FREQUENCY CONTROL

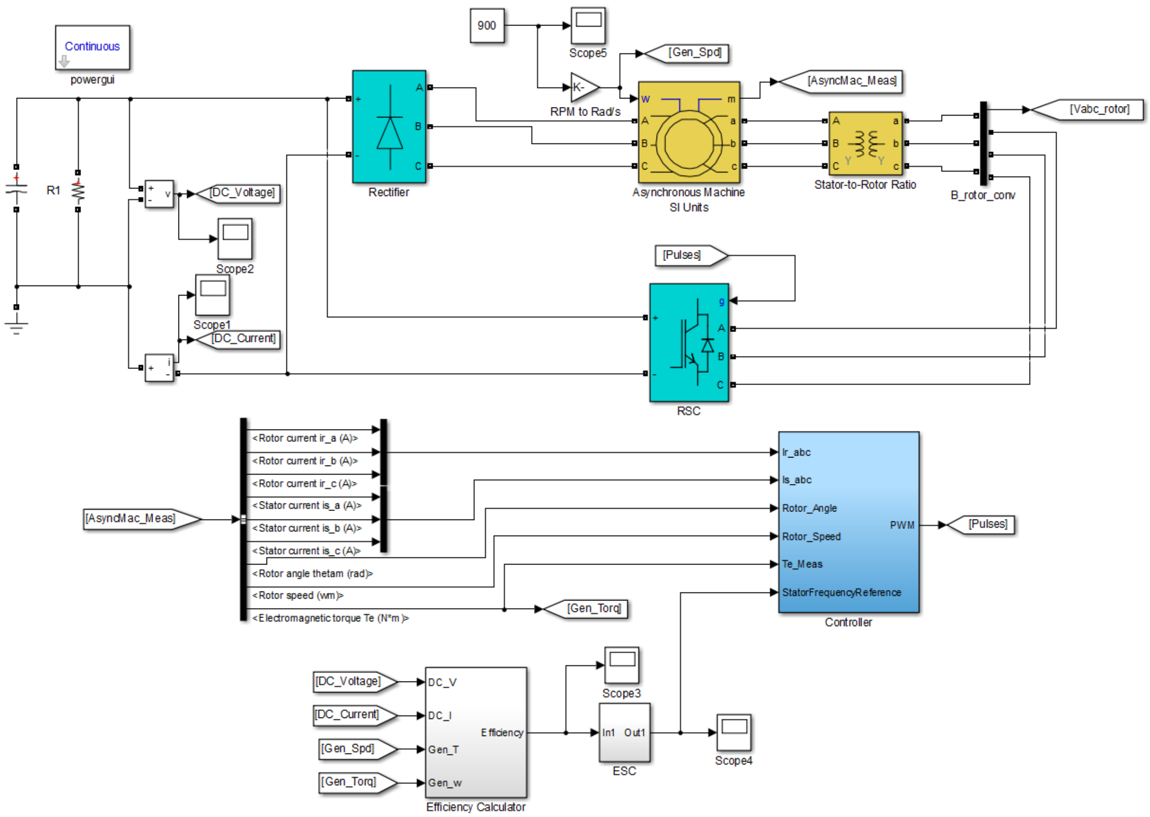

Figure D.1. Simulink layout of the overall system

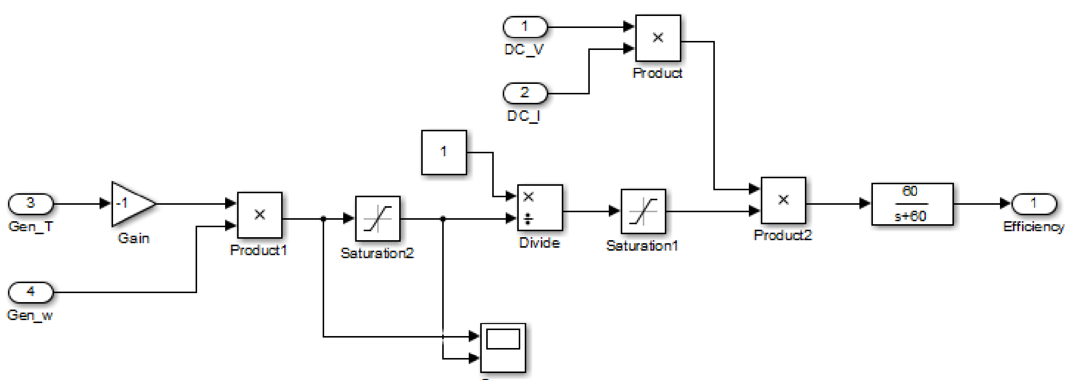

Figure D.2. Simulink layout of the efficiency estimator

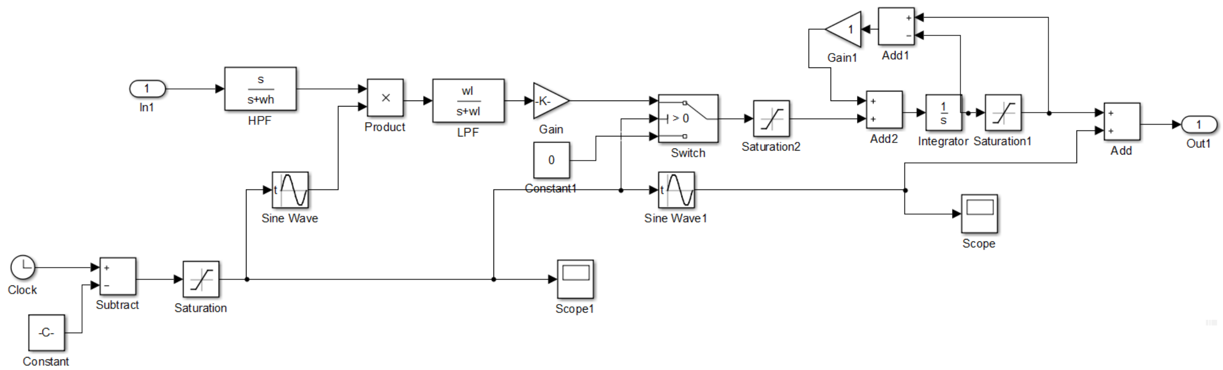

Figure D.3. Simulink layout of the ESC controller

APPENDIX E

LABVIEW PROGRAM CODES FOR EXPERIMENTAL STUDY OF ESC BASED OPTIMAL STATOR FREQUENCY CONTROL

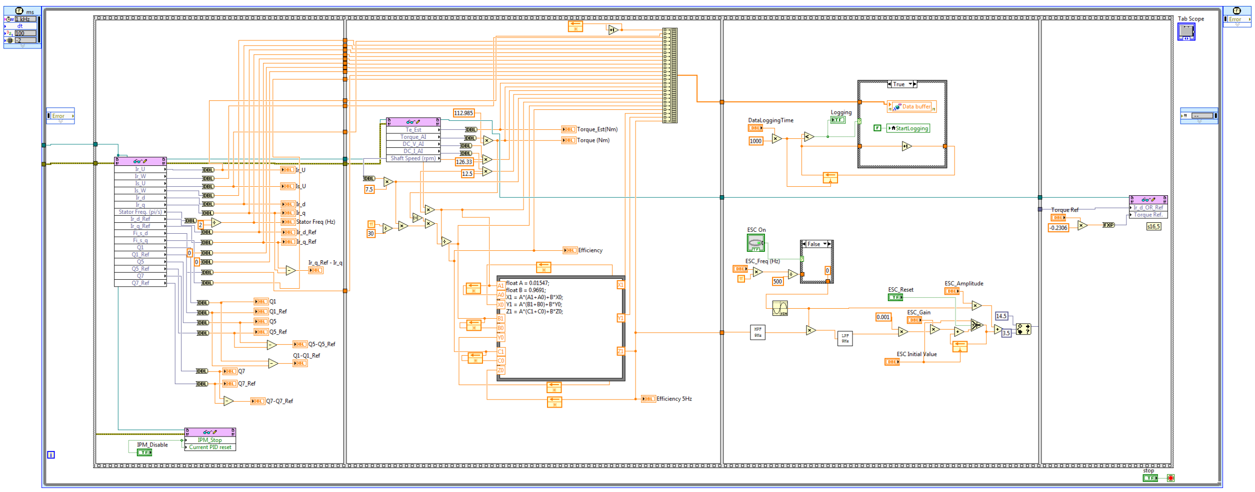

Figure E.1. Labview code for the efficiency estimator and ESC controller (RT controller target)

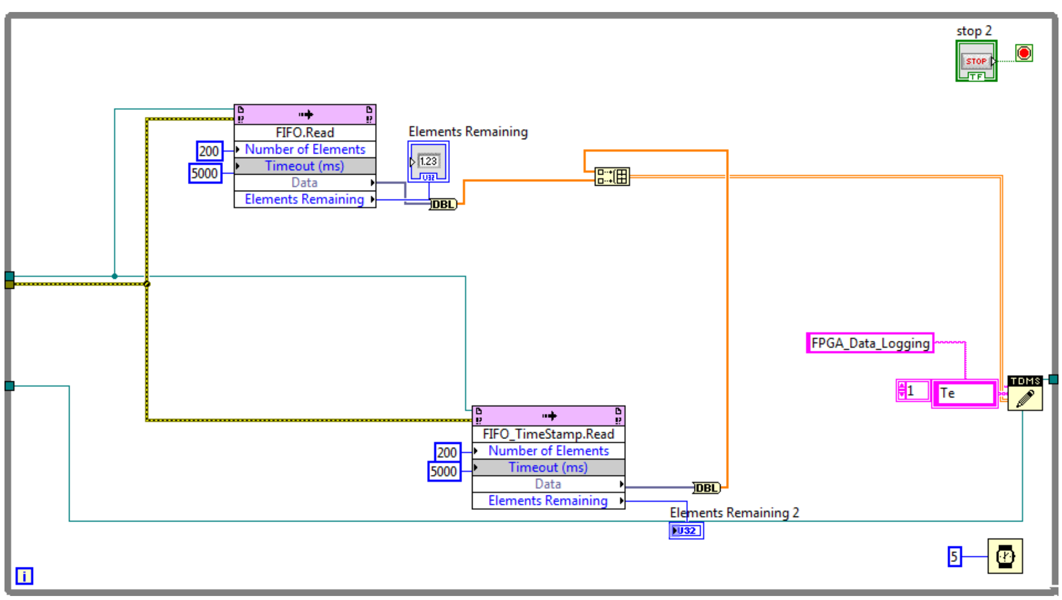

Figure E.2. Labview code for FPGA data logging (RT controller target)

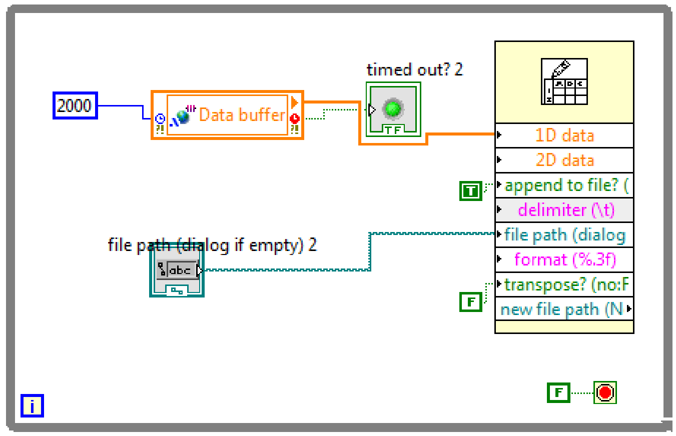

Figure E.3. Labview code for RT controller data logging (RT controller target)

Note: The Labview codes for the FPGA target are the same with the ones shown in Appendix C.

REFERENCES

[1] U.S. Energy Information Administration, *International Energy Outlook 2016*, Washington DC, 2016.

[2] Shell, *World Energy Model: A View to 2100*, 2017.

[3] U.S. Department of Energy, *Wind Vision: A New Era for Wind Power in the United States*, 2015.

[4] International Energy Agency, *Technology Roadmap: China Wind Energy Development Roadmap 2050*, 2011.

[5] Wikimedia Commons. [Online]. Available: https://commons.wikimedia.org/wiki/File: Wind_turbine_with_observation_deck_bruck_an_der_leitha.jpg, Accessed on July 31, 2018.

[6] Wikimedia Commons. [Online]. Available: https://commons.wikimedia.org/wiki/File: Darrieus_rotor002.jpg, Accessed on July 31, 2018.

[7] Office of Energy Efficiency and Renewable Energy. [Online]. Available: https:// energy.gov/eere/wind/how-do-wind-turbines-work , Accessed on Jan. 10, 2018.

[8] F. Blaabjerg, Z. Chen and S. B. Kjaer, “Power electronics as efficient interface in dispersed power generation systems”, in *IEEE Transactions on Power Electronics*, vol. 19, no. 5, pp. 1184-1194, Sept. 2004.

[9] M. F. Iacchetti, G. D. Marques and R. Perini, "Torque ripple reduction in a DFIG-DC system by resonant current controllers," in *IEEE Transactions on Power Electronics*, vol. 30, no. 8, pp. 4244-4254, Aug. 2015.

[10] M. F. Iacchetti, G. D. Marques and R. Perini, "A scheme for the power control in a DFIG connected to a DC bus via a diode rectifier," in *IEEE Transactions on Power Electronics*, vol. 30, no. 3, pp. 1286-1296, March 2015.

[11] G. D. Marques and M. F. Iacchetti, "Stator frequency regulation in a field-oriented controlled DFIG connected to a DC link," in *IEEE Transactions on Industrial Electronics*, vol. 61, no. 11, pp. 5930-5939, Nov. 2014.

[12] M. Leblanc, "Sur L'électrification Des Chemins De Fer Au Moyen De Courants Alternatifs De Frequence Elevee," *Revue Generale de l'Electricite*, France, 1922.

[13] C.S. Drapper and Y.T. Li, “Principles of optimizing control systems and an application to the internal combustion engine”, *ASME*, 1951.

[14] L. Frey, W.B. Deem and R.J. Altpeter, "Stability and optimal gain in extremum seeking adaptive control of a gas furnace," *Third IFAC World Congress*, 48A, London, British, 1966.

[15] M. Krstić, H.H. Wang, "Stability of extremum seeking feedback for general nonlinear dynamic systems," *Automatica*, 36, pp. 595-601, 2000.

[16] M.A. Rotea, "Analysis of multivariable extremum seeking algorithm," *American Control Conference*, Chicago, IL, 1(6), pp. 433-437, Sept. 2000.

[17] K.B. Ariyur, M. Krstić, *Real Time Optimization by Extremum Seeking Control*. Wiley, Hoboken, NJ, 2003.

[18] P. Li, Y. Li and J. E. Seem, "Extremum seeking control for efficient and reliable operation of air-side economizers," *2009 American Control Conference*, St. Louis, MO, 2009, pp. 20-25.

[19] L. Dong, Y. Li, B. Mu, Y. Xiao, "Self-optimizing control of air-source heat pump with multivariable extremum seeking", *Applied Thermal Engineering*, vol. 84, no. 5, pp. 180-195, June 2015.

[20] B. Mu, Y. Li, J. E. Seem, B. Hu, "A multivariable Newton-based extremum seeking control for condenser water loop optimization of chilled-water plant". *ASME. J. Dyn. Sys., Meas., Control*, vol. 137, no. DS-14-1449, pp. 111011/1-10, Aug. 2015.

[21] D. Burns and C. R. Laughman. "Extremum seeking control for energy optimization of vapor compression systems," *(2012) International Refrigeration and Air Conditioning Conference*. Paper #1207.

[22] Y. Xiao, Y. Li and J. E. Seem, "Multi-variable extremum seeking control for mini-split air-conditioning system," Paper #2508, *Proceedings of the 15th International Refrigeration and Air Conditioning Conference* at Purdue, July 14-17, 2014, Purdue University, West Lafayette, IN, USA.

[23] R. Leyva, C. Alonso, I. Queinnec, A. Cid-Pastor, D. Lagrange and L. Martinez-Salamero, "MPPT of photovoltaic systems using extremum - seeking control," in *IEEE Transactions on Aerospace and Electronic Systems*, vol. 42, no. 1, pp. 249-258, Jan. 2006.

[24] Yamanaka, Osamu & Onishi, Yuuta & Namba, Ryo & Obara, Takumi & Hiraoka, Yukio. (2017). "A total cost minimization control for wastewater treatment process by using extremum seeking control," *Water Practice and Technology*. vol. 12, no. 4, pp. 751-760, Dec. 2017.

[25] D. Tehrani, F. Shabani, "Performance improvement of fuel cells using perturbation-based extremum seeking and model reference adaptive control", *Asian Journal of Control*, vol. 19, no, 6, pp. 2178-2191, 2017.

[26] A. S. Matveev, M. C. Hoy, and A. V. Savkin, “3D environmental extremum seeking navigation of a nonholonomic mobile robot”, *Automatica*, vol. 50, no. 7, pp. 1802-1815, July 2014.

[27] E. Dinçmen, B. A. Güvenç and T. Acarman, "Extremum-seeking control of ABS braking in road vehicles with lateral force improvement," in *IEEE Transactions on Control Systems Technology*, vol. 22, no. 1, pp. 230-237, Jan. 2014.

[28] S. L. Brunton, X. Fu and J. N. Kutz, "Extremum-seeking control of a mode-locked laser," in *IEEE Journal of Quantum Electronics*, vol. 49, no. 10, pp. 852-861, Oct. 2013.

[29] M. Guay, D. Dochain, M. Perrier, “Adaptive extremum seeking control of continuous stirred tank bioreactors with unknown growth kinetics”, In *Automatica*, vol. 40, no. 5, pp. 881-888, 2004.

[30] J. Creaby, Y. Li and J. E. Seem, “Maximizing wind turbine energy capture using multivariable extremum seeking control”, *Wind Engineering*, vol. 33, no. 4, pp.361-387, Jun. 2009.

[31] Z. Yang, Y. Li and J. E. Seem, “Optimizing energy capture of cascaded wind turbine array with nested-loop extremum seeking control”, *ASME. J. Dyn. Sys., Meas., Control*, vol. 137, no. DS-14-1398, pp. 121010/1-9, Oct. 2015.

[32] L.Y. Pao and K.E. Johnson, “Control of wind turbines: approaches, challenges, and recent developments,” *IEEE Control Systems Magazine*, vol. 31, no. 2, pp. 44-62, April 2011.

[33] M. A. Bratcu, N. A. Cutululis and E. Ceanga, *Optimal Control of Wind Energy Systems: Towards a Global Approach*, Springer, 2008.

[34] F.D. Bianchi, H. de Battista, and R.J. Mantz, *Wind Turbine Control Systems: Principles, Modeling and Gain Scheduling Design*, Springer, 2006.

[35] L. Y. Pao and K. E. Johnson, “A tutorial on the dynamics and control of wind turbines and wind farms”, in *Proc. of American Control Conference*, St. Louis, MO, USA, Jun. 2009.

[36] M. A. Abdullah, A. H. M. Yatim, C. W. Tan, and R. Saidur, “A review of maximum power point tracking algorithms for wind energy systems,” *Ren. & Sus. Energy Reviews*, vol. 16, pp. 3220-3227, 2012.

[37] S. M. R. Kazmi, H. Goto, H. Guo., and O. Ichinokura, “Review and critical analysis of the research papers published till date on maximum power point tracking in wind energy conversion system,” in *2010 IEEE Energy Conv. Congress & Expo. (ECCE)*. 2010. pp. 4075-4082.

[38] K. Z. Ostergaard, P. Brath, and J. Stoustrup, "Gain-scheduled linear quadratic control of wind turbines operating at high wind speed," in *16th IEEE Int. Conf. Control Applications*, Singapore, 2007, pp. 276-281.

[39] M. Soliman, O. P. Malik, and D. T. Westwick, "Multiple model predictive control for wind turbines with doubly fed induction generators," *IEEE Trans. Sus. Energy*, vol. 2, no. 3, pp. 215-225, Jul. 2011.

[40] T. Bakka, H. R. Karimi, and S. Christiansen, "Linear parameter-varying modeling and control of an offshore wind turbine with constrained information," *IET Ctrl. Theory & App.*, vol. 8, no. 1, pp. 22-29, 2014.

[41] K.E. Johnson, L.J. Fingersh., M. J. Balas, and L. Y. Pao, "Methods for increasing region 2 power capture on a variable-speed wind turbine", *Journal of Solar Energy Engineering*, vol. 126, no. 4, pp. 1092-1100, 2004.

[42] K. E. Johnson, L. Y. Pao, M. J. Balas and L. J. Fingersh, "Control of variable speed wind turbines: standard and adaptive techniques for maximizing energy capture," *IEEE Control Systems Magazine*, vol. 26, no. 3, pp. 70-81, June 2006.

[43] K.B. Ariyur and M. Krstić, *Real-time Optimization by Extremum-Seeking Control*, John Wiley & Sons, 2003.

[44] C. Zhang and R. Ordez, *Extremum-seeking Control and Applications: A Numerical Optimization-based Approach*, Springer, 2012.

[45] M. Komatsu, H. Miyamoto, H. Ohmori, and A. Sano, "Output maximization control of wind turbine based on extremum control strategy," in *Proc. 2001 Am. Ctrl Conf.*, Arlington, VA, Jun. 2001, pp. 1739 - 1740.

[46] C. Ishii, H. Hashimoto, and H. Ohmori, "Modeling of variable pitch micro wind turbine and its output optimization control with adaptive extremum control scheme," *Trans. of the Japan Society of Mechanical Engineers*, Part C, vol. 69, no. 11, pp. 3034-3040, 2003.

[47] K. E. Johnson and G. Fritsch, "Assessment of extremum seeking control for wind farm energy production," *Wind Engr.*, vo. 36, no. 6, pp. 701-716, 2012.

[48] P.A. Fleming, J.W. van Wingerden and A.D. Wright, "Comparing state-space multivariable controls to multi-SISO controls for load reduction of drivetrain-coupled modes on wind turbines through field-testing," *National Renewable Energy Lab.*, NREL/CP-5000-53500, Dec. 2011.

[49] Y. Xiao, Y. Li, and M. A. Rotea, "Experimental evaluation of extremum seeking based region-2 controller for CART3 wind turbine," in *AIAA 2016 Sci-Tech Wind Energy Symposium*, San Diego, CA, Jan. 2016, Paper No. AIAA 2016-1737.

[50] L. Fan, S. Yuvarajan, and R. Kavasseri, “Harmonics analysis of a DFIG for a wind energy conversion system,” *IEEE Trans. Energy Convers.*, vol. 25, no. 1, pp. 181-190, Mar. 2010.

[51] J. Hu, H. Nian, H. Xu, and Y. He, “Dynamic modeling and improved control of DFIG under distorted grid voltage conditions,” *IEEE Trans. Energy Convers.*, vol. 26, no. 1, pp. 163-175, Mar. 2011.

[52] R. D. Shukla, R. K. Tripathi, and P. Thakur, “DC grid/bus tied DFIG based wind energy system,” *Renewable Energy*, vol. 108, pp. 179-193, 2017.

[53] G. D. Marques and M. F. Iacchetti, “Inner control method and frequency regulation of a DFIG connected to a dc link,” *IEEE Trans. Energy Convers*., vol. 29, no. 2, pp. 435-444, Jun. 2014.

[54] A. Petersson, L. Harnefors, and T.Thiringer, “Evaluation of current control methods for wind turbines using doubly-fed induction machines,” *IEEE Trans. Power Electron*., vol. 20, no. 1, pp. 227-235, Jan. 2005.

[55] G. D. Marques and D. M. Sousa, "Stator flux active damping methods for field-oriented doubly fed induction generator," in *IEEE Transactions on Energy Conversion*, vol. 27, no. 3, pp. 799-806, Sept. 2012.

[56] J. Liang, D. F. Howard, J. A. Restrepo, and R. G. Harley, “Feedforward transient compensation control for DFIG wind turbines during both balanced and unbalanced grid disturbances,” *IEEE Trans. Ind. Appl.*, vol. 49, no. 3, pp. 1452-1463, May/Jun. 2013.

[57] M. F. Iacchetti and G. D. Marques, "Enhanced torque control in a DFIG connected to a DC grid by a diode rectifier," *2014 16th European Conference on Power Electronics and Applications*, Lappeenranta, 2014, pp. 1-9.

[58] H. Nian, C. Wu and P. Cheng, "Direct resonant control strategy for torque ripple mitigation of DFIG connected to DC link through diode rectifier on stator," in *IEEE Transactions on Power Electronics*, vol. 32, no. 9, pp. 6936-6945, Sept. 2017.

[59] G. D. Marques and M. F. Iacchetti, "Minimization of torque ripple in the DFIG-DC system via predictive delay compensation," in *IEEE Transactions on Industrial Electronics*, vol. 65, no. 1, pp. 103-113, Jan. 2018.

[60] N. Yu, H. Nian, and Y. Quan, “A novel dc grid connected DFIG system with active power filter based on predictive current control,” in *Proc. Int. Conf. Electr. Mach. Syst.*, Aug. 2011, pp. 1-5.

[61] C. Wu and H. Nian, "An improved repetitive control of DFIG-DC system for torque ripple suppression," in *IEEE Transactions on Power Electronics*, vol. 33, no. 9, pp. 7634-7644, Sept. 2018.

[62] C. Liu, F. Blaabjerg, W. Chen and D. Xu, "Stator current harmonic control with resonant controller for doubly fed induction generator," in *IEEE Transactions on Power Electronics*, vol. 27, no. 7, pp. 3207-3220, July 2012.

[63] G. D. Marques and M. F. Iacchetti, "A self-sensing stator-current-based control system of a DFIG connected to a DC-Link," in *IEEE Transactions on Industrial Electronics*, vol. 62, no. 10, pp. 6140-6150, Oct. 2015.

[64] G. D. Marques and M. F. Iacchetti, "Sensorless frequency and voltage control in the stand-alone DFIG-DC system," in *IEEE Transactions on Industrial Electronics*, vol. 64, no. 3, pp. 1949-1957, March 2017.

[65] G. D. Marques and M. F. Iacchetti, "Field-weakening control for efficiency optimization in a DFIG connected to a DC-Link," in *IEEE Transactions on Industrial Electronics*, vol. 63, no. 6, pp. 3409-3419, June 2016.

[66] M. L. Buhl, “WT_PERF User’s Guide”, National Renewable Energy Laboratory, Golden, Colorado, Dec. 17, 2004.

[67] J. F. Manwell, J. G. McGowan, and A. L. Rogers, *Wind Energy Explained: Theory, Design and Application*, 2nd Ed., Wiley, 2009.

[68] D. Alciatore and M. Histand, *Introduction to Mechatronics and Measurement Systems*, 3rd Ed., McGraw-Hill, 2007.

[69] E. Bossanyi, A. Wright, P. Fleming, “Controller field tests on the NREL CART3 turbine,” National Renewable Energy Laboratory, NREL/TP-5000-49085, Dec. 2010.

[70] R. Osgood, G. Bir, H. Mutha, B. Peeters, M. Luczak, and G. Sablon, “Full-scale modal wind turbine tests: comparing shaker excitation with wind excitation”, in *Conf. Proc. Society for Experimental Mechanics Series*, Jacksonville FL., Feb. 2011, pp.113-124.

[71] D. Wright and L. J. Fingersh, “Advanced control design for wind turbines part 1: control design, implementation, and initial tests”, National Renewable Energy Laboratory, NREL/TP-500-42437, Mar. 2008.

[72] D. Schlipf, P. Fleming, S. Raach, A. Scholbrock, F. Haizmann, R. Krishnamurthy, M. Boquet, and P.W. Cheng, “An adaptive data processing technique for Lidar-assisted control to bridge the gap between Lidar system and wind turbines”, in *European Wind Energy Association Annual Event (EWEA)*, Paris, France, Nov. 2015.

[73] A. Scholbrock, personal communication, National Renewable Energy Laboratory, Golden, Colorado, 2015.

[74] Google Maps. [Online]. Available: https://www.google.com/maps/, Accessed on Sep. 23, 2015.

[75] K.E. Johnson, *Adaptive Torque Control of Variable Speed Wind Turbines*, NREL/TP-500-36265, National Ren. Energy Lab., August 2004.

[76] M. L. Buhl, “MCrunch User’s Guide for Version 1.00”, National Renewable Energy Laboratory, Golden, Colorado, May 15, 2008.

[77] A. Ghaffari, M. Krstić, and D. Nesic, “Multivariable newton-based extremum seeking,” *Automatica*, vol. 48, pp. 1759-1767, 2012.

[78] M. Krstić, “Performance improvement and limitations in extremum seeking control,” *Systems & Control Letters*, vol. 39, no.5, pp. 313–326, 2000.

[79] K. E. Johnson, L. J. Fingersh, and A. Wright, “Controls advanced research turbine: lessons learned during advanced controls testing”, Technical Report NREL/TP-500-38130, June 2005.

[80] J. M. Jonkman, M. L. Buhl Jr., “FAST user’s guide,” NREL/EL-500-29798. Golden, Colorado: National Renewable Energy Laboratory, 2005.

[81] P. L. Chapman and S. D. Sudhoff, "A multiple reference frame synchronous estimator/regulator," in *IEEE Transactions on Energy Conversion*, vol. 15, no. 2, pp. 197-202, Jun 2000.

[82] J. A. M. Bleijs, "Continuous conduction mode operation of three-phase diode bridge rectifier with constant load voltage," in *IEEE Proceedings - Electric Power Applications*, vol. 152, no. 2, pp. 359-368, March 2005.

[83] S. M. A. Cruz, G. D. Marques, P. F. d. C. Goncalves and M. F. Iacchetti, "Predictive torque and rotor flux control of a DFIG-DC system for torque-ripple compensation and loss minimization," in *IEEE Transactions on Industrial Electronics*, vol. 65, no. 12, pp. 9301-9310, Dec. 2018.

[84] P. C. Krause, "Method of multiple reference frames applied to the analysis of symmetrical induction machinery," in *IEEE Transactions on Power Apparatus and Systems*, vol. PAS-87, no. 1, pp. 218-227, Jan. 1968.

[85] S. M. Muyeen, *Wind Energy Conversion Systems: Technology and Trends*. London UK: Springer-Verlag London, 2012.

[86] S. Muller, M. Deicke and R. W. De Doncker, “Doubly fed induction generator systems for wind turbines,” IEEE Ind. Appl. Mag., vol. 8, no. 3, pp.26-33, May/Jun. 2002.

[87] A. Scholbrock, personal communication, National Renewable Energy Laboratory, Golden, Colorado, 2018.

[88] Y. Xiao, Y. Li and M. A. Rotea, "CART3 field tests for wind turbine region-2 operation with extremum seeking controllers," in *IEEE Transactions on Control Systems Technology*. vol. PP, no. 99, pp. 1-9, April 2018.

[89] Y. Xiao, Y. Li and M. A. Rotea, “Multi-objective extremum seeking control for enhancement of wind turbine power capture with load reduction,” *Journal of Physics: Conference Series* 753 (2016).

[90] Y. Xiao, Y. Li, M. A. Rotea and B. Fahimi, “ESC based optimal stator frequency control of DFIG-DC system for efficiency enhancement,” 2018 IEEE Energy Conversion Congress and Exposition, September 23 – 27, 2018, Portland, OR, USA.

BIOGRAPHICAL SKETCH

Yan Xiao was born in Henan, China. He received a Bachelor of Science degree in Electrical Engineering from Huazhong University of Science and Technology (HUST), Wuhan, China in 2009. He received his Master of Science degree in Electrical Engineering from Huazhong University of Science and Technology (HUST), Wuhan, China in 2012. Since August 2012, he has been a PhD student in Electrical Engineering at The University of Texas at Dallas. His research interests include motor control, power electronics, and optimal control of renewable energy systems.

CURRICULUM VITAE

Yan Xiao

Address: W. 800 Campbell Rd., Richardson TX 75080, USA

Email: yxx123430@utdallas.edu

SUMMARY

Nine years of experience in motor control system, power electronics system and embedded system analysis, design and development. As well as design and implementation of optimum control algorithm on air-conditioning system and renewable energy system (PV, wind turbine). Strong programming skills, especially in C, C++ and Python.

SKILLS

- Advanced PMSM (FOC control, sensor-less control, direct-torque control, field weakening control, MTPA, etc.), DFIG and BLDC control system design and development
- Power electronics converter (Buck, Boost, Fly-back, Three-phase Inverter, etc.) design and development
- Optimum control (extremum seeking control, model predictive control, dynamic programming)
- Programming languages: ASM, C, C++, Python, Labview
- Development platform: TI DSP (TMS320F28xxx), Infineon MCU (16-bit, 32-bit), ARM Cortex-M3 (STM32F103), National Instruments CompactRIO etc.
- Simulation software: Matlab, Simulink, Pspice
- PCB design with Altium Designer(Protel)
- Familiar with basic mechanical design and AutoCAD
- Good English skills: GRE: 570+800 TOEFL:102

RESEARCH EXPERIENCE

09/2017-06/2018: Multiple Reference Frame Based Torque Ripple Reduction of DFIG-DC System

- ✓ Analysis of the genesis of torque ripple in DFIG-DC system
- ✓ Design of a multiple reference frame (MRF) based torque ripple mitigation controller
- ✓ Simulation validation of the effectiveness of the proposed MRF based torque ripple reduction scheme
- ✓ Test rig design and build with a 7.5 KW doubly-fed induction generator and a 3 KW inverter
- ✓ Experimental results support that the proposed MRF based controller can greatly limit the torque ripple in the DFIG-DC system

09/2017-05/2018: Efficiency Optimization of DFIG-DC System via Extremum Seeking Control

- ✓ Analysis of the relationship between DFIG-DC system efficiency and stator frequency
- ✓ Design of an extremum seeking control (ESC) based DFIG-DC system efficiency optimizer
- ✓ Simulation validation of the effectiveness of the proposed framework
- ✓ Test rig design and build with a 7.5 KW doubly-fed induction generator and a 3 KW inverter
- ✓ Experiment validation demonstrate that the proposed controller can successfully track the optimum stator frequency that results in the highest efficiency of the DFIG-DC system

04/2016-08/2016: Model Wind Turbine Control Using NI CompactRIO

- ✓ Control the yaw angle of the model wind turbine using stepper motor
- ✓ Control the servo motor linked to each blade to change the blade pitch angle
- ✓ A DC motor powered linear actuator is used to control the tilt angle of the model wind turbine

06/2014-04/2016: Extremum Seeking Control (ESC) for Region-2 Operation of Wind Turbine

- ✓ Simulation study: implement single input ESC on a WindPACT 1.5 MW wind turbine model to search the optimal generator torque gain, pitch angle, yaw angle respectively
- ✓ Simulation study: implement multi-input ESC on a WindPACT 1.5 MW wind turbine model to search for the optimal operation point for generator torque gain, pitch angle and yaw angle

- ✓ Simulation study: implement both single input and multi-input ESC on the CART3 600 KW model
- ✓ Experiment study: develop and implement the ESC based controller code on NREL's CART3 600 KW wind turbine for field test

05/2013-06/2014: Multi-variable Extremum Seeking Control for Mini-split AC System

- ✓ NI CompactRIO is used to directly control the evaporator fan motor (BLDC)
- ✓ Use a TI DSP based motor controller to control the condenser fan motor (BLDC) (sensor-less control, speed closed-loop control, with inner current-loop control)
- ✓ Experiment study: implement single-variable ESC on the testbed to search the optimal working speed for the evaporator fan
- ✓ Experiment study: implement two-variables ESC on the testbed to search the optimal working speeds for both the evaporator fan and condenser fan
- ✓ Simulation study: implement three-variable ESC on a Modelica based ASHP model to find the optimal working points for the evaporator fan speed, condenser fan speed and superheat
- ✓ Theoretical analysis: optimal frequency selection for Newton-based ESC

09/2012-09/2013: Multi-variable ESC Based MPPT Control for Multi-String PV System

- ✓ Simulation study: gradient-based multi-variable ESC
- ✓ Simulation study: Newton-based multi-variable ESC
- ✓ Experiment study: implement gradient-based four-variable ESC
- ✓ Experiment study: implement Newton-based four-variable ESC

09/2012-04/2013: SPSA Based MPPT Control for Multi-String PV System

- ✓ Simulation based on two-measurement standard SPSA
- ✓ Simulation based on one-measurement SPSA
- ✓ Simulation based on one-measurement adaptive SPSA
- ✓ Simulation based on modified one-measurement adaptive SPSA
- ✓ Hardware Development: Design and develop a multi-port power electronic interface for the experiment study (four boost converters coupled electrically)
- ✓ Experiment study: implement SPSA on multi-string PV system

07/2010-08/2011: Sensor-less Permanent Magnet Synchronous Motor (PMSM) Controller Design

- ✓ Built a Simulink model of the control system. Proposed to use a Luenberger observer to estimate the rotor position. Simulation results showed that the Luenberger observer can perfectly track the actual rotor position in real time
- ✓ Developed the hardware of the controller. The MCU used here is an ARM (STM32F103). Other main parts include bus voltage sampling circuit, phase current sampling circuit, over current protection circuit, over voltage protection circuit, drive circuit, communication circuit, etc.
- ✓ To ensure a unity power factor of the whole system, an active power factor correction circuit is designed
- ✓ Developed the controller code that implementing the proposed Sensor-less PMSM control algorithm. Experiments demonstrate that the controller system can drive a PMSM perfectly within the required speed range (600r/min-4500r/min)

01/2011-07/2011: High Speed Brushless DC Motor (BLDC) Controller Design

- ✓ Designed the electrical circuit of the controller board. The MCU used here is Infineon XC878. Other main parts include bus voltage sampling circuit, phase current sampling circuit, over current protection circuit, over voltage circuit, drive circuit, communication circuit, etc.
- ✓ Assisted in the program development of the controller software. My main contribution is to develop the communication system. CAN is used to communicate between different controller board. UART is used to communicate between BLDC controller board and a computer

01/2009-06/2009: Isolated PV Power System Design

- ✓ Built a mathematical model of the system. Then a simulation study is performed to verify the analysis results
- ✓ Designed a 3KW prototype. The electricity comes from the PV board, through Buck circuit to the battery and inverter circuit. Rear level uses single-phase full-bridge inverter circuit, after which is an isolation step-up transformer. The MCU of the controller used is TI TMS320F2812, using the corresponding control strategy and system protection strategy in order to achieve the design specifications

EDUCATION

09/2012-08/2018: Ph.D. Candidate in Electrical Engineering

Department of Electrical Engineering,
University of Texas at Dallas, TX, USA

GPA: 3.642/4.0

09/2009-03/2012: M.S.E.E (specialty: Power Electronics and Electrical Drives)

College of Electrical and Electronics Engineering,
Huazhong University of Science and Technology, Wuhan, China
GPA: 86.03/100

09/2005-06/2009: B.S.E.E (specialty: Electrical Engineering and Automation)

College of Electrical and Electronics Engineering,
Huazhong University of Science and Technology, Wuhan, China
GPA: 85.22/100

PUBLICATION

[1] Y. Xiao, M. A. Rotea, Y. Li and B. Fahimi, "ESC Based Optimal Stator Frequency Control of DFIG-DC System for Efficiency Enhancement", *2018 IEEE Energy Conversion Congress and Exposition*, September 23-27, 2018, Portland, OR, USA.

[2] Y. Xiao, Y. Li and M. A. Rotea, "CART3 Field Tests for Wind Turbine Region-2 Operation with Extremum Seeking Controllers", *IEEE Transactions on Control Systems Technology,* 2018

[3] Y. Xiao, Y. Li and M. A. Rotea, "Multi-objective Extremum Seeking Control for Enhancement of Wind Turbine Power Capture with Load Reduction", *Journal of Physics: Conference Series,* Volume 753

[4] Y. Xiao, Y. Li and M. A. Rotea, "Experimental Evaluation of Extremum Seeking Based Region-2 Controller for CART3 Wind Turbine", AIAA 34TH Wind Energy Symposium, 2016

[5] T. Ashuri, M. A. Rotea, C. V. Ponnurangam and Y. Xiao, "Impact of Airfoil Performance Degradation on Annual Energy Production and Its Mitigation via Extremum Seeking Controls", AIAA 34TH Wind Energy Symposium, 2016

[6] T. Ashuri, M. A. Rotea, Y. Xiao, Y. Li and C. V. Ponnurangam, "Wind Turbine Performance Decline and Its Mitigation via Extremum Seeking Controls", AIAA 34TH Wind Energy Symposium, 2016

[7] L. Dong, Y. Li, B. Mu and Y. Xiao, "Self-optimizing Control of Air-source Heat Pump with Multivariable Extremum Seeking", *Applied Thermal Engineering,* 2015

[8] Y. Xiao, Y. Li and J. E. Seem, "Multi-variable Extremum Seeking Control for Mini-split Air-conditioning System", Purdue Conference, 2014

[9] Y. Xiao, Y. Li, J. E. Seem and K. Rajashekara, "Maximum Power Point Tracking of Multi-string Photovoltaic Array via Simultaneous Perturbation Stochastic Approximation", ASME 2013 Dynamic Systems and Control Conference, 2013

[10] Y. Xiao and Q. Xu, "Sensor-less PMSM Control System Research and Design", Master Thesis (in Chinese), 2012